Université Fédérale
Toulouse Midi-Pyrénées

THÈSE

En vue de l'obtention du

DOCTORAT DE L'UNIVERSITÉ DE TOULOUSE

Délivré par :

Institut Supérieur de l'Aéronautique et de l'Espace

Présentée et soutenue par :
Fábio MANZONI VIEIRA

le jeudi 30 novembre 2017

Titre :

Fusion de données AIS et radar pour la surveillance maritime

Fusion of AIS and radar data for maritime surveillance

École doctorale et discipline ou spécialité :
ED MITT : Signal, image, acoustique et optimisation

Unité de recherche :
Équipe d'accueil ISAE-ONERA SCANR

Directeur(s) de Thèse :

M. Jean-Yves TOURNERET (directeur de thèse)
M. François VINCENT (co-directeur de thèse)

Jury :

M. Frédéric PASCAL Professeur Centrale Supélec - Président
Mme Marie ANSART Ingénieure Thalès Alenia Space
M. Guillaume GINOLHAC Professeur Université Savoie Mont-Blanc - Rapporteur
M. Jean-Philippe OVARLEZ Maître de Recherche ONERA - Rapporteur
M. Jean-Yves TOURNERET Professeur INP Toulouse - Directeur de thèse
M. François VINCENT Professeur ISAE-SUPAERO - Co-directeur de thèse

Acknowledgments

I would like to thank first the one that gave me the opportunity to my long-desired dream of resuming my studies: My thesis director Jean-Yves Tourneret. An incredible person in all aspects. Sometimes I think he managed to clone himself in secret to be able to do so many things at the same time and still be there anytime. I am glad to have this opportunity to thank you for everything you did, teaching, supporting, pushing, criticizing, sharing and helping. I own you a lot.

Secondly, but not less important, I would like to thank my thesis co-direction François Vincent. Thank you for the opportunity to step in your scientific domain. It was really an honor to learn from you. I am still amazed for your energy in every solution proposed. Thank you for being available and for the patience with all my questions.

Next, I would like to thank my tutor at TéSA David Bonacci. You helped me not only with the technical subjects, but also sharing the good times at the laboratory and being open to discuss about everything.

From the industry support I would like to thank those that shared their time, experience, knowledge during the thesis journey: Marc Spigai, a great thanks for your contribution, for your patience and for being so kind giving ears helping me endure the difficult subjects and the hard times. Marie Ansart, for all colaboration during those three years. Jacques Richard, not only for providing his experience and knowledge for this research but for being so kind and supporting me in France, not forgetting to mention Bertille, a wonderful person in whom I lack adjectives to describe, thank you for the great time.

I would like to thank all those who I shared great experiences and which whom I had a lot of fun

during coffee breaks: Phillipe, David, Romain, Tarik, Charles-Ugo, Adrien, Selma, Karine, Maha, Jorge, Jean-Adrien, Raoul, Lorenzo, Simone, Silvain, Julien, Patrice, Bernard, Jacques, Corinne, Isabelle, Marie-José.

Also I would like to thank my friends at ISAE, the Brazilians in Toulouse and to all new friends I made during my stay in France.

I would like to dedicate this thesis also to my family and friends that are very far away and who I miss a lot. Also to my wife Helena, which survived the stress, headaches, my long studying days, the fright of my crazy bike stunts, for all your patience and helping me to pursuit my dream. Finally, I dedicate this to a little someone who I am anxious to meet!

Thank you all,

" *Do. Or do not. There is no try.* " - Yoda

Fábio

Résumé

Dans le domaine de la surveillance maritime, les systèmes d'identification et de positionnement coopératifs tels que le système AIS (Automatic Identification System) sont souvent couplés à des systèmes permettant l'observation de navires non coopératifs comme les Radars à Synthèse d'Ouverture (RSO). L'utilisation conjointe des images RSO et des signaux AIS peut permettre d'améliorer la détection de certains navires dans des environnements denses et d'identifier d'éventuels scénarii de piraterie. L'approche la plus répandue pour la fusion de données est la « fusion après détection » où chacun des systèmes traite les données brutes de manière indépendante. Dans le contexte AIS et Radar, trois niveaux de fusion peuvent être identifiés : 1) la fusion des données brutes, 2) la fusion des données brutes d'un système avec une carte de détection issue de l'autre système, 3) la fusion des cartes de détections issues des deux systèmes. Nous nous focaliserons sur les deux premiers contextes, le dernier étant plus largement traité dans la littérature. Après avoir introduit les systèmes AIS et Radar destinés à la surveillance maritime, nous détaillons la structure des données AIS et Radar, ainsi que le traitement du signal utilisé pour décoder les signaux AIS ou former une image radar. Le deuxième chapitre présente l'apport potentiel de l'utilisation conjointe des données brutes Radar et AIS pour la détection de navires. Après avoir décrit le modèle des signaux reçus en fonction de la position inconnue d'un bateau, nous étudions le problème de détection à l'aide d'un test basé sur le rapport des vraisemblances maximales (test GLRT). Les performances théoriques de ce test sont évaluées et permettent d'estimer le gain en performance par rapport à un traitement RSO seul. Ces performances théoriques sont validées par simulations de Monte Carlo via le tracé de Caractéristiques Opérationnelles du Récepteur (Courbes COR). Bien que les résultats soient encourageants,

la mise en pratique en temps-réel de telles méthodes semble compliquée. Nous nous tournons donc vers une solution sous-optimale mais réalisable, exploitant les données brutes Radar et une carte de détections provenant du système AIS. Le troisième chapitre étudie la fusion des données brutes Radar avec une liste de positions de navires, a priori fournie par le système AIS. Les navires étant mobiles et les instants de mesures AIS et Radar n'étant pas les mêmes, les positions des bateaux doivent être extrapolées. Deux cas sont alors traités successivement. Soit les erreurs d'extrapolations sont inférieures à la résolution du radar et n'ont pas à être intégrées dans le modèle, soit ces erreurs ne peuvent pas être négligées et doivent être prises en compte dans le modèle. Contrairement au deuxième chapitre, quatre hypothèses d'intérêt peuvent maintenant être distinguées. En effet, en plus des cas classiques de détection par les deux systèmes, on peut identifier les cas où seul l'un des systèmes détecte un objet correspondent aux situations où un navire n'émet pas d'AIS ou un navire qui biaise volontairement son AIS. Le problème peut se formaliser par deux tests d'hypothèses binaires successifs. Ce processus permet d'une part de fusionner de manière naturelle les informations AIS et radar, mais permet également d'améliorer la performance en détection du radar. La comparaison des performances de ce détecteur disposant de l'information a priori à celle d'une détection radar classique montre qu'elle est moins sensible à la proximité et à la densité des autres navires. Le quatrième chapitre présente le fonctionnement du simulateur que nous avons développé dans le cadre de cette thèse pour tester les algorithmes sur différents scénarii de surveillance, à savoir un scénario de piraterie sur un navire civil, un transbordement illégal et une navigation dans un environnement dense.

Abstract

Cooperative systems used for vessel identification and localization in the context of maritime surveillance, such as the Automatic Identification System (AIS), are often coupled to systems that allow the observation of uncooperative ships such as the Synthetic Aperture Radar (SAR). The combination of information coming from the SAR image and AIS signals can improve the detection of some ships in dense environments, but also allows possible piracy scenarios to be identified. The most common approach for data fusion is the "fusion after detection", where each system processes the raw data independently. In the context of AIS and Radar, three levels of fusion can be identified: 1) fusion of the raw data, 2) fusion of raw data from a system with the processed data (list of detection) from the other system, 3) fusion of the detection lists formed by the two systems. We will focus on the first two cases, since the last case has been more widely covered in the literature. After introducing the AIS and Radar systems for maritime surveillance, we present structure of AIS data and radar signals, as well as the signal processing used to decode these AIS signals or to produce a radar image. The second chapter presents the potential benefits of the joint use of raw data from both radar and AIS for ship detection. After having described the signal models associated with the unknown ship position, we investigate the detection problem using a Generalized Likelihood Ratio Test (GLRT). The theoretical performances of this test are evaluated and allow us to estimate the performance gain in comparison to a single RSO processing. These theoretical results are validated by Monte Carlo simulations using Receiver Operational Characteristics (ROC). The detection results obtained using the GLRT are encouraging. However, the time implementation of these methods for practical applications is complicated. We therefore proceed to a sub-optimal detector using raw data from the

radar and a list of detections from the AIS system, leading to a more simple detection strategy. The third chapter studies the fusion of raw radar data with a list of ship positions, formerly provided by the AIS system. Since the ships are moving and the AIS and Radar measurements are not are not acquired at the same time instants, the ship positions have to be extrapolated. Two extrapolation cases are considered in this work: 1) extrapolation errors are lower than the radar resolution and do not have to be integrated in the model, 2) extrapolation errors are not negligible and have to be taken into account in the model. Contrary to the second chapter, four hypotheses can now be considered. Indeed, in addition to the classical detection scenarios by both systems, we can identify the cases where only one of the systems detects a ship, which corresponds to the situations where a ship does not transmit its AIS position or where a ship intentionally false its AIS position. The problem can then be formalized with two successive binary hypothesis tests. This process allows the information coming from AIS and radar data to be fused naturally, aleading to improved radar detection performance. A performance comparison of this detector that uses a priori information with conventional radar detection shows that it is less sensitive to the proximity to other ships and to the ship density of the considered scenario. The fourth chapter presents the signal simulator considered in this thesis to test the detection algorithms in different surveillance scenarios, i.e., a piracy ship hijacking scenario, an illegal cargo transshipment and a navigation in a dense environment.

Contents

List of Figures

List of Tables

Introduction

Context and thesis challenges

Maritime surveillance can rely on cooperative transmitting technologies used for vessel identification and localization, such as the Automatic Identification System (AIS). The AIS is a shipborne VHF radio system that is used for maritime communication worldwide, designed to cooperatively broadcast AIS messages containing positioning and voyage information such as ship identification, size, position, heading, speed and others. However, cooperative systems alone are not fully appropriate because of the diversity of surveillance scenarios and the presence of uncooperative ships. In those cases, data can be counterfeit, masked or even not transmitted at all. Also, some ships are not enforced by maritime regulations (small boats for example) and the carriage of AIS equipment is optional. On the other hand, there are other systems that allow the observation of uncooperative ships, such as the Synthetic Aperture Radar (SAR). The use of different information sources is a natural choice to overcome the individual sensor limitations and manage both cooperative and non-cooperative systems such as the AIS and radar systems.

The objective of this thesis is to study and evaluate a dedicated data fusion scheme for AIS and radar data in order to improve maritime surveillance performance. Concerning this study, the combination of information coming from the SAR image and AIS signals can improve ship detection in dense environments with cooperative ships, but also allows some surveillance scenarios to be identified.

This thesis has as been conducted at the TéSA laboratory in Toulouse and in collaboration with

Signal, Communication, Antennes, Navigation (SCAN) research unit from the Institut supérieur de l'aéronautique et de l'espace (ISAE) and the institute of research in computer science (IRIT laboratory) of Toulouse. This research was funded by Thales Alenia Space - Toulouse and by Thales International Brazil.

Manuscript organization

The first chapter introduces the general operation of the AIS system followed by the radar system. It describes the AIS signal structure as well as the binary representation of the AIS message and the signal processing used to reproduce and decode those signals. Similarly, we present the structure of spatial Synthetic Aperture Radar, defining the models necessary to simulate the SAR signals that will be used to provide representative data for the simulations in the next chapters.

The second chapter presents the potential benefits of the joint use of raw data from both radar and AIS for ship detection. After having described the signal models associated with the unknown ship position, we investigate the detection problem using a Generalized Likelihood Ratio Test (GLRT). The theoretical performances of this test are evaluated and allow us to estimate the performance gain in comparison with a single SAR processing. These theoretical results are validated by Monte Carlo simulations using Receiver Operational Characteristics (ROC). The detection results obtained using the GLRT are encouraging. However, the time implementation of these methods for practical applications is complicated. We therefore proceed to a sub-optimal detector using raw data from the radar and a list of detections from the AIS system, leading to a more simple detection strategy.

The third chapter studies the fusion of raw radar data with a list of ship positions, formerly provided by the AIS system. Since the ships are moving and the AIS and Radar measurements are not acquired at the same time instants, the ship positions have to be extrapolated. Two extrapolation cases are considered in this work: 1) extrapolation errors are lower than the radar resolution and do not have to be integrated in the model, 2) extrapolation errors are not negligible and have to be taken into account in the model. Contrary to the second chapter, four hypotheses can now be considered. Indeed, in addition to the classical detection scenarios by both systems, we can identify

the cases where only one of the systems detects a ship, which corresponds to the situations where a ship does not transmit its AIS position or where a ship intentionally false its AIS position. The problem can then be formalized with two successive binary hypothesis tests. This process allows the information coming from AIS and radar data to be fused naturally, leading to improved radar detection performance. A performance comparison of this detector that uses a priori information with conventional radar detection shows that it is less sensitive to the proximity to other ships and to the ship density of the considered scenario.

The fourth chapter presents the signal simulator considered in this thesis to test the detection algorithms in different surveillance scenarios, i.e., a piracy ship hijacking scenario, an illegal cargo transshipment and a navigation in a dense environment.

Main contributions

The main contributions of this thesis are presented below.

Chapter 1. This chapter details the AIS and SAR systems considered in this thesis. These systems are well known and thus there is no new contribution in this chapter.

Chapter 2. We present a ship detection method based on Generalized Likelihood Ratio Test (GLRT) that integrates both AIS and radar raw data. The detector performance is evaluated and shows an important gain when compared to a single SAR processing. This new detector was published in the conference paper [VVT+16].

Chapter 3. We propose to use the knowledge of cooperative ship positions obtained from the AIS system with raw radar data to detect ships. We formalize the GLRT detection problem with two successive binary hypothesis tests that can identify the cases where a ship does not transmit its AIS position or where a ship intentionally false its AIS position. Besides, it can lead to improved radar detection performance in some scenarios with cooperative ships. This new fusion rule was published in the conference paper [VVT+17].

Chapter 4. We present the signal simulator considered in this thesis and use it to test the detection algorithms in different surveillance scenarios, i.e., a piracy ship hijacking scenario, an illegal cargo transshipment and a navigation in a dense environment. We demonstrate the advantage of using the proposed detector to identify some surveillance scenarios and also to improve ship detection in some specific situations in the presence of cooperative ships.

Chapter 1

Radar and AIS over satellite

1.1 Introduction (in French)

Représentant 3/4 de la surface de la terre, les océans et mers jouent en rôle prépondérant entre autres pour le transport, la pêche, les loisirs, les aspects militaires et stratégiques. Ils représentent aussi une zone de danger sur notre planète. L'*International Maritime Organization* (IMO) a requis l'utilisation de moyens de sécurité en mer comme l'*Automatic Identification System* (**AIS**), qui est un système radio VHF diffusant la position, vitesse, identité et statut des navires dont la jauge dépasse une valeur minimale. On qualifie l'AIS de **système coopératif**.

Dans le domaine de la surveillance maritime, de par l'existence de bateaux non coopératifs (dysfonctionnement, extinction intentionnelle de l'AIS, bateaux de petite taille, etc.), les systèmes coopératifs sont souvent couplés à des systèmes externes, **non coopératifs**, comme par exemple

le **Radar** qui permet, au moyen d'ondes électromagnétiques, de localiser voire suivre des objets en mouvement ou non, de jour comme de nuit. On peut distinguer notamment les Radars qui ont pour objectif une localisation de points « cibles » dans un espace en 2 ou 3 dimensions, c'est le cas par exemple des Radars côtiers, des Radars qui ont pour objectif de créer une image en deux dimensions dans lesquelles se trouve la réponse, en terme de rétrodiffusion, des cibles se trouvant sur la zone géographique délimitée par l'image : c'est le cas des Radars à Ouverture Synthétique (ROS, ou **SAR** *Synthetic Aperture Radar*) que l'on trouve à bord de satellites en orbite défilante.

L'utilisation conjointe fusionnant Radars SAR (non coopératifs) et AIS (coopératifs) fournit de l'information de première importance pour la surveillance maritime: détection, localisation, voire reconnaissance et identification de bateaux.

L'approche la plus répandue pour la fusion est la « *fusion after detection* » où chaque système calcule une détection de cibles indépendamment des autres et la fusion consiste alors à combiner les détections des différents systèmes. D'autres approches sont possibles comme la « *fusion before detection* » où l'on cherche à combiner les données « signal » de chaque système au plus tôt (on parle alors généralement de « données brutes », *raw data*) c'est-à-dire avant même de chercher à détecter des cibles pour chaque système. Il existe aussi des compromis où l'on va utiliser les données brutes d'un système, le SAR par exemple, avec les données de détection d'un autre système, l'AIS dans l'exemple. Pour terminer, l'aspect intégration temporelle peut aussi être pris en compte dans la fusion, où l'on cherche à utiliser la cohérence du mouvement des cibles dans le temps.

Dans la thèse on a résumé les différentes fusions AIS-SAR en 4 niveaux :

- Fusion de niveau 1: Données brutes AIS et Radar.
- Fusion de niveau 2: Données brutes Radar et données traitées AIS (traitées = détection AIS), ou données traitées Radar (traitées = détection radar) et données brutes AIS.
- Fusion de niveau 3: Données traitées AIS et Radar. Il s'agit de la fusion la plus répandue sur le sujet à l'heure actuelle.
- Fusion de niveau 4: Données temporelles traitées AIS et Radar, exploitant notamment la revisite des satellites en orbite défilante.

On va présenter dans la suite de ce résumé les signaux AIS et Radar SAR imageur par satellite.

AIS

Concernant les systèmes AIS1 et AIS2 dont les spécifications sont données dans la recommandation UIT-R M.1371-2, édition 2006, les caractéristiques principales des signaux émis sont les suivantes :

- Organisation fréquentielle :
  - Transmissions alternatives sur deux canaux: à 161.975 MHz (canal 87) et à 162.025 MHz (canal 88)
  - Bande de 25 kHz (bande large) ou de 12,5 kHz (bande étroite)
- Modulation et codage :
  - Codage NRZI avec un changement de niveau sur l'élément zéro et le bit stuffing
  - Modulation GMSK adaptée en bande de fréquences (GMSK/FM) de produit BT = 0,3 (bande étroite) ou 0,4 (bande large) et indice de modulation de 0,25 (bande étroite) ou 0,5 (bande large)
  - Débit de transmission : 9600 bits/s
- Puissance : 12.5 Watts (classe A) et 2 Watts (classe B).

Au niveau de l'organisation temporelle, le système AIS est auto-organisé (selon le protocole SO-TDMA : Self-Organized Time Division Multiple Access) sur de petites cellules d'un diamètre de 50 milles nautiques environ. Les trames d'une minute, sont divisées en 2250 intervalles de temps : 1 slot dure 26.67 ms. Le début et la fin de la trame coïncident avec la minute UTC.

Au démarrage du système, les bateaux « écoutent » pendant une minute les messages émis par les bateaux du voisinage pour choisir un time slot libre et s'insérer dans celui-ci. Ainsi, 2 bateaux qui ne sont pas à portée directe l'un de l'autre peuvent choisir le même time slot.

Pour cette raison, à plus grande échelle, il n'y a plus d'organisation et le champ de vue depuis un satellite (même en orbite basse à une altitude de l'ordre de quelques centaines de kilomètres) étant beaucoup plus large que celui d'un bateau, des collisions de signaux vont donc se produire.

Il existe plusieurs types de messages. Les messages de type 1, 2 et 3 contiennent des informations « dynamiques » (position, cap, ...) et sont émis fréquemment. C'est à ces derniers que l'on s'intéressera dans cette thèse. La période de répétition de ces messages dépend de la classe du navire, du type d'information, de la vitesse du navire et des changements de route. Par exemple un navire de classe A à 20 noeuds transmettra les messages de type 1 toutes les 6 secondes.

Les problèmes essentiels de la capture des signaux AIS depuis l'espace sont :

- Un faible rapport signal à bruit à cause de la distance séparant le bateau du satellite
- La faisabilité de séparation des messages lorsqu'ils entrent en collision, en vue du décodage.
- La faible fréquence de répétition des messages qui fait qu'il est difficile d'utiliser ces répétitions pour améliorer le taux de décodage des messages.

Radar à Synthèse d'Ouverture

Comme déjà indiqué dans le début de ce résumé, on peut distinguer différents types de Radars. On présente ici les principes généraux du Radar à Synthèse d'Ouverture (RSO, ou SAR Synthetic Aperture Radar) que l'on trouve à bord de satellites en orbite défilante ou d'avions qui ont pour objectif de créer une image en deux dimensions dans laquelle se trouve la réponse, en terme de rétrodiffusion, des cibles se trouvant sur la zone géographique délimitée par l'image.

L'objectif d'un SAR est donc de fournir une image où chaque pixel représente l'amplitude et la phase du signal rétrodiffusé par la cible se trouvant dans le pixel vers le satellite en réponse à une émission électromagnétique effectuée par celui-ci.

Chaque cellule de résolution est caractérisée par une résolution distance (axe perpendiculaire au mouvement du satellite) et une résolution azimut (axe parallèle au mouvement du satellite). La résolution distance est obtenue « électroniquement » par émission de chirps suivant l'axe distance, tandis que la résolution azimut est obtenue par l'utilisation de l'effet Doppler crée par le mouvement du satellite au-dessus de la cible pendant un certain temps d'observation. On parle d'antenne synthétique car le mouvement du satellite peut être vu comme une antenne virtuelle très longue, de l'ordre de plusieurs kilomètres.

Dans le cadre de la thèse il est important de comprendre la notion de données brutes (raw data): les SAR émettent des impulsions tout au long du temps d'observation de la cible, les impulsions sont synchronisées et ont une phase connue, on parle de système cohérent. Le signal reçu au cours du temps est une suite de signaux temporels relatifs au passage du lobe d'antenne Radar sur la scène observée. A ce stade on a des signaux « bruts » représentant des mélanges de réponses de cibles à divers endroits de la scène éclairée par le lobe d'antenne. Pour ramener l'énergie et la phase spécifiques à chaque cellule de résolution au sol on réalise en azimut une synthèse d'ouverture et une compression distance sur l'autre axe. On montre qu'il s'agit, projeté sur la surface de la Terre, de l'intersection de courbes iso-distances (des cercles) et de courbes iso-doppler (des hyperboles) et que pour lever des ambigüités (plusieurs solutions possibles après intersection) on décale le lobe d'antenne par rapport à la verticale d'un angle d'incidence non nul afin de pointer à un endroit où les ambiguïtés sont levées dans une certaine mesure. En résumé on sépare donc les données brutes (signal brut reçu par le passage du lobe d'antenne) de l'image amplitude/phase pour chaque cellule de résolution obtenue après synthèse d'ouverture et compression d'impulsions.

Une fois l'opération de synthèse réalisée, on dispose au sol de l'énergie et phase spécifique à chaque cellule de résolution. Il y a en général des opérations qui suivent (interpolation, etc.) pour ramener l'énergie sur des pixels sur une grille qui est souvent régulière, par exemple 5 mètres $\times$ 5 mètres. Il ne faut pas confondre la notion de résolution physique du capteur, qui est la capacité physique du capteur à séparer deux cibles écartées d'une valeur égale à cette résolution, de la notion de taille de pixels qui peut-être virtuellement plus grande ou plus petite. Une fois l'image disponible on peut effectuer par exemple une détection de cibles souvent basée sur l'amplitude (énergie) contenue dans chaque pixel. Dans la thèse cette opération est souvent résumée par le terme « données traitées ».

Pour terminer, un SAR a plusieurs modes de mesures. Ainsi la résolution azimut d'une cellule de résolution dépend du temps d'observation de celle-ci par le lobe d'antenne. On a alors un compromis entre la taille de la zone observée et la résolution. On distingue classiquement les modes ScanSAR (grande zone, faible résolution), Spotlight (petite zone, très bonne résolution) et Stripmap (zone moyenne, moyenne résolution). Les hypothèses de travail sous-jacentes à la thèse sont basées sur le mode Stripmap.

1.2 Introduction

The sea covers 3/4 of the Earth's surface, with the oceans representing an area of 361 million square kilometers. About 80% of world transportation is done using maritime routes [Fou12] with more than 90% of the world's trade being transported in containerized cargo over the seas [UNC08]. On top of that, the number of ships is continuously increasing. In 2016, the global merchant fleet was around 92 thousands vessels, representing an increase of 10% in a period of five years [Uni17], not including other type of sea activities, for example people transporting, fishing, military, recreational applications, among others.

The continuous growth of maritime transport raises some challenges. Indeed, oceans remain the most dangerous places in the planet. For reference, commercial seafaring is considered the second-most dangerous occupation just after deep-sea fishing [All15]. Particularly, the navigation in crowded ocean areas near ports and sea channels, the occurrence of illicit activities like cargo transshipment, smuggling, illegal fishing, and even the emergence of sea piracy in the modern days are examples of important scenarios that impacts sea safety and security.

A transshipment refers to the action of moving a cargo load from one vessel to another. Sea transshipment is not fundamentally an illegal operation and many carriers use this mode of cargo loading and unloading for his greater logistical flexibility. On the one hand, it also difficult the control and tracking of illegal cargo loading operations by the maritime authorities. Some examples of illicit transshipment includes the shipment of drugs, illegal goods and weapons between smugglers from organized crime networks. In fishing, illegal transshipment is a far widespread operation. It is frequently used to import and export stocks of fish from illegal fisheries. A common procedure includes a fishing vessel sending its stock on a cargo ship, which exports the cargo directly without returning to its home port. Thus, no control can be carried out neither tax are paid. To understand the significance of the phenomenon, here are some numbers : the global income losses of states in the world due to illegal unreported and unregulated fishing are estimated to be between 10 and 23.5 billion dollars per year, i.e., at least 6.5 times the total GDP of the African continent produced in 2008. Fisheries can sometimes reach 37% of the total fish catch in the region at East Africa [APP+09].

The economic stakes are therefore considerable, since these fisheries do not generate benefits for the local inhabitants and threaten food security and marine biodiversity.

About piracy, pirates may be defined as those who resort to unauthorized violence against a ship outside the jurisdiction of a state, on the high seas [Det13]. Due to economizing strategies, there are more merchant vessels transporting valuable cargo manned by reduced crews. Those became easy targets for the gangs of armed criminals, named pirates [Mar11]. One typical piracy approach is to board a victim ship with a small boat with heavy armed pirates, take control of the ship, then steal its cargo or kidnap the crew for a ransom. Under few exceptions, piracy was nearly extinct until 1992 when the Nagasaki Spirit tanker collided with the Ocean Blessing container in the Malacca Straits after being seized by pirates and left unmanned. The resulting collision caused the spilling of $12,000$ tonnes of crude oil into the sea that caused fire, destroying both ships and killing all but two crew members [Bur03; Ong06]. This incident marked the beginning of modern piracy era. It represents the most challenging threat to international maritime security [Gov11] and is considered a worldwide problem, despite being more concentrated in the East Africa near Somalia and Yemen, in the West Africa near Nigeria, and the South East Asia. According to reports from Oceans Beyond Piracy (OBP), the economic cost of Somalia piracy was estimated to be near 6.6 billion dollars in 2011, declining to 1.7 billion dollars in 2016 mainly due to counter-piracy efforts in the recent years. Globally, the economic cost of piracy in 2016 was estimated in 2.5 billion dollars [Oce17]. Despite the lower numbers over the last years, pirates have continued their involvement in other illicit maritime activities, such as arm smuggling and human trafficking. The number of registered incidents in 2016 was 278 cases of piracy and armed robbery in sea.

The piracy, sea transshipment and navigation in areas of dense ship traffic represents examples of maritime scenarios that represent important challenges in maritime surveillance applications to properly ensure the safety, security and to monitor ship traffic.

1.2.1 Maritime surveillance

Maritime surveillance has been a subject of growing interest during the recent years [HLP15; MVS15]. It can be performed with information from vessel monitoring systems based on cooperative transmitting technologies or from detection sensors.

Cooperative sources are equipped with electronic navigation sensors in order to estimate the position of a ship, usually a global navigation satellite system (GNSS) or an inertial sensor, and with radio equipment for communication purposes. One example of cooperative system is the automatic identification system (AIS), a shipborne VHF radio system that is used for maritime communication worldwide. It was conceived to enhance safety of life in the sea, to protect the maritime environment and to improve security and navigation efficiency.

Despite providing useful information, cooperative systems alone are not fully appropriate for maritime surveillance because of the diversity of surveillance scenarios and the presence of non-cooperative targets. Just as an example, in scenarios considering illicit activities, cooperative data can be counterfeit, masked or even not transmitted at all. It can also be mentioned that some ships are not enforced by maritime regulations (small boats for example) and the carriage of AIS equipment is optional. For those reasons, maritime surveillance using only cooperative information is a real challenge. For this reason, to resolve the non-cooperative scenarios one usually relies on remote sensing equipment such as radars or image sensors. These can be deployed in coastal stations, ships, aircrafts and satellites.

As a matter of comparison, non-cooperative systems are less sensitive to deception when considering non-military situations (targets without furtiveness or radar countermeasures). Radar sensors have proved useful when dealing with specific maritime surveillance scenarios [BLF+11]. Still, there are lots of remaining challenges related to maritime surveillance using only non-cooperative system since information recovery is limited and the detections need to be interpreted somehow. These challenges include ship detection, identification and tracking, or speed and heading estimation. Furthermore, some non-cooperative systems have limited coverage and their reliability can vary with environmental conditions, e.g., related to sea clutter.

For all reasons mentioned above, the use of different sources of information is a natural choice

to overcome the individual sensor limitations and manage both cooperative and non-cooperative targets. Radars associated with cooperative systems provided important information for maritime surveillance applications [MKS16; ZJX+14; GMB+09; CYS+11]. Jointly, AIS data with radar embedded satellites is an interesting solution for ship detection, identification and tracking. Satellites may overcome some difficulties of performing maritime surveillance within very large oceanic areas, where no ground infrastructure is available. They enable the surveillance and control of areas beyond country borders while avoiding legal constraints and disputes involving the sovereignty of third countries.

Data fusion systems can exploit the complementary information associated with dissimilar sensors for high performance maritime surveillance. However, processing the data requires an appropriate data fusion strategy. There are different ways to integrate AIS with radar data :

- Fusion Level 1: AIS and SAR raw data.
- Fusion Level 2: AIS processed data and SAR raw data (or AIS raw and radar processed data).
- Fusion Level 3: AIS and SAR processed data (most common fusion strategy).
- Fusion Level 4: Tracking of AIS and SAR data (exploring satellite revisit).

The first fusion level is the integration of AIS with radar raw data. In this method, sensor raw data is explored in a data fusion scheme before performing detection. With detection, when data exceeds a given threshold, a detection is made and the raw data is discarded. By using a "fusion-before-detect" scheme, that is, using the raw sensor data fusion before detecting, more data would be available and possibly a better performance could be attained.

The second approach is to still use fusion with raw sensor data, but this time, only one sensor raw data is used while exploring processed data from the other sensor (as a secondary source of information). This approach may allow segregation of different types of ship targets, according to the types of detection errors and also to improve detection as shown in Chapter 3.

The most conventional approach considers data fusion after detection, where the detectors provide lists of detections that need to be merged together. Some features that can be used for data fusion

include ship position, heading and speed among others (see [MVS15; GMB+09; CYS+11; MT11] for more details). Here this approach corresponds to the fusion level 3.

The fourth level of fusion considers the exploration of satellite revisit time in order to improve tracking or detection of ships by long term integration of data.

In this thesis the first and second data fusion levels are investigated considering the AIS and radar systems, being the others levels extensively explored in the literature. The rest of this chapter presents both AIS and radar systems used for maritime surveillance applications. The AIS system and the radar are detailed and a signal model is presented for both systems. The radar and AIS signal models will be used in the following chapters in order to generate the synthetic data to test the proposed data fusion methods.

1.3 Automatic Identification System

The AIS is an important asset originally designed as an anti-collision communication system for large vessels, operating locally in a semi-cell organization with the nearby vessels at range. It performs autonomously ship-to-ship and ship-to-shore communications, automatically exchanging information with the nearby vessels, navigational aids and shore stations. The AIS equipment is designed to cooperatively broadcast its own situation while gathering information from others in the vicinity area simultaneously, providing a picture of the environment and local ship traffic. AIS messages include positioning and voyage information such as ship identification, size, position, heading, speed and others.

With sea safety as subject of interest, the *International Maritime Organization* (IMO) requires flag states to ensure that their ships comply with minimum safety standards, from which one of those states the provision of traffic awareness to ship vessels with the compulsory use of the AIS system. Consequently, with the majority of ships carrying an AIS transmitter the AIS became an important source of information for ship traffic data.

The AIS was proposed as an anti-collision measure to preserve ship safety and originally designed for local communications. Despite of that, many [RTC+10; ZJX+14; PPHD15] consider the harvest

AIS broadcasts in different ways like in sea ports, surveillance ships, aircrafts [PPHD15] and even satellites [Pré12; ESN+10]. Yet, the AIS system has been proved an important cooperative source of information for different applications, e.g., ship registration, maritime situation awareness, ship traffic control and monitoring, safety and security [ESN+10], maritime surveillance [RTC+10; PPHD15], among others.

The International Telecommunications Union (ITU) and the *International Electrotechnical Commission* (IEC) define the standards for the different classes of AIS systems from which there are two types of shipborne AIS: Class A and Class B AIS devices. The IMO adopted the AIS Class A shipborne equipment through the carriage requirements in the Safety of Life at Sea convention (SOLAS) which stipulate the size and type of vessels that have to carry AIS devices [ITU14]. SOLAS defines that the AIS is mandatory equipment for vessels of 300 gross tonnage and upwards engaged on international voyages, all vessels of 500 gross tonnage and upwards and passenger ships irrespective of size. AIS Class B are shipborne devices that operate with less functionality and lower transmitting power compared to Class A AIS and are intended for voluntary use by non-SOLAS regulated vessels.

There are four frequency channels reserved for AIS use worldwide (other frequencies may be designed for AIS on a regional basis). The first two channels are allocated for standard AIS operations and the last two channels are reserved for a special type of AIS vessels. They are designed long range AIS broadcast messages (see Table 1.1). The Class A AIS equipment has operational range within 20 to 30 nautical miles and the reporting interval depends on the speed and ship dynamics. The repetition time of AIS Class A goes from 2 to 10 seconds when moving to 3 minutes for an anchored or not moving ship. The operational characteristics define the physical limits of the AIS communications to a cell, which is a local geographic area where users shall be able to communicate.

The standard AIS communications are realized within AIS 1 and AIS 2 channels using a time division channel access method known as Self-Organizing Time Division Multiple Access (SOTDMA) in order to coordinate ship communications in a given geographic cell. The signal structure is composed of a frame divided into time-slots. SOTDMA operates without a central controller. Organization of the messaging structure is done by each user individually announcing their next intended transmission time-slot. This method lets the users to adapt themselves in allocating the available time-slots in

Table 1.1: AIS frequency channels

Channel	Frequency	Description
87B	161.975 MHz	AIS 1
88B	162.025 MHz	AIS 2
75	156.775 MHz	Long range AIS
76	156.825 MHz	Long range AIS

order to avoid message collisions (more than one message transmission occurring at a single time-slot).

The next section gives an insight about the AIS communications concerning the structure of AIS signal and the modeling used.

1.3.1 AIS signal structure

The AIS system broadcast information about ships dynamic and other data in a self-organized structure in a time division multiple access (TDMA) scheme. The AIS uses the concept of frames to divide the user transmissions. One frame is equal to the period of one minute and it is subdivided into 2250 slots that are used for AIS communications.

In this thesis, we are interested in Class A AIS communications because of the widespread usage and stronger signal power [Pré12]. The class A AIS equipment is conceived to be permanently active and to operate continuously in order to allow other ships to identify the nearby vessels whenever they are moving or anchored [ITU14]. The AIS equipment operates by default in the autonomous mode the majority of time. In this mode, the AIS equipment continuously tries to determine its own schedule for AIS communications and automatically resolves transmission scheduling conflicts with the others AIS users that operates in the vicinity (the AIS cell range). Also, the reporting interval depends on the ship's dynamic conditions. The report intervals presented in Table 1.2 were designed to minimize unnecessary loading of the radio channels and to preserve AIS performance standards defined by the IMO [IMO04; IMO98].

Beyond autonomous mode, the AIS may be set to operate in assigned mode or in polled mode. In the assigned mode, the current transmission schedule of the AIS equipment changes to take into

Table 1.2: Repetition times for class A AIS transmissions in autonomous mode

Ship dynamic conditions	**Reporting interval**
Anchored or moored with speed lower than 3 knots	3 minutes
Anchored or moored with speed faster than 3 knots	10 seconds
Moving from 0 to 14 knots	10 seconds
Moving from 0 to 14 knots and changing course	3 1/3 seconds
Moving from 14 to 23 knots	6 seconds
Moving from 14 to 23 knots and changing course	2 seconds
Moving from 23 knots	2 seconds
Moving from 23 knots and changing course	2 seconds

account a command message received beforehand from an AIS base station. In the polled mode, the AIS equipment automatically reschedules itself to respond the interrogation message received from other AIS user.

1.3.2 The AIS packet

Data communications with AIS adopt a bit-oriented format which is almost identical to the general High Level Data Link Control (HDLC) structure specified by ISO/IEC 13239:2002 [ITU14]. The AIS equipment synchronizes the AIS frames using coordinated universal time (UTC) or, in absence of an UTC source, it uses packets received from other AIS stations. The AIS packet contains signaling and message bits that are divided into seven blocks as represented in Figure 1.1. The ramp up and buffer blocks are used for timing. The training sequence, start flag and ending flag are used for AIS communication signaling. Together, both data and the cyclic redundancy check (CRC) blocks form the AIS message part of the packet.

The size of AIS packet may vary according to the quantity of data to be sent. In the standard form, the AIS packet is a sequence of 256 bits which may hold 168 bits of data. Longer transmission packets may store more data occupying two or more AIS frame slots. The majority of messages including the ones that we are interested have the standard size. The AIS message is organized as follows

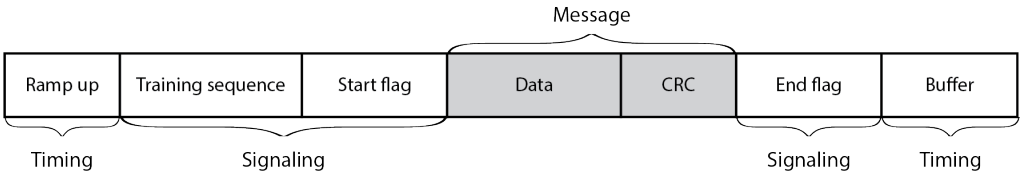

Figure 1.1: The AIS packet format

- The ramp up block represents a guard time of 8 bits to allow the transmitter to reach 80% of its nominal operation power.
- The training sequence is part of the signaling. It corresponds to a bit pattern of alternating zeros and ones (0101 . . . 01) containing 24 bits that serves for AIS receiver synchronization. The sequence always starts with a "zero".
- The start and end flag patterns are also used for signaling. They are important to indicate the message boundaries within the AIS packet. They both are represented by the same 8 bits pattern "01111110". Detection of AIS signal is usually performed using the known header in the AIS packet (24 bits of the training sequence and 8 bits of the start flag) [PCB+13].
- The message starts with the data block, which in the standard format may hold 168 bits of information. Right after data bits there is a block of 16 bits used to store cyclic redundancy check (CRC) data. The CRC is calculated over the data bits and used to provide error detection functionality at the reception of AIS packets. The CRC can be also used for error correction [Pré12].
- Due to the nature of AIS communications it is necessary to add some time margin to avoid overlapping of AIS transmission slots. This is done by the addition of a block buffer in the AIS packets. This block reserves 24 bits in order to compensate for timing errors. The buffer guards for the synchronization jitters that may happen in the AIS transmitting equipment.
- There are also transmission delays due to the propagation time considering the distance between the receiver and ship transmitting the AIS packet. Buffer is also important to allow reception of AIS packets with different sizes which are result from the extra bits added by bit stuffing

process. The number of stuffed bits is unknown and depends on the content of the transmitted message.

1.3.3 Construction of the AIS packet

The AIS bit stream is represented in Figure 1.1. The construction of the AIS packet starts with the calculation of the CRC based on the data bits. Then the CRC block is appended to the end of the data, creating the message part of the AIS packet. Next after the addition of CRC the bit stream is transformed by a bit flipping process and immediately after it gets transformed by another bit coding process called bit stuffing. After the bit stuffing process, the transformed message bit stream is concatenated with the signaling parts of the AIS packet: The end flag is appended to the end and the training sequence with the starting flag are appended to the beginning of the message. At this point, the AIS packet entire bit stream is now encoded using the non-return to zero inverted (NRZI) code, then finally sent to the modulator using the Gaussian minimum filtered shift keying (GMSK/FM) modulation before the transmission. The AIS packet to be transmitted is sent from left to the right, starting with the training sequence, followed by the start flag, message part and finally the end flag). The entire process of AIS packet construction before transmission is represented in Figure 1.2.

Figure 1.2: Construction of the AIS packet for transmission

The physical parameters for AIS (such as, e.g., the modulation index, frequency bandwidth, bit rate,...) are defined in the AIS regulation standards [ITU14].

AIS message

There are 27 different types of AIS messages [ITU14]. This study will focus on the AIS position reports considering that those contain relevant information with respect to ship positioning and identification. AIS position reports are the AIS message numbers 1, 2 and 3 defined by the AIS

standard. Those are the more recurrent message types in AIS communications. Table 1.3 presents the bits reserved for the construction of the AIS message. Details about the bits in the message block can be found in [ITU14].

Cyclic redundancy check

The CRC is a cyclic code used to provide a check value to a bit sequence. It is designed to protect data against errors that are common in communication channels and to grant the integrity of data. CRC is defined as the remainder associated with a division of the data bits by a polynomial. AIS provides a way to identify if there are errors in the AIS transmitted data. The CRC is a 16-bit polynomial that is calculated over the AIS message part (see Figure 1.1). The CRC is computed from the 168 AIS information bits and then appended to the end of the bit stream, creating the AIS message block. The CRC calculation is defined in ISO/IEC 13239:2002. The AIS standard defines that CRC bits are pre-set to "one" at the beginning of calculation. More details of AIS calculation can be found in [Pré12].

Flip bits

The flip bits process is part of the AIS specifications. It transforms the message (the data and CRC blocks) by flipping the bit order inside each octet (see Figure 1.3). The order is reversed such as in a octet the 1^{st} bit becomes the 8^{th}, the 2^{nd} becomes the 7^{th} bit, and so on. This allows calculating the CRC continuously during the reception of each octet. Bit flipping is performed before the bit stuffing stage when constructing the AIS message for transmission. At reception, the bits are flipped back in the original order after the removal of bit stuffing.

Bit stuffing

Bit stuffing is a line code process that inserts extra bits into a stream without adding new information that would affect the synchronism of communications. It allows the AIS to transmit any sequence of bits without worrying about the possibility of a flag pattern being inadvertently reproduced inside the message bit stream, which would interfere with the receiver's ability to synchronize and detect

Table 1.3: AIS message bits for messages 1, 2 and 3

Parameter	**Number of bits**	**Description**
Message ID	6	Identifier for message type 1,2 or 3.
Repeat indicator	2	Number of times a message has been repeated.
User ID	30	Unique identifier such as the maritime mobile service identity (MMSI) number.
Navigational status	4	Vessel status code. Indicates ship situation like anchored, fishing, among others.
Rate of turn (ROT)	8	Ship rotation rate based in degrees per minute.
Speed over ground (SOG)	10	Speed over ground in 1/10 knot steps.
Position accuracy	1	Position accuracy based on electronic position fixing device. Indicates if precision is $\leq$ 10 meters.
Longitude	28	Latitude in 1/10 000 minute.
Latitude	27	Latitude in 1/10 000 minute.
Course over ground (COG)	12	Direction of vessel with respect to earth's surface in 1/10 of degree.
True heading	9	Vessel direction with respect to the north in degrees.
Time stamp	6	Universal coordinated time UTC Time in seconds when the report was generated by the position system.
Special manoeuvre indicator	2	Code indicating that a special manoeuvre is in execution.
Spare	3	Not used.
RAIM-flag	1	Receiver autonomous integrity monitoring (RAIM) flag indicating the use of electronic position fixing device.
Communication state	19	AIS communication related data for slot allocation and synchronization.

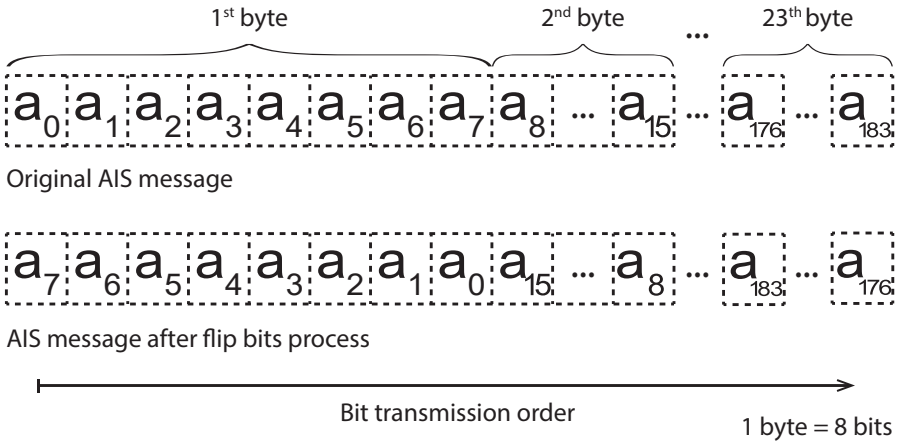

Figure 1.3: Flip bits applied to the AIS data

AIS packets. Bit stuffing also creates extra transitions for long bit sequences that help to recover receiver synchronization and protect from clock drift.

For AIS transmission, bit stuffing shall append an extra bit "zero" immediately after a sequence of five "ones". The bit stuffing process is represented in Figure 1.4. At the reception side the process is reversed, where the first zero that appears after five consecutive ones are removed from the bit stream in order to recover the original message. Notice that only the message part (the data and CRC blocks) is subject to bit stuffing.

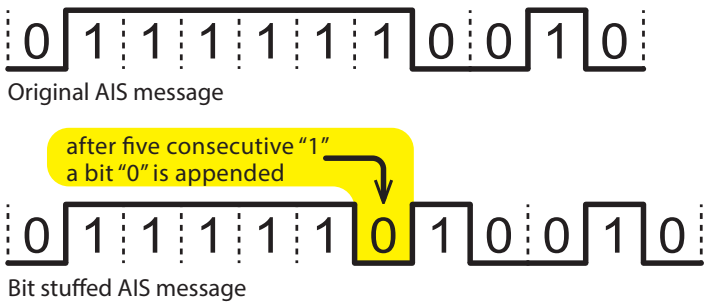

Figure 1.4: Bit stuffing process during the construction of the AIS packet

NRZI line coding

After bit stuffing, the entire AIS packet is encoded. The AIS uses NRZI line coding. For each bit "zero" found in the bit stream the coding produces a level transition. The output level stays at the same level for each "one" bit in the bit stream. Encoding is done by the following relation

$$b_k = \overline{a_k \oplus b_{k-1}} \tag{1.1}$$

where the bit a_k represents the k-th input bit to be encoded, b_k the k-th output and $\oplus$ is the XOR binary operator. Note that NRZI uses differential encoding which introduces memory to the signal. At reception, the NRZI bit stream is decoded by detecting the state of current bit and comparing it with the previous transmitted bit, that is

$$a_k = \overline{b_k} \oplus b_{k-1}. \tag{1.2}$$

GMSK modulation

The GMSK is a type of continuous-phase modulation (CPM). It is a non-linear modulation where the output phase is constrained to remain continuous. The information is only contained in the phase of the transmitted signal. The output signal has memory introduced through the imposition of phase continuity [PS08]. In CPM, each symbol is modulated by continuously changing the phase of the carrier over the symbol duration. One characteristic is that the memory of cumulative phase from previous transmitted symbols is necessary to demodulate a symbol from the signal.

The complex envelope of a general CPM waveform is

$$s(t) = Ae^{j(\phi(t)+\theta_0)} \tag{1.3}$$

where A is the amplitude, θ_0 is the initial phase at instant $t = 0$ and $\phi(t)$ is the carrier phase defined for CPM signals as

$$\phi\left(t; \boldsymbol{I}\right) = 2\pi \sum_{k=-\infty}^{n} I_k h_k q\left(t - kT\right), \quad nT \leq t \leq (n+1)T, \tag{1.4}$$

where $\{I_k\}$ is the sequence of M-ary information symbols selected from the alphabet $\pm 1, \pm 3, \ldots, \pm(M-1)$, $\{h_k\}$ is a sequence of modulation indices, and $q(t)$ is the frequency shaping function, which is some normalized waveform that is used to shape the output signal [Stü00].

The waveform $q(t)$ may be represented as the integral of some pulse $g(t)$, i.e.,

$$q(t) = \int_0^t g(\tau)d\tau \tag{1.5}$$

Considering $g(t)$ a signal pulse with duration limited between $[0, LT]$, T being the symbol period and L the duration of $g(t)$ in number of symbols, the duration LT of the pulse $g(t)$ defines if the modulated signal is a full or partial-response CPM. In a full-response CPM, the demodulation of a symbol depends on the memory of cumulative phase from the last transmitted symbol ($L = 1$). For partial-response CPM, $L > 1$ symbols and the demodulation depends on the cumulative phase of the $L - 1$ last data symbols. This introduces memory to the modulated signal.

GMSK is a special type of partial response CPM that uses a rectangular pulse with Gaussian pre-modulation filter to create the shaping pulse $g(t)$. As a result, the GMSK modulation yields a Gaussian shaping waveform pulse

$$g(t) = Q\left[\frac{2\pi B}{\sqrt{\ln 2}}\left(t - \frac{T}{2}\right)\right] - Q\left[\frac{2\pi B}{\sqrt{\ln 2}}\left(t + \frac{T}{2}\right)\right] \tag{1.6}$$

where $Q(\alpha)$ is the Gaussian cumulative error function with

$$Q(\alpha) = \int_\alpha^\infty \frac{1}{\sqrt{2\pi}} \exp^{-x^2} dx \tag{1.7}$$

B being the bandwidth of the Gaussian filter (defined by the -3 dB cutoff frequency) and the pulse limited at the interval $[-LT/2, LT/2]$. In AIS communications the GMSK modulation uses binary symbols ($M = 2$) with $I_k = \pm 1$. The total pulse area is $\int_{-\infty}^{+\infty} g(t)dt = 1/2$ and the contribution to the excess phase for each symbol is $\pm\pi/2$.

The parameters of the GMSK modulation are the index $h = 0.5$ and the time-bandwidth product $BT = 0.4$. Following from ITU-R recommendation M.1371-5, AIS class A communications use $B = 25$ kHz (formerly the AIS prior dual bandwidth optionally had a 12.5 kHz narrow operation band which is now obsolete). The period $L = 3T$ gives the truncation time of 16 μs. The resulting AIS parameters are displayed in Table 1.4.

Table 1.4: GMSK parameters in AIS Class A communications

Parameter	**Value**
Bit rate $1/T$	9600 bits/s
Time-bandwidth product BT	0.4
Modulation index h	0.5
Bandwidth B	25 kHz

AIS signal model at the ship transmitter

The AIS signal model during transmission can be modeled as

$$s_{\text{AIS}}(t) = e^{i\phi(t;\boldsymbol{I})} \tag{1.8}$$

with

$$\phi(t;\boldsymbol{I}) = \pi \sum_{k=-\infty}^{n} I_k q(t - kT), \quad nT \leq t \leq (n+1)T, \tag{1.9}$$

and where the bits $I_k = \pm 1$ belong to a binary alphabet, $q(t)$ is the Gaussian waveform defined by (1.5) and the pulse $g(t)$ is defined by (1.6).

1.3.4 Satellite reception of AIS signals

In a space based AIS, the AIS coverage may be close to the size of the satellite footprint because AIS reception is possible at low elevation angles. For reference, a low orbit satellite (whose altitude goes from 200 km to 2.000 km) has a footprint between 1.5% to 12% of the Earth's surface area [MA14].

As described earlier, the AIS system was created for ship-to-ship communications. Thus, some characteristics of the AIS system were not optimized for satellite communications. For instance, low SNR conditions may be balanced thanks to the use of error correction techniques, but bit stuffing makes the use of such methods very complicated (but still possible) [PCB+13]. Despite of that, satellite AIS have proved viable [ITU09; CGE11; EHNM06; WHLN05; Pré12; LM13] and AIS receivers have been embedded into satellites [LM13] raising some extra difficulties. Message collisions, attenuation and Doppler distortion are common problems that need to be considered in AIS transmissions [ESN+10].

Satellite reception of AIS signals has some peculiar differences with respect to maritime direct communications. For example, there is attenuation due to the involved distances (between the emitter and the receiver). The distance between ships and the satellite may be 10 times more important than traditional AIS ship-to-ship communications [Pré12]. As consequence satellite reception of AIS implies greater noise levels and needs to deal with important bit error rate (BER) in comparison with standard ship-to-ship communications.

The AIS signal transmission efficiency depends also on antenna directivity. Ship's antennas are usually conceived to reach other vessels that are in the horizontal line of sight, being not really optimized for satellite reception at higher elevation angles.

Another particularity related to satellite reception is the Doppler distortion. This occurs due to the Doppler effect induced by the relative radial velocity between satellite and transmitting ships. Figure 1.5 shows an example of the Doppler distortion for a satellite with an AIS receiver located at 500 km of altitude where the Doppler shift is between $+4$ kHz and -4 kHz, giving a maximum perceived Doppler of 8 kHz between two AIS messages. For reference, two AIS messages that occurs at the same instant may not be separated by spectral filtering due to the Doppler being inferior to the signal bandwidth of 9600 Hz.

Another known problem is signal model mismatch that may occur due to the existence of ships carrying low cost AIS transmitters (in particular, with modulation indexes different from the AIS standard). This may increase the complexity of AIS reception as the receiver needs to estimate the correct modulation index and the original transmitter frequency of the AIS transmitted signal.

A relevant problem in satellite AIS reception is the higher occurrence of AIS packet collisions. This is due to in the fact that the satellite antenna footprint generally covers an area many times greater than an AIS resolution cell. AIS transmissions are scheduled to work with ships that are within a certain range, and ships that are further than one AIS cell range are not coordinated for appropriate satellite reception (they may occupy the same time slot). As consequence, a much larger number of vessels are covered by the satellite swath and transmissions from different AIS cells may appears at the satellite point-of-view as an excessive reuse of AIS time-slots, increasing the number of message collisions. Some AIS reception problems were addressed in [Pré12].

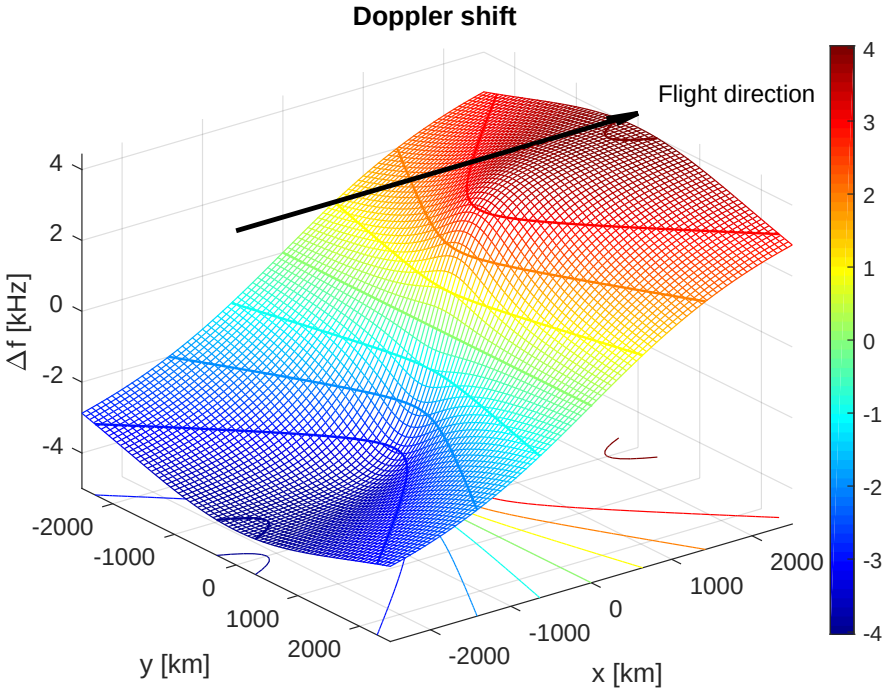

Figure 1.5: AIS signal Doppler shift distribution under the satellite footprint area

AIS signal model at the satellite receiver

The following signal model considers the reception of a unique AIS signal by the satellite receiver without collisions. The AIS signal being narrow-band can be represented as follows

$$r_{\text{AIS}}(t) = A s_{\text{AIS}}(t-\tau) e^{i(2\pi f_D t + \theta)} + n(t), \tag{1.10}$$

where $r_{\text{AIS}}(t)$ is the received AIS signal, A is an attenuation coefficient, $s_{\text{AIS}}(t)$ is the transmitted AIS signal model from (1.8), τ is the delay due to the propagation time of the AIS signal, f_D is the frequency offset due to satellite Doppler, θ is the value of the signal phase at reception due to the distance between the satellite and the ship transmitter, and $n(t)$ is the noise modeled as additive white Gaussian.

1.4 Radar

Radars use electromagnetic waves in order to extract information about the objects that are being observed. They are valuable because of their ability to perform measurements, detection, localization, imaging and also to extract information about the illuminated targets without depending on target cooperativeness. Radar systems have very interesting attributes. They are well known for the high accuracy of their measurements and for being resilient to adverse atmospheric conditions. As active sensors, they are able to operate during the day or night without directly depending on the sunlight like optical sensors. In addition, the frequency selectivity of radar allows imaging in different weather conditions (like in case of cloudy or rainy weather) where imaging with optical sensors would be compromised. Those characteristics brought attention of a wide variety of applications. Radars became very popular for military purposes, remote sensing, traffic control, surveillance, safety, navigation, space observation and many other applications [Sko02]. Radars may be adopted to investigate objects that are masked, covered or beyond visual perception, whereas others may use radars to localize, measure and analyze. Radars may also be used to sense and measure the environment, e.g., to gather information about atmospheric events like winds, snow, rain, clouds or sea waves. Radar targets may be on ground, sea, air, space, underground, behind clouds, trees, or even walls.

Among the many available types of radars, the imagery radar has proven its importance in observation, vigilance, measurement and many other applications. In traditional imaging radar systems the angular resolution depends on the ratio between radar signal wavelength to the antenna aperture size. The spatial resolution is the angular resolution times the distance between the radar sensor and the surface to be imaged. As distance increases, the spatial radar resolution decreases unless the physical size of the aperture is increased. At wavelengths in the visible and near infrared spectrum high resolution images can be obtained with sensor apertures of reasonable sizes even at orbital altitudes. However, for conventional radar imaging with spaceborne instruments operating at typical wavelengths of five orders of magnitude longer than light, high resolution is impracticable [CM91]. For example, a radar operating at 20 cm wavelength with 10 m aperture antenna embedded

into a satellite at 500 km altitude orbit would produce images with spatial resolution of 10 km using the real antenna aperture. Considering conventional radar imaging process it would be necessary to greatly increase the antenna aperture size to improve image resolution. Returning to the same example, to achieve 20 m resolution it would be necessary an antenna aperture of 5 km, which is unfeasible.

Synthetic aperture radars (SAR) are a group of special imagery radars that, in their basic form, are able to create two- or three-dimensional images using the synthetic aperture radar technology. SAR reproduce a synthetic aperture that is many times longer than the antenna real aperture. In consequence, azimuth resolution may increase far beyond conventional radar resolution limit and it is possible to reach high azimuth resolution with reasonable size antennas. This however has the cost of the assumption that the targets are stationary with respect to a moving radar. The term "synthetic" comes from the signal synthesis that is based on using the radar motion to synthesize a virtual antenna far longer than the real one (see Figure 1.6). In the figure λ is the wavelength, L_a is the antenna length, R is the range from the radar to the target, V_s is the radar platform speed and L is the synthetic aperture length.

SAR imaging is performed by mapping the received signal energy into the image pixels that correspond to a location inside the illuminated radar area. Each pixel in a SAR image corresponds to a calculation done on the received signal in order to concentrate the energy into the pixels that correspond to the target positions. SAR processing is responsible to improve cross-range (azimuth) resolution. However, the high azimuth resolution obtained incentive SAR designers to use pulse compression in order to improve the range resolution. As a result, SAR is known to produce high-resolution radar images in both range and azimuth directions. Another interesting aspect of SAR processing is that the spatial resolution does not depend on the target distance like conventional radar. This makes the SAR a valuable instrument for applications that need to deal with important propagation distances.

The SAR process is the only technique that leads to high resolution imaging at the long ranges involving space-based observation [UMF86; GAS+17]. This among other advantages allowed SAR to consolidate its presence in satellite radar imaging, being currently used by the majority of satellites

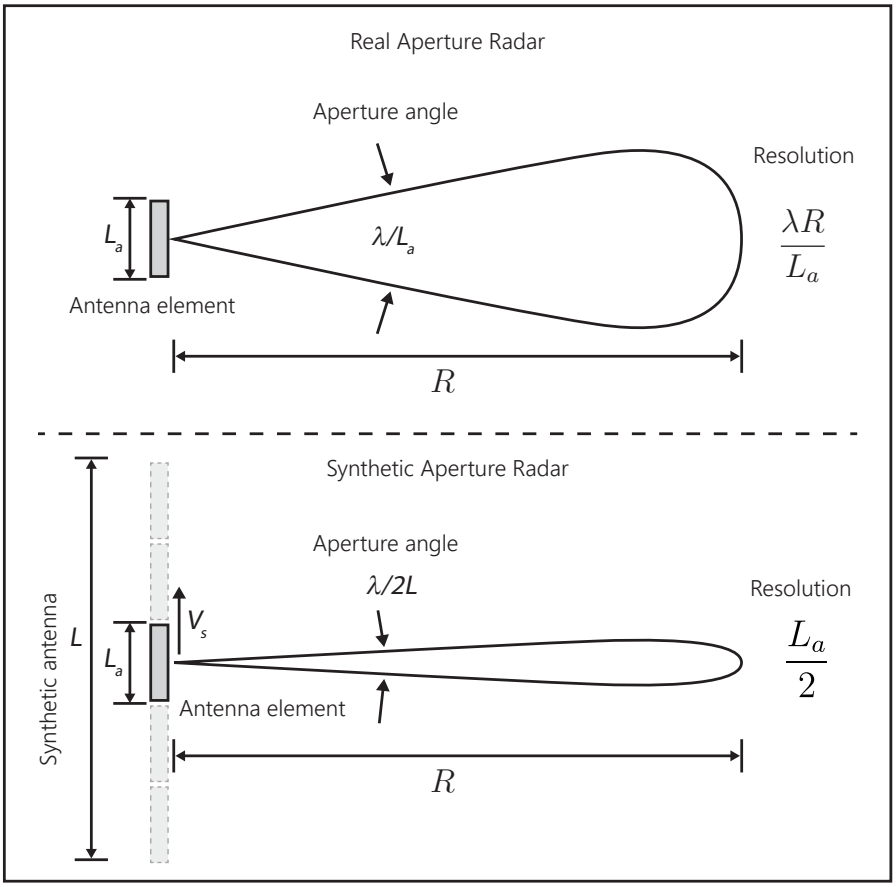

Figure 1.6: Representation of real and synthetic apertures.

embodying radar imaging services. Usually, satellites embedding SAR sensors operate in a near circular low-Earth orbit (LEO) spanning altitudes between 500 km to 850 km [Sko08]. They usually cover surface areas with length from tens to a few hundreds of kilometres, depending on the radar design and the SAR operation mode [MVS15].

SAR is an interesting tool for target detection and imaging in space-based platforms. It is frequently used in surveillance applications that demand high availability with the ability to operate in all-weather situations even in adverse atmospheric conditions. Space-based SAR systems have been used for earth observation and are well known for their ability to generate high resolution images of the Earth's surface. They are able to provide important details about the imaged targets

such as dimensions, orientation and its geographic location.

There are basically three types of SAR operation mode: “stripmap”, “scan” and “spotlight” SAR (Figure 1.7).

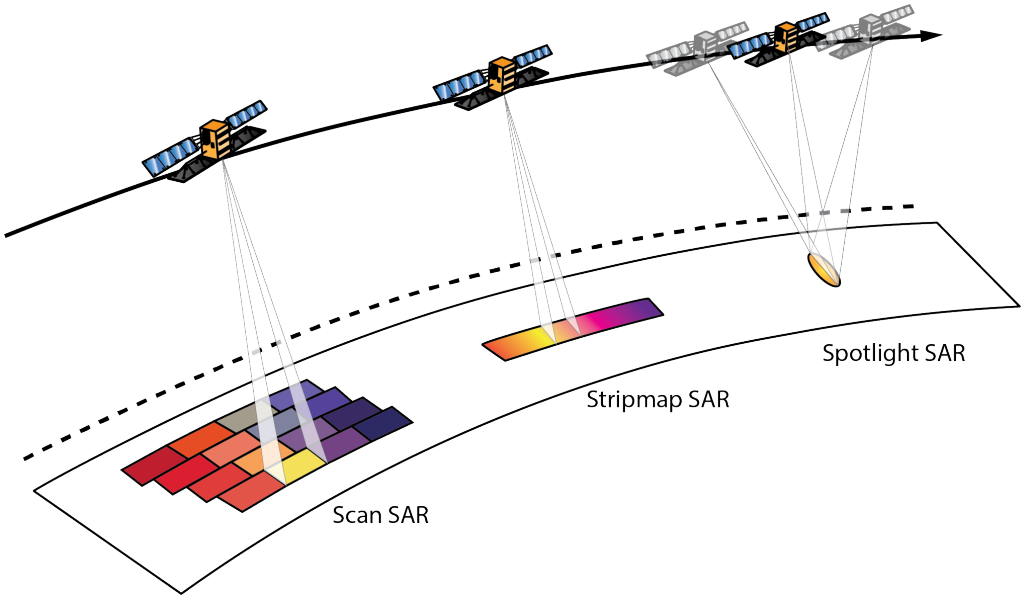

Figure 1.7: Illustration of the three main SAR operation modes.

In the stripmap mode, the radar antenna is fixed with respect to the moving platform while the radar footprint illuminates a constant strip of the earth surface parallel to the platform path of movement. In this mode, the radar antenna may be pointing normal to the radar moving trajectory (broadside) or pointing the earth surface at a fixed and usually small squint angle forward or behind the normal to the radar platform movement path. The maximum synthetic aperture length in stripmap mode cannot exceed the azimuth width of the radar beam footprint on the ground. This occurs because the radar beam fixed angle with respect to the moving platform limits the maximum viewing angle that a point target on the ground is illuminated to be inside the antenna aperture length.

In the spotlight mode, the SAR antenna is forced to continuously image a specific area at the imaged surface by steering the radar beam to compensate the radar platform movement. Spotlight steering of the radar beam allows focus at a single target area at greater squint angles, producing

even longer radar exposition of a particular illuminated area, increasing the synthetic aperture size. The maximum synthetic aperture length in spotlight mode may be even longer than the synthetic aperture in stripmap mode. As SAR steers the radar beam to keep the target zone under the antenna view it may reach the target at larger viewing angles. By consequence, the synthetic aperture size is increased beyond stripmap synthetic aperture limit, providing even finer azimuth resolution when compared with stripmap. As a downside, the resolution improvement comes in exchange for a much smaller coverage area. As spotlight mode needs to steer the radar beam at the desired spot on Earth's surface it does not observe the entire azimuth extent as the stripmap does.

The SAR scan mode is an operation that also steers the radar beam to image. However, the scan mode sweeps the imaged area in different ways in order to image at a desired resolution and radar coverage. Steering in spotlight also allows a scene to be imaged at multiple viewing angles and different ground patches to be considered dynamically.

1.4.1 Radar principles

This section presents an overview of SAR system.

The SAR is a coherent radar system, meaning that the phase between the transmitted pulses are preserved. SAR processing uses the coherent transmissions and the returned echoes to image and geographically map targets at an imaged scene. During the satellite moving trajectory, the SAR regularly transmits a radar signal to the imaged surface. Those transmissions collide at the illuminated surface where the signal is backscattered to different directions. A part of the signal energy is reflected back to the radar direction. The receiver is ready to register the returned signal in the form of a raw signal to be processed. The amount of energy recovered depends on factors related to electromagnetic wave propagation, e.g., the antenna gain and directivity, the attenuation due to the propagation medium. Some important factors related to power transmission are propagation distance, atmospheric absorption, surface reflectivity, target geometry, among others.

Due to the radar displacement in orbit movement, the radar signals are transmitted and then acquired at different positions along the movement track of the radar platform. Targets in the radar line of sight are repeatedly illuminated at different azimuth viewing angles while still inside the radar

antenna aperture (see Figure 1.8).

The SAR principle is based on the observation that, at any instant, point targets with even slightly different angles with respect to the radar movement path will have different radial speeds in the radar point of view [CM91].Consequently, the signal returns from those targets will have distinct Doppler frequency shifts accordingly to their angle to the antenna during reception. Similarly, target distance to the satellite are distinguishable by the time delay τ of after the two-way propagation of the radar signal. The time delay is given by

$$\tau(t) \approx 2R(t)/c \tag{1.11}$$

where $R(t)$ is the radial distance of the antenna center to the target, c is the speed of the light and the factor 2 is due to the two-way wave propagation common in active radar systems.

The location of a target at the Earth surface may be described in terms of their coordinates relative to the radar positioning. The SAR system performs a reversible transformation of coordinates from the ground range y and along track position x to observable coordinates, pulse delay τ and Doppler

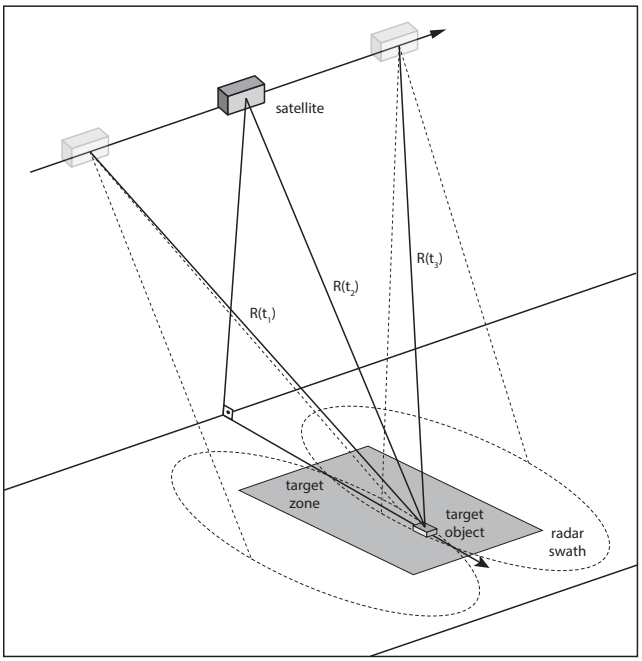

Figure 1.8: Representation of SAR satellite illuminating a target at ground.

shift f_D using the echoed radar signal. There are some other factors that impact the target positioning measurement. For example, Earth rotation and some uncertainties with respect to the radar orbit trajectory may need additional steps in the SAR processing to compensate their effects in the return signal. Likewise, non-stationary targets would need an additional step to identify and compensate the effect of extra Doppler modulation in the radar return signal.

1.4.2 SAR geometry

Suppose a satellite carrying a SAR in orbital movement over the Earth. The satellite distance along path is denoted as a coordinate in the x axis. Consider a satellite in circular motion over a spherical earth in which the platform trajectory does an arc with constant height above earth surface. This consideration means that the uncertainties in satellite radial speed and differences in orbit geometry have been compensated. Consider that the radar uses synthetic aperture processing. The antenna is placed broadside on the platform track. The radar beam center points towards the earth surface at a fixed look angle with respect to the satellite platform. When moving in the azimuth direction, the radar swath illuminates a constant strip zone of the Earth surface along the satellite displacement path. In the SAR nomenclature operating in stripmap SAR mode. For sake of simplicity, we consider the radar as operating broadside (no squint angle).

Considering a single small area of interest, our model may consider a satellite SAR in near linear movement at certain altitude h with uniform speed V_s in the x direction (See Figure 1.9). The radar will perceive a Doppler for targets according to their radial speed V_r with respect to the satellite. Targets that produce identical Doppler shift f_D are those positioned on the surface of a cone with central axis along with the radar axis of movement. Similarly, targets that produce identical time delays τ are those at the same radial distance over a sphere centered at the radar position. The intersection of those geometries with the ground plane containing the targets produce iso-Doppler and iso-range lines (see Figure 1.10). The targets positioned at the same contour line share the same respective coordinates in a two-dimensional mapping.

The zone of interest in SAR is broadside the movement trajectory of the satellite. At this direction, the iso-range and iso-Doppler lines are almost orthogonal (have very low coupling between range and

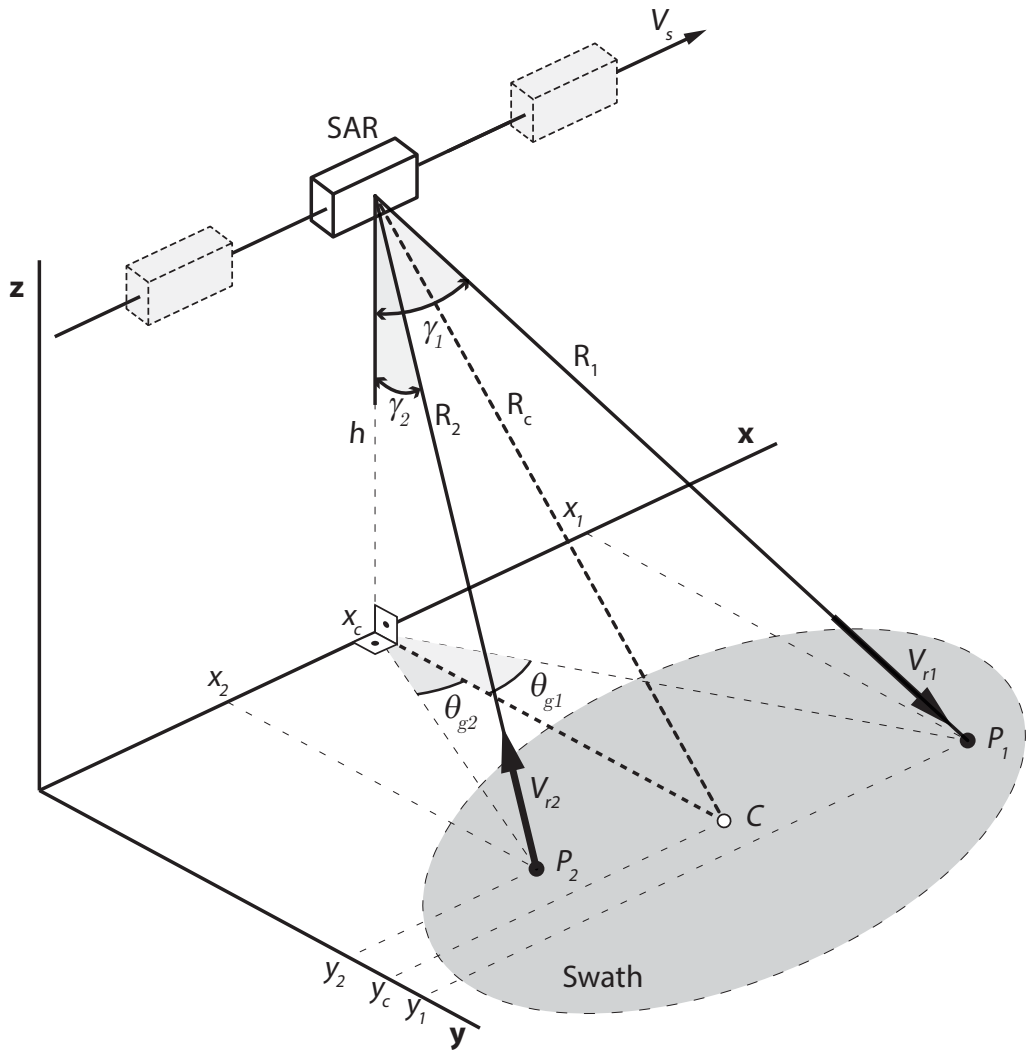

Figure 1.9: SAR geometry: Coordinates from two targets P_1 and P_2 based on range and Doppler parameters.

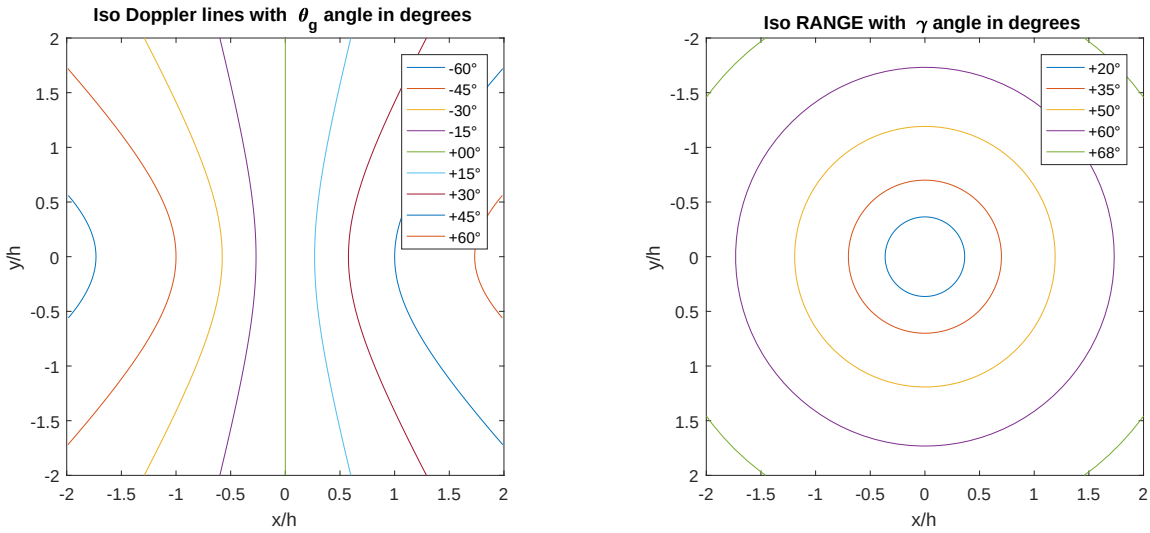

(a) Lines of constant Doppler shift. θ_g is the target angle at the ground plane with respect to the range direction.

(b) Lines of constant range distance. γ is the looking angle of satellite towards the ground plane.

Figure 1.10: The Iso-Doppler and iso-range contours geometry at the surface

Doppler), serving as pair of planar coordinates. One may use the transmission timing, namely the slow time and fast time as the coordinate pair related to deal with the radar sampling times. Slow time samples are related to the Doppler while fast time samples are related to the time between samples. The slant range and the ground planes are also used to represent the imaged area [Sko08].

The slant range R and azimuth distance y are coordinates usually used to alternatively represent the imaged area instead of direct working with the ground coordinate pair (x, y). This happens because the slant range R is a distance coordinate directly associated with the propagation time delay τ of the radar signal that is directly measurable. It defines the radial distance from the radar antenna to the target and is coupled with the ground coordinates. The Doppler information is used to decouple range from azimuth to obtain the ground coordinates.

Considering the radar signal at the receiver acquired at a constant sampling rate, the signal uniformly sampled in time represents ground samples spaced in a non-uniform manner. This occurs because radar sampling is uniform in range direction, which is non-linearly related to the ground

samples by the variable angle of incidence (see Figure 1.11). The incidence angle ϕ of the radar beam is not constant. At near range distances, the incidence angle $\phi(R_{\text{near}})$ is smaller than the look angle at far ranges $\phi(R_{\text{far}})$. This means that returns from targets at the near range area arrive on the radar receiver more closely spaced than samples taken from far range distances. As a result of uniform sampling there is a non-uniform mapping between slant range and ground range and the target area will appear distorted in the radar image.

Despite the non-uniform map in the ground coordinates x and y, they are necessary when the radar image needs to be associated with images from a different sensor such as optical images, or when radar need to be associated with positions referenced in ground coordinates, or when land masking is required. An appropriate transformation and interpolation is necessary in order to properly represent the radar images in ground coordinates.

SAR range resolution

The resolution of the radar in range is defined as the minimum range separation of two points that can be distinguished by the radar system [CM91]. Without pulse compression, range resolution is determined by the pulse duration T and the maximum separation between two resolvable echoes is given by $\delta R = cT/2$, where δR is the resolution in slant range. In the same way the ground range resolution becomes $\Delta y = cT/2 \sin(\phi(R))$ where $\phi(R)$ is the incidence angle of the radar wave at the target position defined by the slant range R (radial distance).

Narrowing the pulse width improves the radar range resolution. However, the transmitted power is also directly related to the duration of the radar pulses, which means that signal power is related to radar range resolution. As a consequence, reducing pulse width also reduces the transmitted signal power, degrading the radar signal-to-noise ratio (SNR). This can be troublesome for applications where the resources are limited like with spatial SAR systems. In addition, spatial SAR also need to deal with important attenuation due to the greater propagation distances involved and transmitting power is an important parameter. The use of pulse compression may resolve this problem. It decouples the pulse width T from the range resolution δR, so that range resolution may be improved without affecting the signal transmitted power. The range resolution and the ground range resolution

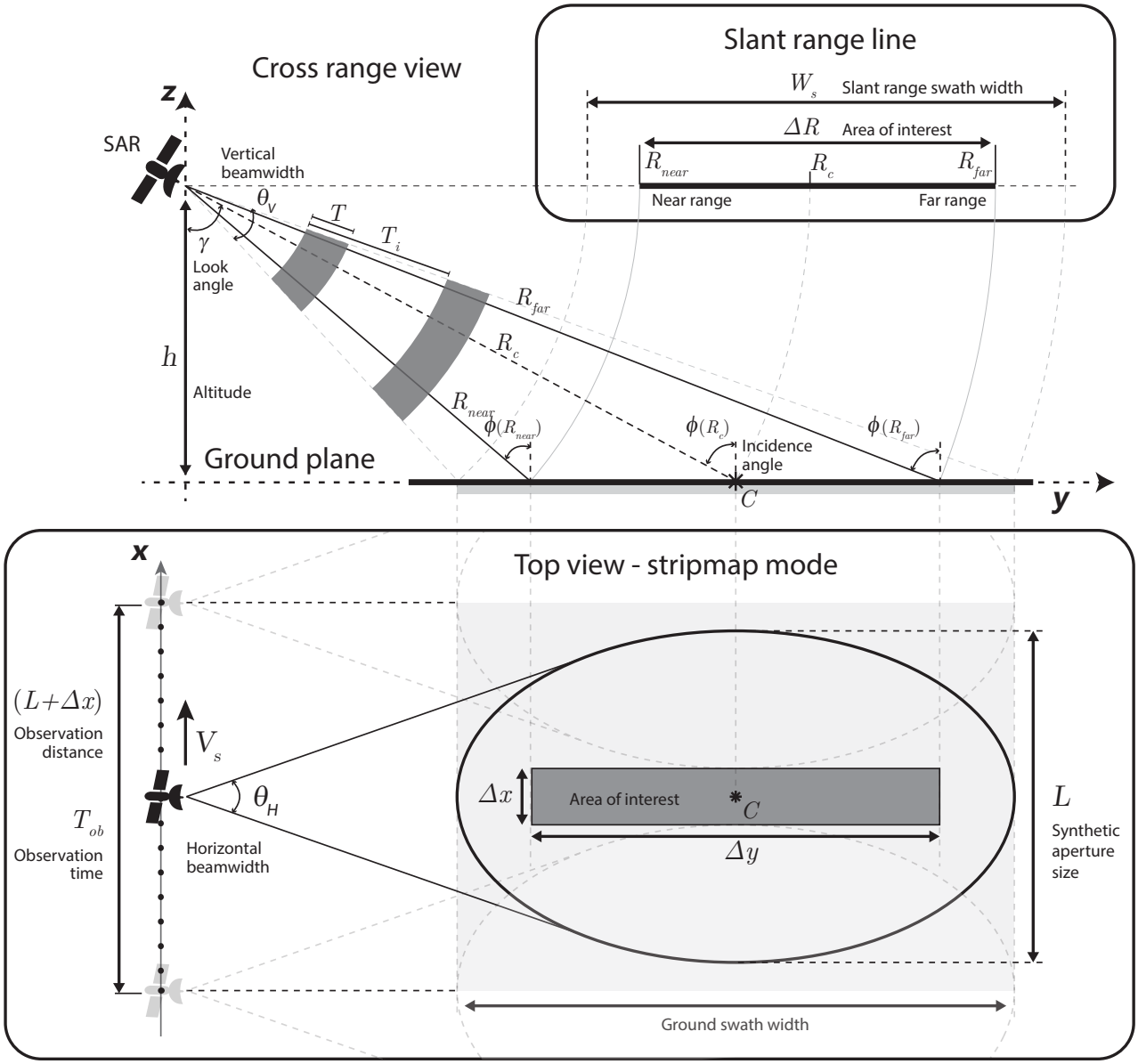

Figure 1.11: SAR geometry: Contains the ground plane, slant plane and upper view of the SAR geometry process for stripmap SAR operation.

for pulse compressed radar signals are given by

$$\delta R = \frac{c}{2B_0}, \qquad \delta y = \frac{\delta R}{\sin(\phi)}, \tag{1.12}$$

where B_0 is the projected pulse bandwidth. Range resolution improves as the signal bandwidth is increased. However, this also increases the receiver minimum sampling rate required to properly sample the entire pulse bandwidth B_0.

SAR azimuth coverage

Consider the radar operating in stripmap mode with the antenna fixed angle pointing broadside (according to Figure 1.11). Consider a radar antenna with length L_a in the azimuth direction (see Figure 1.6). The radar azimuth beamwidth has angular spread in azimuth direction equals to

$$\theta_H = \lambda / L_a \tag{1.13}$$

where λ is the wavelength of the transmitted radar signal. The azimuth distance on the ground covered by the antenna beamwidth is

$$X = R\theta_H = R\lambda / L_a \tag{1.14}$$

where R is the slant range distance.

SAR Doppler and azimuth coordinate

The received radar signal from a pointwise target at some slant range R and along-track coordinate x is perceived as having a modulation from its original frequency. The Doppler shift is proportional to the target azimuth angle with respect to the radar antenna center (see Figure 1.9). The Doppler shift is given by

$$f_D = \frac{2V_{st}\cos(\theta_g)}{\lambda} \approx \frac{2V_{st}x}{\lambda R} \tag{1.15}$$

which V_{st} is the satellite azimuth speed relative to the target, θ_g the target angle off broadside and the factor 2 results from the two-way travel of the radar wave that is intrinsic in active systems.

Imaged targets may be discriminated in azimuth by associating azimuth position x with the signal Doppler deviation with

$$x = \frac{\lambda R}{2V_{st}} f_D \tag{1.16}$$

f_D being the Doppler shift. Consider δx as the minimum distance to resolve two neighbor targets in the azimuth direction. Denoting as δf_D the resolution of the Doppler measurements (to resolve targets at δx distance) and using (1.16), the azimuth resolution δx using SAR focused processing is

$$\delta x = \left(\frac{\lambda R}{2V_{st}}\right) \delta f_D. \tag{1.17}$$

The resolution of the Doppler measurement is nominally the inverse of the time span $\delta f_D = 1/S$, which is the time during any particular target is in view (period that a punctual target remains illuminated by the radar).

SAR synthetic aperture size

Considering the radar operating in the stripmap mode (that is, with the antenna in a fixed angle), the size of the radar beamwidth on the ground is defined in azimuth by the aperture size of the radar antenna in both range and azimuth directions. From the Figure 1.11, θ_H is the maximum azimuth angle that a target is visible by the radar antenna. Considering (1.13), a target is observable during the timespan

$$S = \frac{R\theta_H}{V_{st}} = \frac{R\lambda}{L_a V_{st}}. \tag{1.18}$$

The synthetic aperture length is the distance in azimuth that the SAR satellite passes while still observing the same point target on ground. During the timespan S, the satellite displacement is $L = SV_{st}$, which is identical to the radar azimuth beamwidth on the ground for the range distance R. From (1.17) and (1.18) the synthetic aperture L may be written

$$L = \frac{\lambda R}{2\delta x}. \tag{1.19}$$

SAR azimuth resolution

From equations (1.17) and (1.18) the azimuth resolution of the stripmap SAR may be written as

$$\delta x = \left(\frac{\lambda R}{2V_{st}}\right)\left(\frac{L_a V_{st}}{\lambda R}\right) = \frac{L_a}{2}. \tag{1.20}$$

This result states that azimuth resolution with SAR only depends on the size of the real antenna azimuth length L_a.

SAR constraints

Some practical issues limit the use of very small antennas. Reducing the antenna azimuth length L_a enlarges the radar azimuth beamwidth and broads the view angle that targets are observable by the radar beam. However, it also degrades the radar SNR because smaller antennas have reduced antenna aperture and, by consequence, inferior power transfer effectiveness.

Another limitation is the use of a pulsed radar to image in both range and azimuth. From Figure 1.11, we observe that the reception time of the earliest possible echo from any point in the swath needs to occur after reception of the echoes from a previous transmitted pulse. This limitation is necessary to avoid collision of echoes from far and near ranges originated from different transmitted pulses at the SAR receiver.

The inferior bound for the radar pulse repetition interval T_i is

$$\Delta R = R_{\text{far}} - R_{\text{near}} < cT_i/2 = c/\left(2f_p\right) \tag{1.21}$$

which f_p is the radar pulse repetition frequency (PRF).

Another requirement is the Doppler frequency shift related to the azimuth ambiguity. To avoid ambiguities, the frequency bandwidth B_D of the Doppler signal must be less than the PRF ($B_D < f_p$), which gives a lower bound to the radar PRF f_p

$$B_D = f_{\text{D,high}} - f_{\text{D,low}} = V_{st}/\delta x < f_p. \tag{1.22}$$

This means that the radar must transmit at least one pulse each time the radar platform travels a distance equal to one half of the antenna length to remain unambiguous in azimuth.

Those inequalities yield another requirement for the antenna area as a lower bound for full resolution SAR of [CM91, Curlander p.21]

$$A_a = L_a W_a > 4V_{st}\lambda R_c(\tan\phi)/c \tag{1.23}$$

where A_a is the antenna area, W_a is the antenna height, R_c is the slant range to the center of the target area, ϕ is the incidence angle at the imaged area center.

1.4.3 Radar signal model

This section summarizes the SAR signal model considered in this thesis.

The SAR transmitted signal is usually a burst containing one sequence of narrow bandwidth pulses. The radar signal before transmission is represented by the pulse stream

$$p(t) = \sum_{h} \psi(t - hT_i) \tag{1.24}$$

where T_i is the pulse repetition interval, h the integer representing the pulse number, t the time and $\psi(t)$ is the pulse waveform. SAR system have different types of waveforms for pulse compression. The most common type of waveform is the linear frequency modulation (LFM). The LFM waveform is defined by

$$\psi(t) = 1_T(t) e^{jK_r t^2} \tag{1.25}$$

where $1_T(t)$ is the indicator function on the interval $]-T/2, +T/2[$, which T is the pulse duration and K_r the chirp rate parameter. A positive chirp rate parameter represents an upchirp (frequency rising chirp) and negative a downchirp (frequency decreasing chirp). The pulse waveform is a quadratic phase in t, where is a linear frequency modulation. This waveform modulates the transmitted pulse, denoted by the indicator function $1_T(t)$, into an LFM waveform usually known as a chirp (see Figure 1.12).

The SAR signal is mixed with the carrier frequency f_0 before transmission. The transmitted SAR signal can then be written as

$$s_\mathrm{rad}(t) = \sum_{h=1}^{N_P} \psi(t - hT_i) e^{j2\pi f_0 t} \tag{1.26}$$

where N_p is the number of transmitted pulses.

From the geometry in Figure (1.11), we can see that the observation time is

$$T_\mathrm{ob} = (L + \Delta x)/V_{st}. \tag{1.27}$$

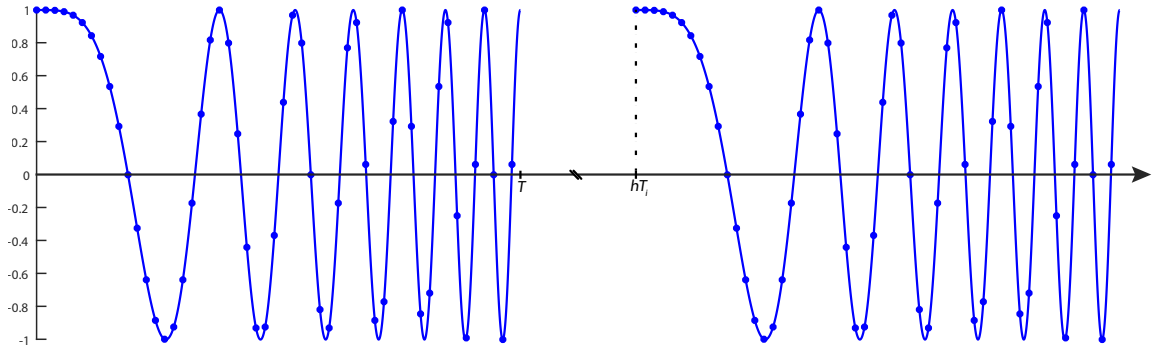

Figure 1.12: The sampled LFM signal before transmission (waveform in baseband).

During the observation time T_{ob}, the radar travels a distance that covers the synthetic aperture length L plus the azimuth length of the area of interest Δx. T_{ob} is the time during which the radar covers the entire area of interest in the observable angle limit. The quantity of pulses transmitted during this period is

$$N_p = T_{\text{ob}} f_s \tag{1.28}$$

which N_p is the number of samples needed to image the area of interest.

Consider a scene where there is only one target at a given position $\boldsymbol{\theta} = (x, y)^T \in \mathbb{R}^2$ and where (x, y) is the target ground coordinates in the local scene. Denote as $\tau_{\boldsymbol{\theta}}$ the time duration of the radar signal to propagate to the target position $\boldsymbol{\theta}$ and return to the radar receiver. At some time t when the satellite is at some slant range distance $R(t)$ from the target, the radar signal echo received from this target is

$$r_{\text{rad}}(t) = ap(t - \tau_{\boldsymbol{\theta}}(t)) \tag{1.29}$$

where a is a scale factor that is locally constant at the slant $R_\theta(t)$, and the delay is $\tau_{\boldsymbol{\theta}}(t) \approx 2R_\theta(t)/c$. From equations (1.24) and (1.29), the received pulse train quadrature demodulation signal is then

$$r_{\text{rad}}(t) = \sum_{h=1}^{N_P} a_h \psi(t - hT_i - 2R_\theta(t)/c) \tag{1.30}$$

where a_h is an amplitude scale factor for the h^{th} pulse. This formulation shows that received pulses $\psi(t - hT_i - 2R(t)/c)$ are delayed and distorted versions of transmitted pulses $s_{\text{rad}}(t - hT_i)$. The distortion varies with the range $R_\theta(t)$ that depends on the geometry along with the radar displacement.

The term $\tau_{\boldsymbol{\theta}}(t)$ in is a hyperbolic form which is near quadratic during the time the target is in view (inside the antenna aperture) for the SAR in stripmap mode operating in the broadside direction (without squint angle). The quadratic range term produces a Doppler modulation to the transmitted radar signal that is related to the satellite radial speed V_r. In practice, the induced Doppler is almost negligible for the fast time samples, as the slant range does not vary significantly during the pulse duration T. At slow time samples (after each pulse) the range variation is significant and corresponds to a quadratic phase change that occurs during T_i periods. Omitting the propagation losses, the received radar signal $r_{\text{rad}}(t) = s_{\text{rad}}(t - \tau_{\boldsymbol{\theta}}(t))$ is the transmitted LFM signal $s(t)$ after a time delay transformation of $\tau_{\boldsymbol{\theta}}(t)$ due to Doppler and the time delay associated with the target position.

1.5 Conclusion

This chapter presented both AIS and radar systems embedded into satellites with focus on maritime surveillance application. The AIS and radar systems were described in details. Both AIS and radar signal models are presented. The AIS and radar signal models are necessary to simulate AIS and radar signals. Those will be useful in the next chapters to provide representative synthetic data for the simulations.

Chapter 2

Ship detection using AIS and radar raw data

This chapter has been adapted from the conference paper [VVT+16].

2.1 Introduction (in French)

L'objectif de ce chapitre est d'étudier l'apport potentiel d'une utilisation conjointe des données radar et AIS brutes pour la surveillance maritime. Le chapitre débute par la description d'un modèle mathématique qui relie la position inconnue d'un bateau aux mesures AIS et radar via une fonction

non-linéaire et un bruit de mesure additif blanc gaussien. Plus précisément, on obtient les relations suivantes

$$\begin{aligned} y_{\text{rad}} &= \alpha \boldsymbol{a}(\boldsymbol{\theta}) + \boldsymbol{n}_{\text{rad}} \\ y_{\text{AIS}} &= \beta \boldsymbol{b}(\boldsymbol{\theta}) + \boldsymbol{n}_{\text{AIS}} \end{aligned}$$

où

- $\boldsymbol{\theta}$ est la position inconnue du bateau
- β et α sont des amplitudes complexes également inconnues
- $\boldsymbol{b}(\cdot)$ et $\boldsymbol{a}(\cdot)$ sont les signatures AIS et radar d'un bateau situé à la position $\boldsymbol{\theta}$
- $\boldsymbol{n}_{\text{AIS}}$ et $\boldsymbol{n}_{\text{rad}}$ sont des bruits additifs blancs gaussiens de variances σ^2_{AIS} et σ^2_{rad}.

Afin de détecter la présence potentielle d'un bateau à la position $\boldsymbol{\theta}$, le chapitre introduit un problème de détection qui consiste à détecter si les amplitudes α et β sont nulles ou pas

$$\begin{cases} H_0 : \alpha = \beta = 0, (\text{absence of ship}) \\ H_1 : \alpha \neq 0, \beta \neq 0, (\text{presence of ship}). \end{cases}$$

Le problème est alors abordé de manière assez classique en étudiant le test du rapport des vraisemblances (test classiquement appelé GLRT, pour « generalized likelihood ratio test »). Ce test nécessite d'estimer les paramètres inconnus des lois des observations sous chaque hypothèse à l'aide de la méthode du maximum de vraisemblance. Ces estimateurs sont ensuite remplacés dans la vraisemblance du modèle d'observation sous chaque hypothèse. Après quelques calculs détaillés dans ce chapitre, on obtient la règle de décision suivante, sous l'hypothèse de puissance de bruit connue

$$T_{\text{f}} = \frac{\|\boldsymbol{P_a} y_{\text{rad}}\|^2}{\sigma^2_{\text{rad}}} + \frac{\|\boldsymbol{P_b} y_{\text{AIS}}\|^2}{\sigma^2_{\text{AIS}}} \underset{H_0}{\overset{H_1}{\gtrless}} \eta_f \tag{2.1}$$

où $\boldsymbol{P_a}$ et $\boldsymbol{P_b}$ sont des opérateurs de projection sur les vecteurs $a(\boldsymbol{\theta})$ et $b(\boldsymbol{\theta})$ et η_f est un seuil à déterminer en fonction de la probabilité de fausse alarme désirée. Une approche similaire permet

de déterminer les règles de décision correspondant à la présence du radar seul ou de la présence du système AIS seul.

Dans une seconde partie de ce chapitre, nous étudions la loi de probabilité de la statistique de test T_f sous les deux hypothèses H_0 et H_1, de manière à obtenir les courbes COR (caractéristiques opérationnelles du récepteur) qui sont la mesure communément utilisée pour évaluer les performances d'un test statistique. La loi de T_f est une loi du chi-deux centrée sous l'hypothèse H_0 et décentrée sous l'hypothèse H_1.

Le chapitre se termine par des expériences montrant clairement l'apport d'une fusion des données brutes radar et AIS, à partir de données simulées. Ces simulations sont tout d'abord effectuées pour un bateau de taille fixe, puis pour différentes valeurs du rapport signal sur bruit radar, qui dépend directement de la taille du bateau. Dans chacun des cas d'étude, on peut apprécier le gain en probabilité de détection résultant de l'utilisation conjointe des données radar et AIS.

2.2 Introduction

Here we present a way to integrate two dissimilar sensors, namely an AIS and a SAR sensor, in the scope of using raw data for detecting ships.

The SAR signal is designed to be coherent and also orthogonal (in the limits of the maximum unambiguous distances). The transmitted signal is known to the receiver, that signal process the signal returns for the different Doppler and delays in order to discriminate targets.

In contrast, AIS is mainly conceived for communications. Excluding the synchronization patterns present in the AIS signal, the transmitted sequence is mostly unknown to the receiver. Traditionally, the associated processing for AIS signals is more related to decoding information bits than exploring correlation by matched filtering. Despite of that, AIS signals may still be explored differently. For example, one may explore AIS raw measurements with a signal model where there are unknown parameters (for example the ship location).

An inherent problem of working with AIS signals is that they were designed for local radio communications based on a TDMA structure. As described in the first chapter, the AIS ships use

a self-organizing architecture where ships adapt their own transmissions, preventing conflicts and preserving the structure of communications. Time slot allocation varies under time and geographic position as users may relocate their transmissions due to changes in their own travel dynamics or due to a change in time slot availability. This sequential aspect of received signals, the possible non orthogonality of transmissions, and the existence of more unknown parameters in signal structure (e.g. ship identification, speed, Doppler and delay are some examples) may complicate the use of matched filtering methods compared to direct decoding of the AIS bitstream.

One way to identify the ship positioning is to describe the signal measurements as direct function of a model with unknown parameters. For instance, one may consider ship positioning as unknown parameters that are of interest and use raw sensor measurements associated with a signal model to search for the unknown parameters. That method would provide the best theoretical performance considering that no data is discarded by the sensors signal processing.

A possible way to identify ship positioning is to deal with the problem in an estimation approach. In this method, one may explore the sensors model as function of ship positions and the other nuisance parameters (for example, the Doppler shifts, ship speed, delay, frequency offset). By using some assumptions about the measurement noise, one may search for the desired parameter vector that maximizes a likelihood function. This theoretical method needs to search into a large dimensional space. Despite optimal, this approach may not be reliable unless covering a very small geographic zone and with a limited number of ships to estimate. Despite the considerations to reduce the computation time, it may remain too computational intense to be tractable.

Based on this, an alternative is to use detection. In this case, the large dimensional parameter search may be replaced by a detection test, which we must to decide between the presence of absence of ship for some set of fixed parameters. For instance, we want to answer if there is a ship at the coordinates fo the test position, estimating only the remaining parameter nuisances.

In classic detection, data from a single sensor is used for detecting targets. Other methods with multiple sensors usually fusion data after the detection step.

In this chapter, we propose to integrate data from two dissimilar sensors in an upstream step of the processing. Indeed, the closer to the raw data, the less loss of information due to processing.

This way, one can expect better detection performance and possibly detect smaller targets that would have been discarded by a conventional detector. In a fusion-before-detect scheme, we study a new detector adapted to raw data acquired by both AIS and SAR sensors.

This chapter is organized as follows. First we define a data model for the measured sensor signals and the considered modeling assumptions. In Section 2.5, we present the Generalized Likelihood Ratio Test (GLRT) that will be used to detect the presence of radar and AIS signals, followed by the GLRT of the classical detector that will be used for comparison. In Section 2.6 we determine the distribution of the GLRT and we will provide the measurement of detection performance in terms of receiver operational characteristic curves. To finish, in Section 2.8 we draw our conclusions and discuss some prospective tracks to be explored.

2.3 Raw sensor signals

At the beginning of this section we summarize the raw signals models that are used by the proposed ship detection method.

2.3.1 AIS signal model

Here we consider directly the raw AIS signal acquired by the satellite receiver. This signal is a vector of complex time samples obtained after in-phase and quadrature (I/Q) demodulation before any signal processing step. For a single vessel at a position $\boldsymbol{\theta} = (x, y)^T \in \mathbb{R}^2$, the received sampled AIS signal $\boldsymbol{y}_{\text{AIS}} = (y_{\text{AIS}}(1), \ldots, y_{\text{AIS}}(N_{\text{AIS}}))^T \in \mathbb{C}^{N_{\text{AIS}}}$ (where N_{AIS} is the sample size) is defined as

$$\boldsymbol{y}_{\text{AIS}} = \beta \boldsymbol{b}(\boldsymbol{\theta}) + \boldsymbol{n}_{\text{AIS}} \tag{2.2}$$

where $\boldsymbol{b}(\boldsymbol{\theta}) \in \mathbb{C}^{N_{\text{AIS}}}$ represents the AIS signature for a ship located at position $\boldsymbol{\theta}$, $\beta \in \mathbb{C}$ is the unknown complex signal amplitude and $\boldsymbol{n}_{\text{AIS}} \in \mathbb{C}^{N_{\text{AIS}}}$ is the additive measurement noise. We assume that the noise sequence contains uncorrelated complex white Gaussian samples, i.e.

$$\boldsymbol{n}_{\text{AIS}} \sim \mathbb{C}\mathcal{N}\left(0, \sigma^2_{\text{AIS}} \boldsymbol{I}_{N_{\text{AIS}}}\right)$$

where $\boldsymbol{I}_{N_{\text{AIS}}}$ is the $N_{\text{AIS}} \times N_{\text{AIS}}$ identity matrix and σ^2_{AIS} is the AIS noise power (here considered as known initially).

The AIS message is unknown to the receiver, but contains some bits that can be predicted [HLP15]. Consider that a detector will try do detect a ship in a small region on the earth surface. The AIS message bits relative to latitude and longitude coordinates may be tested by the detector for all the possible combinations that cover the area of interest. The detector will identify the presence of a ship by detecting a signal using the correlation of the known AIS bits.

An AIS demodulator must perceive a good SNR in order to decode all the AIS bits without errors. Conventional AIS demodulation compares the CRC block from the AIS message against the CRC calculated over the received AIS bits. The AIS message is considered valid if there is a CRC match. Otherwise, there are errors and the message is usually discarded. There are more advanced demodulation techniques that are able to decode AIS messages at lower SNRs and in presence of bit errors (such as in [Pré12]). However, our interest is to explore the correlation between the known bits to detect ships with help of AIS raw data.

We consider to have a low SNR environment in which the AIS message may not be correctly demodulated. Still, some bits may still be correct and data may be used by an AIS signal detector. As a consequence, the AIS signal model $\boldsymbol{b}(\boldsymbol{\theta})$ can be constructed using the known signaling bits (here the "training sequence", "start flag" and the "end flag") and the predicted message bits (here "latitude" and "longitude" bits in the AIS message). The remaining unknown bits in the signal model are blanks (zeros) and thus do not impact in the detection performance.

2.3.2 Radar signal model

We directly consider the raw radar signal which is a vector of complex time samples obtained after I/Q demodulation and before any signal processing. As described in the radar signal model in Section 1.4.3, we consider the signal model for a single vessel at position $\boldsymbol{\theta} = (x, y)^T \in \mathbb{R}^2$ where the received sampled radar signal $\boldsymbol{y}_{\text{rad}} = (y_{\text{rad}}(1), \ldots, y_{\text{rad}}(N_{\text{rad}}))^T \in \mathbb{C}^{N_{\text{rad}}}$ is defined as

$$\boldsymbol{y}_{\text{rad}} = \alpha \boldsymbol{a}(\boldsymbol{\theta}) + \boldsymbol{n}_{\text{rad}} \tag{2.3}$$

where $\boldsymbol{a}(\boldsymbol{\theta}) = (r(t_1), ..., r(t_{N_{\text{rad}}}))^T$ (with $t_1, ..., t_{N_{\text{rad}}}$ the sampling times) represents the radar signal modeled at the respective sampling times, the scalar $\alpha \in \mathbb{C}$ is the unknown complex signal amplitude and

$$\boldsymbol{n}_{\text{rad}} \sim \mathbb{C}\mathcal{N}\left(0, \sigma^2_{\text{rad}} \boldsymbol{I}_{N_{\text{rad}}}\right) \tag{2.4}$$

is the additive measurement noise whose samples are uncorrelated complex Gaussian and σ^2_{rad} is the noise power.

2.4 Modeling assumptions

There are some practical limitations when using both AIS and radar signals for detection. For instance, considerations need to be made about the reception of both signals. Also, there are detection scenarios that may not be explored properly by our method. Likewise, there are unknown parameters in both radar and AIS signal models that increases the computational complexity of the detectors. Dealing with all those constraints is important for proper use of the signal detectors that will be presented in the next sections.

In summary, we need some modeling assumptions to be considered in order to simplify our detection scenario. Here we consider the following assumptions :

Assumption 1: At a given time instant t, the AIS and radar signals are synchronous with respect to the ship position $\boldsymbol{\theta}(t) = [x(t), y(t)]^T$, where the time dependence has been outlined here for clarity. As the signals coming from the same ship are usually acquired by the SAR and AIS sensors at distinct time instants $t_{\text{rad}} \neq t_{\text{AIS}}$, they do not generally correspond to the same coordinates. However, we assume here that these coordinates have been corrected in order to obtain $\boldsymbol{\theta}(t_{\text{AIS}}) = \boldsymbol{\theta}(t_{\text{rad}})$. It is worth noting that the equality $\boldsymbol{\theta}_{\text{AIS}} = \boldsymbol{\theta}_{\text{rad}}$ is automatically satisfied when repositioning errors are lower than the radar resolution.

Assumption 2: The proposed model is valid for a single ship per test position. Moreover, we assume to test only a binary hypotheses case: or there is a ship and both Radar and AIS data are present, or there is only noise in both Radar and AIS signals. This leads to a simpler detection

problem with only two hypotheses, ignoring complications such as, e.g., signal conflicts with other ships (AIS collisions), or other hypotheses like the presence of a ship signal at only one of the sensors.

Assumption 3: The AIS signal model $\boldsymbol{b}(\cdot)$ not only depends on $\boldsymbol{\theta}$ but also on other parameters, like the bit-stuffing in the message, Doppler, time delay, difference in the modulation index, among others. Even being possible to deal with bit-stuffing, it can be neglected assuming some detection performance loss [HLP15].

Our assumption facilitates our signal model and provides an upper bound of detection performance. In other words, this assumption corresponds to a best case scenario without any error in bit-stuffing, Doppler, time delay, difference in the modulation index. We assume here that these parameters are known by the receiver in order to obtain a simplified model $\boldsymbol{b}(\boldsymbol{\theta})$.

2.5 GLRT detectors

In this section we introduce the statistical test proposed to detect the presence of signals applied to our context of AIS and radar sensors. The concept of the signal detectors presented in this work is based on a binary hypothesis testing that contrasts the null hypothesis against an alternative one. More precisely, we are interested in generating a test that evaluates the raw sensor data and infer about the presence (or absence) of signals in a noisy environment. We present two likelihood ratio test that will be used to decide between the hypotheses. In fact, as the probability density functions depend on a set of unknown parameters that differ under each hypothesis, the generalized likelihood ratio test (GLRT) is considered for this task replacing the unknown by their estimates in order to obtain the desired detectors.

2.5.1 Detector for AIS and radar raw data

In order to detect the presence or absence of a ship using AIS and radar data, we propose to study the following binary hypothesis testing problem

$$\begin{cases} H_0 : \alpha = \beta = 0, (\text{absence of ship}) \\ H_1 : \alpha \neq 0, \beta \neq 0, (\text{presence of ship}). \end{cases} \tag{2.5}$$

Note that hypothesis H_0 corresponds to the absence of ship in both AIS and radar measurements whereas hypothesis H_1 corresponds to a situation for which the ship signature is present in both AIS and radar measurements. The hybrid case for which the ship is present in only one of the two signatures will be discussed in the next section. Since the two amplitudes α and β are unknown, it is standard to consider the GLRT to solve the detection problem (2.5). The GLRT for (2.5) is based on the following test statistics

$$\frac{p(\boldsymbol{y}_{\text{AIS}}, \boldsymbol{y}_{\text{rad}}|\hat{\alpha}, \hat{\beta}, \boldsymbol{\theta}, H_1)}{p(\boldsymbol{y}_{\text{AIS}}, \boldsymbol{y}_{\text{rad}}|\alpha = 0, \beta = 0, \boldsymbol{\theta}, H_0)} \tag{2.6}$$

where parameters $\hat{\alpha}$ and $\hat{\beta}$ are the maximum likelihood estimators of the signal amplitudes under hypothesis H_1 and $p(\boldsymbol{y}_{\text{AIS}}, \boldsymbol{y}_{\text{rad}}|\alpha, \beta, H_i)$ is the probability density function of the measurement vectors $(\boldsymbol{y}_{\text{AIS}}, \boldsymbol{y}_{\text{rad}})$ at the position $\boldsymbol{\theta}$ under the hypothesis H_i.

Under the signal models (2.2) and (2.3) we have the probability density functions

$$p(\boldsymbol{y}_{\text{rad}}; \alpha, \sigma^2_{\text{rad}}, \boldsymbol{\theta}) = \left(\pi\sigma^2_{\text{rad}}\right)^{-N_{\text{rad}}} \exp\left\{-\frac{\|\boldsymbol{y}_{\text{rad}} - \boldsymbol{a}(\boldsymbol{\theta})\alpha\|^2}{\sigma^2_{\text{rad}}}\right\} \tag{2.7}$$

$$p(\boldsymbol{y}_{\text{AIS}}; \beta, \sigma^2_{\text{AIS}}, \boldsymbol{\theta}) = \left(\pi\sigma^2_{\text{AIS}}\right)^{-N_{\text{AIS}}} \exp\left\{-\frac{\|\boldsymbol{y}_{\text{AIS}} - \boldsymbol{b}(\boldsymbol{\theta})\beta\|^2}{\sigma^2_{\text{AIS}}}\right\}. \tag{2.8}$$

Consider that we are going to solve a detection problem for a single position $\boldsymbol{\theta} = (x_0, y_0)$. Since $\boldsymbol{\theta}$ is fixed, for simplicity of notation we write $\boldsymbol{a}$ and $\boldsymbol{b}$ instead of $\boldsymbol{a}(\boldsymbol{\theta})$ and $\boldsymbol{b}(\boldsymbol{\theta})$, respectively. Being the additive noises $\boldsymbol{n}_{\text{rad}}$ and $\boldsymbol{n}_{\text{AIS}}$ independent random variables with σ^2_{rad} and σ^2_{AIS} known variances, we have the joint probability density function

$$\begin{aligned} p(\boldsymbol{y}_{\text{rad}}, \boldsymbol{y}_{\text{AIS}}; \alpha, \beta) &= p(\boldsymbol{y}_{\text{rad}}; \alpha, \sigma^2_{\text{rad}}) \times p(\boldsymbol{y}_{\text{AIS}}; \beta, \sigma^2_{\text{AIS}}) \\ &= \left(\pi\sigma^2_{\text{rad}}\right)^{-N_{\text{rad}}} \left(\pi\sigma^2_{\text{AIS}}\right)^{-N_{\text{AIS}}} \exp\left\{-\frac{\|\boldsymbol{y}_{\text{rad}} - \boldsymbol{a}\alpha\|^2}{\sigma^2_{\text{rad}}} - \frac{\|\boldsymbol{y}_{\text{AIS}} - \boldsymbol{b}\beta\|^2}{\sigma^2_{\text{AIS}}}\right\}. \end{aligned} \tag{2.9}$$

Under hypothesis H_1 the unknown signal amplitudes α and β may be replaced by their maximum likelihood estimates (MLE) $\hat{\alpha}$ and $\hat{\beta}$. It follows immediately that

$$\hat{\alpha} = \frac{\boldsymbol{a}^H}{\|\boldsymbol{a}\|^2}\boldsymbol{y}_{\text{rad}} \tag{2.10}$$

$$\hat{\beta} = \frac{\boldsymbol{b}^H}{\|\boldsymbol{b}\|^2}\boldsymbol{y}_{\text{AIS}}. \tag{2.11}$$

Reporting (2.10) and (2.11) into (2.9) and also naming $k_0 = (\pi\sigma^2_{\text{rad}})^{-N_{\text{rad}}}(\pi\sigma^2_{\text{AIS}})^{-N_{\text{AIS}}}$, we obtain

$$p(\boldsymbol{y}_{\text{rad}}, \boldsymbol{y}_{\text{AIS}}|\hat{\alpha}, \hat{\beta}, H_1) = k_0 \exp\left\{-\frac{\|(\boldsymbol{I} - \boldsymbol{P_a})\boldsymbol{y}_{\text{rad}}\|^2}{\sigma^2_{\text{rad}}} - \frac{\|(\boldsymbol{I} - \boldsymbol{P_b})\boldsymbol{y}_{\text{AIS}}\|^2}{\sigma^2_{\text{AIS}}}\right\} \tag{2.12}$$

where $\boldsymbol{P_a} = \boldsymbol{a}\boldsymbol{a}^H/\|\boldsymbol{a}\|^2$ and $\boldsymbol{P_b} = \boldsymbol{b}\boldsymbol{b}^H/\|\boldsymbol{b}\|^2$ are, respectively, the projection operators onto the subspace spanned by their respective vectors $\boldsymbol{a}$ and $\boldsymbol{b}$. Under the null hypothesis H_0, the signal amplitudes are $\alpha = \beta = 0$ which means that $\boldsymbol{y}_{\text{AIS}}$ and $\boldsymbol{y}_{\text{rad}}$ measurements are composed only by the noises. It is immediate that

$$p(\boldsymbol{y}_{\text{rad}}, \boldsymbol{y}_{\text{AIS}}|\alpha = 0, \beta = 0, H_0) = k_0 \exp\left\{-\frac{\|\boldsymbol{y}_{\text{rad}}\|^2}{\sigma^2_{\text{rad}}} - \frac{\|\boldsymbol{y}_{\text{AIS}}\|^2}{\sigma^2_{\text{AIS}}}\right\}. \tag{2.13}$$

Applying (2.12) and (2.13) to the test statistics in (2.6) then the generalized likelihood ratio (GLR) is given by

$$\frac{p(\boldsymbol{y}_{\text{rad}}, \boldsymbol{y}_{\text{AIS}}|\hat{\alpha}, \hat{\beta}, H_1)}{p(\boldsymbol{y}_{\text{rad}}, \boldsymbol{y}_{\text{AIS}}|\alpha = 0, \beta = 0, H_0)} = \frac{\exp\left\{-\frac{\|(\boldsymbol{I}-\boldsymbol{P_a})\boldsymbol{y}_{\text{rad}}\|^2}{\sigma^2_{\text{rad}}} - \frac{\|(\boldsymbol{I}-\boldsymbol{P_b})\boldsymbol{y}_{\text{AIS}}\|^2}{\sigma^2_{\text{AIS}}}\right\}}{\exp\left\{-\frac{\|\boldsymbol{y}_{\text{rad}}\|^2}{\sigma^2_{\text{rad}}} - \frac{\|\boldsymbol{y}_{\text{AIS}}\|^2}{\sigma^2_{\text{AIS}}}\right\}}.$$

After some trivial manipulation and taking the logarithm, the GLRT then amounts to comparing

$$T_{\text{f}} = \frac{\|\boldsymbol{P_a}\boldsymbol{y}_{\text{rad}}\|^2}{\sigma^2_{\text{rad}}} + \frac{\|\boldsymbol{P_b}\boldsymbol{y}_{\text{AIS}}\|^2}{\sigma^2_{\text{AIS}}} \underset{H_0}{\overset{H_1}{\gtrless}} \eta_f \tag{2.14}$$

which η_f is an appropriate detection threshold [VBR08] to be chosen accordingly. It is interesting to note that the detector (2.14) is a weighted sum of two independent test statistics that are associated, respectively, with the radar and the AIS measurements. This weighted sum can be viewed as the sum of the estimated signal-to-noise ratios for the AIS and radar test statistics. Of course, the probability of detection P_d and the probability of false alarm P_{fa} of the test (2.14) are directly related to the value of the decision threshold η_f.

2.5.2 Detector for radar raw data

When a single source of information is available, the GLRT detector (2.14) reduces to the matched subspace detector (MSD) [Sch91]. For instance, in the case of radar data only, the test statistics reduces to

$$T_{\text{rad}} = \frac{\|\boldsymbol{P_a}\boldsymbol{y}_{\text{rad}}\|^2}{\sigma^2_{\text{rad}}} \underset{H_0}{\overset{H_1}{\gtrless}} \eta_{\text{rad}} \tag{2.15}$$

where η_{rad} is a detection threshold to be adjusted as a function of the desired detection performance in term of P_d or P_{fa}.

A similar result can be obtained for the GLRT for AIS data only. The proof is immediate.

2.5.3 Detector for AIS and radar raw data (unknown noise power case)

Here we present a different formulation of the detector considering the case that noise power is unknown. In that case, σ^2_{AIS} and σ^2_{rad} parameters need also to be estimated. In the same procedure for α and β, we use the MLE for both noise parameters plugged directly into the GLRT in order to obtain a constant false alarme rate (CFAR) detector.

From the hypothesis test in (2.5), we have the test statistic presented in (2.6). Now consider the extra nuisances as the signal noise power for both AIS and radar. Then the test statistics now becomes

$$\frac{p(\boldsymbol{y}_{\text{AIS}}, \boldsymbol{y}_{\text{rad}}|\hat{\alpha}, \hat{\beta}, \hat{\sigma}^2_{\text{AIS}}, \hat{\sigma}^2_{\text{rad}}\boldsymbol{\theta}, H_1)}{p(\boldsymbol{y}_{\text{AIS}}, \boldsymbol{y}_{\text{rad}}|\alpha = 0, \beta = 0, \hat{\sigma}^2_{\text{AIS}}, \hat{\sigma}^2_{\text{rad}}, \boldsymbol{\theta}, H_0)}, \tag{2.16}$$

where parameters $\hat{\sigma}^2_{\text{AIS}}$ and $\hat{\sigma}^2_{\text{rad}}$ are the maximum likelihood estimators of the signal noise powers under both hypothesis.

The likelihood for AIS and radar signals are presented in 2.8 and 2.7. Similarly, (2.9) represents the same joint probability density function of using both AIS and radar sensors. It is immediate to obtain both $\hat{\sigma}^2_{\text{AIS}}$ and $\hat{\sigma}^2_{\text{rad}}$. Using the partial derivatives of both likelihoods to represent the extreme value of the functions with respect to σ^2_{AIS} and σ^2_{rad}, we obtain

$$\begin{aligned} \frac{\partial \ln L}{\partial \sigma^2_{\text{AIS}}} &= \frac{\partial}{\partial \sigma^2_{\text{AIS}}}\left(-N_{\text{AIS}}\ln(\pi) - N_{\text{AIS}}\ln(\sigma^2_{\text{AIS}}) - \frac{\boldsymbol{z}^H\boldsymbol{z}}{\sigma^2_{\text{AIS}}}\right) = 0 \\ \hat{\sigma}^2_{\text{AIS}} &= \boldsymbol{z}^H\boldsymbol{z}/N_{\text{AIS}}, \end{aligned} \tag{2.17}$$

where $\boldsymbol{z}$ is the term $\boldsymbol{y}_{\text{AIS}} - \boldsymbol{b}\beta$. It is immediate that

$$\hat{\sigma}^2_{\text{rad}} = \boldsymbol{x}^H\boldsymbol{x}/N_{\text{rad}} \tag{2.18}$$

where $\boldsymbol{x} = \boldsymbol{y}_{\text{rad}} - \boldsymbol{a}\alpha$. Finally, the likelihood equation considering the MLE of the radar and AIS noise powers is

$$L = k_1(\boldsymbol{z}^H\boldsymbol{z})^{-N_{\text{AIS}}}(\boldsymbol{x}^H\boldsymbol{x})^{-N_{\text{rad}}} \tag{2.19}$$

where $k_1 = (\pi e/N_{\text{AIS}})^{-N_{\text{AIS}}} (\pi e/N_{\text{rad}})^{-N_{\text{rad}}}$ is a constant.

Under hypothesis H_1, the unknown signal amplitudes α and β may be replaced by their maximum likelihood estimates $\hat{\alpha}$ and $\hat{\beta}$. It is immediate that $\hat{\alpha}$ and $\hat{\beta}$ are the same found in (2.10) and (2.11). Replacing the unknown variables by their MLE we obtain

$$L = \begin{cases} k_1 \left(\boldsymbol{y}_{\text{rad}}^H \boldsymbol{P}_{\boldsymbol{a}}^{\perp} \boldsymbol{y}_{\text{rad}} \right)^{-N_{\text{rad}}} \left(\boldsymbol{y}_{\text{AIS}}^H \boldsymbol{P}_{\boldsymbol{b}}^{\perp} \boldsymbol{y}_{\text{AIS}} \right)^{-N_{\text{AIS}}} & \text{under } H_1 \\ k_1 \left(\boldsymbol{y}_{\text{rad}}^H \boldsymbol{y}_{\text{rad}} \right)^{-N_{\text{rad}}} \left(\boldsymbol{y}_{\text{AIS}}^H \boldsymbol{y}_{\text{AIS}} \right)^{-N_{\text{AIS}}} & \text{under } H_0. \end{cases} \tag{2.20}$$

The GLRT considering noise power unknown for the detector of both radar and AIS signals is

$$T_{\text{uf}} = \left(\frac{\|\boldsymbol{y}_{\text{rad}}\|^2}{\left\| \boldsymbol{P}_{\boldsymbol{a}}^{\perp} \boldsymbol{y}_{\text{rad}} \right\|^2} \right)^{N_{\text{rad}}} \left(\frac{\|\boldsymbol{y}_{\text{AIS}}\|^2}{\left\| \boldsymbol{P}_{\boldsymbol{b}}^{\perp} \boldsymbol{y}_{\text{AIS}} \right\|^2} \right)^{N_{\text{AIS}}}, \tag{2.21}$$

where T_{uf} represents the GLRT of a detector considering the case of unknown noise power that jointly uses both AIS and radar raw signals. This detector is the product of two constant false alarm rate (CFAR) matched subspace detectors (see [Sch91]) with different power exponents. It is direct that the probability law of T_{uf} is a product of two χ^2 distributions with different power exponents.

Next we proceed with performance analysis of the detectors, where we will compare the radar detector with the detector T_{f}, the case considering noise power known. The detector T_{uf} that considers noise power unknown is presented here for reference only and will not be evaluated.

2.6 Performance analysis

The detectors derived in the last sections will be compared thanks to their receiver operational characteristics (ROCs), which requires the distribution of the test statistics under both hypotheses. In the sequel, we present the distribution of the test statistics. The closed form equations of distributions are used to produce the ROC curves that will evaluate the respective theoretical performance of both detectors.

The notation $\chi_n^2(\lambda)$ indicates a chi-squared distribution with n degrees of freedom and non-centrality parameter λ. We use the notation $W \sim \rho\chi_n^2(\lambda)$ for a random variable W such that W/ρ is distributed as a chi-squared distribution $\chi_n^2(\lambda)$. Of course, the distribution $\chi_n^2(\lambda)$ reduces to the central chi-squared distribution for $\lambda = 0$.

2.6.1 Distribution of the test statistic $T_{\mathbf{rad}}$ (radar data)

The test statistic T_{rad} in (2.15) is a quadratic form from a multivariate complex normal distribution. From the noise distribution (2.4) it is clear that

$$\boldsymbol{P_a}\boldsymbol{y}_{\text{rad}} \sim \mathbb{C}\mathcal{N}\left(\boldsymbol{a}\alpha, \sigma^2_{\text{rad}}\boldsymbol{P_a}\right). \tag{2.22}$$

is correlated with $\boldsymbol{P_a}$ as correlation matrix. The correlation matrix is symmetric and nonnegative definite. Therefore, there exists an orthogonal transformation matrix $\boldsymbol{Q}$ such that $\boldsymbol{Q}^H\boldsymbol{P_a}\boldsymbol{Q} = \boldsymbol{I}_k$, where $k = \text{rank}(\boldsymbol{P_a})$. It follows that the transformed vector

$$\boldsymbol{Q}^H\boldsymbol{P_a}\boldsymbol{y}_{\text{rad}} \sim \mathbb{C}\mathcal{N}\left(\boldsymbol{Q}^H\boldsymbol{a}\alpha, \sigma^2_{\text{rad}}\boldsymbol{I}_k\right) \tag{2.23}$$

is uncorrelated while preserving the same quadratic form

$$\boldsymbol{y}^H_{\text{rad}}\boldsymbol{P_a}\boldsymbol{Q}\boldsymbol{Q}^H\boldsymbol{P_a}\boldsymbol{y}_{\text{rad}} = \boldsymbol{y}^H_{\text{rad}}\boldsymbol{P_a}\boldsymbol{y}_{\text{rad}} = \|\boldsymbol{P_a}\boldsymbol{y}_{\text{rad}}\|^2.$$

The quadratic function from multivariate normal random variables has a chi-squared distribution [Sch91, p.63]. Since it is usual dealing with the real χ^2 distribution, we define $\mathcal{T}\{\cdot\}$ the real isomorphism that allows the one-to-one mapping correspondence from the complex vector space $\mathbb{C}^p$ to the real vector space $\mathbb{R}^{2p}$ (see [DFKE95] for more details). A random vector $\boldsymbol{w} \in \mathbb{C}^p$ may be represented as

$$\mathcal{T}\{\boldsymbol{w}\} = \begin{pmatrix} \text{Re}(\boldsymbol{w}) \\ \text{Im}(\boldsymbol{w}) \end{pmatrix}$$

where $\mathcal{T}\{\boldsymbol{w}\} \in \mathbb{R}^{2p}$. Similarly, a matrix $\boldsymbol{C} \in \mathbb{C}^{p\times p}$ the isomorphism transform produces

$$\mathcal{T}\{\boldsymbol{C}\} = \begin{pmatrix} \text{Re}(\boldsymbol{C}) & -\text{Im}(\boldsymbol{C}) \\ \text{Im}(\boldsymbol{C}) & \text{Re}(\boldsymbol{C}) \end{pmatrix}$$

which is a real partitioned matrix with $\mathcal{T}\{\boldsymbol{C}\} \in \mathbb{R}^{2p\times 2p}$. From those definitions, it is straightforward that the k-dimensional complex random vector in (2.23) may be written as the $2k$-dimensional real random vector

$$\mathcal{T}\left\{\boldsymbol{Q}^H\boldsymbol{P_a}\boldsymbol{y}_{\text{rad}}\right\} \sim \mathcal{N}(\mathcal{T}\left\{\boldsymbol{Q^H a}\right\}\alpha, \frac{1}{2}\sigma^2_{\text{rad}}\boldsymbol{I}_{2k}).$$

For convenience, we let $\boldsymbol{w} = \boldsymbol{Q}^H \boldsymbol{P_a} \boldsymbol{y}_{\text{rad}}/\sigma_{\text{rad}}$ so that

$$\mathcal{T}\left\{\sqrt{2}\boldsymbol{w}\right\} \sim \mathcal{N}(\sqrt{2}\mathcal{T}\left\{\boldsymbol{Q}^H\boldsymbol{a}\right\}\alpha, \boldsymbol{I}_{2k})$$

has the quadratic form

$$2\frac{\boldsymbol{w}^H\boldsymbol{w}}{\sigma^2_{\text{rad}}} = 2T_{\text{rad}} \sim \chi^2_{2k}(\lambda_{\text{rad}})$$

that is distributed as a non central χ^2 distribution with non-centrality parameter

$$\lambda_{\text{rad}} = \|\sqrt{2}\alpha\boldsymbol{Q}^H\boldsymbol{a}/\sigma_{\text{rad}}\|^2 = 2\alpha^2\|\boldsymbol{a}\|^2/\sigma^2_{\text{rad}} \tag{2.24}$$

with $2k$ degrees of freedom in which $k = \text{rank}(\boldsymbol{Q^H P_a}) = 1$. The detector distribution under both hypotheses only differs on the non-centrality parameter, as for the null hypothesis $\alpha = 0$ and consequently $\lambda = 0$. We conclude that the distribution of the MSD in corresponding to radar only measurements in the case of a known noise power is

$$T_{\text{rad}} \sim \begin{cases} \frac{1}{2}\chi^2_2(0) & \text{under } H_0 \\ \frac{1}{2}\chi^2_2(\lambda_{\text{rad}}) & \text{under } H_1. \end{cases} \tag{2.25}$$

A similar result can be obtained for the distribution of the test statistics for AIS data only.

2.6.2 Distribution of the test statistic T_{f} (radar and AIS data)

The distribution of T_{f} test statistics in (2.14) may be obtained by evaluating the signal model random variables in (2.2) and (2.3). Since T_{f} is the sum of two quadratic forms originated from independent multivariate normal distributions, it is easily seen from Section 2.6.1 that

$$\frac{\|\boldsymbol{P_a}\boldsymbol{y}_{\text{rad}}\|^2}{\sigma^2_{\text{rad}}} \sim \frac{1}{2}\chi^2_{2k}(\lambda_{\text{rad}})$$
$$\frac{\|\boldsymbol{P_b}\boldsymbol{y}_{\text{AIS}}\|^2}{\sigma^2_{\text{AIS}}} \sim \frac{1}{2}\chi^2_{2l}(\lambda_{\text{AIS}})$$

are two independent non central χ^2 random variables with respectively $\lambda_{\text{rad}} = 2\alpha^2\|\boldsymbol{a}(\boldsymbol{\theta})\|^2/\sigma^2_{\text{rad}}$ and $\lambda_{\text{AIS}} = 2\beta^2\|\boldsymbol{b}(\boldsymbol{\theta})\|^2/\sigma^2_{\text{AIS}}$ non-centrality parameters. It is known that the non central χ^2 distribution

satisfies the reproductive property with respect to the number of degrees of freedom and the non-centrality parameter [Rao02, p.182]. Thus, we have that

$$T_{\mathrm{f}} = \frac{\|\boldsymbol{P_a}\boldsymbol{y}_{\mathrm{rad}}\|^2}{\sigma^2_{\mathrm{rad}}} + \frac{\|\boldsymbol{P_b}\boldsymbol{y}_{\mathrm{AIS}}\|^2}{\sigma^2_{\mathrm{AIS}}} \sim \frac{1}{2}\chi^2_{2k+2l}(\lambda_{\mathrm{rad}} + \lambda_{\mathrm{AIS}})$$

is also χ^2 distributed with $2k + 2l$ degrees of freedom and $\lambda_{\mathrm{rad}} + \lambda_{\mathrm{AIS}}$ non-centrality parameter. Given that $k = \mathrm{rank}(\boldsymbol{P_a}) = 1$ and $l = \mathrm{rank}(\boldsymbol{P_b}) = 1$ and considering that under the null hypothesis $\lambda_{\mathrm{rad}} = \lambda_{\mathrm{AIS}} = 0$, we conclude that the test statistic T_{f} of the joint AIS and radar detector that uses raw sensor data has the distribution

$$T_{\mathrm{f}} \sim \begin{cases} \frac{1}{2}\chi^2_4(0) & \text{under } H_0 \\ \frac{1}{2}\chi^2_4(\lambda_{\mathrm{rad}} + \lambda_{\mathrm{AIS}}) & \text{under } H_1. \end{cases} \tag{2.26}$$

2.6.3 Receiver operating characteristics

The probability distributions derived in the previous section can be used to determine the ROCs for both detectors T_{rad} and T_{f}, and thus to evaluate the potential performance gain due to the joint use of AIS and radar data. Let

$$Q_{\chi^2}(y; n, \lambda) = \int_{\boldsymbol{y}}^{\infty} p_{\chi^2(n,\lambda)}(x)dx$$

denote the complementary cumulative distribution function (CCDF) of a non central χ^2 random variable y with n degrees of freedom and non-centrality parameter λ, and consider $Q^{-1}_{\chi^2}(p; n, \lambda)$ its inverse [VBR08]. The P_d and the P_{fa} of both detectors can be derived as follows

Radar only

$$P_{fa}(T_{\mathrm{rad}}) = Q_{\chi^2}(2\eta_{\mathrm{rad}}; 2, 0)$$
$$P_d(T_{\mathrm{rad}}) = Q_{\chi^2}(2\eta_{\mathrm{rad}}; 2, \lambda_{\mathrm{rad}})$$

AIS and radar

$$P_{fa}(T_{\mathrm{f}}) = Q_{\chi^2}(2\eta_f; 4, 0)$$
$$P_d(T_{\mathrm{f}}) = Q_{\chi^2}(2\eta_f; 4, \lambda_{\mathrm{AIS}} + \lambda_{\mathrm{rad}}).$$

Straightforward use of the CCDF and its inverse lead to the following ROC equations

Radar only

$$P_d(T_{\text{rad}}) = Q_{\chi^2}(Q_{\chi^2}^{-1}(P_{fa}(T_{\text{rad}}); 2, 0); 2, \lambda_{\text{rad}}) \tag{2.27}$$

AIS and radar

$$P_d(T_{\text{f}}) = Q_{\chi^2}(Q_{\chi^2}^{-1}(P_{fa}(T_{\text{f}}); 4, 0); 4, \lambda_{\text{AIS}} + \lambda_{\text{rad}}) \tag{2.28}$$

where (3.26) and (3.25) represent the theoretical performance in terms of P_d versus P_{fa}. The expressions also indicate that the detection performance is directly related to the non-centrality parameters of the distributions λ_{rad} and $\lambda_{\text{AIS}} + \lambda_{\text{rad}}$. Observe that

$$\begin{aligned} 2\alpha\|\boldsymbol{a}\|^2/\sigma^2_{\text{rad}} &= 2\alpha \sum_{i=1}^{N_{\text{rad}}} \|a_i\|^2/\sigma^2_{\text{rad}} = 2N_{\text{rad}}\,\text{SNR}_{\text{rad}} \\ 2\beta\|\boldsymbol{b}\|^2/\sigma^2_{\text{AIS}} &= 2\beta \sum_{i=1}^{N_{\text{AIS}}} \|b_i\|^2/\sigma^2_{\text{AIS}} = 2N_{\text{AIS}}\,\text{SNR}_{\text{AIS}} \end{aligned}$$

where N_{rad} is the number of radar integrated samples and SNR_{rad} the input signal-to-noise ratio of the radar samples (respectively N_{AIS} and SNR_{AIS} for the AIS samples). Denoting as SNRo the output signal-to-noise ratio [Sch91], we can express both as function of the non-centrality parameters as

$$\lambda_{\text{rad}} = 2N_{\text{rad}}\,\text{SNR}_{\text{rad}} = 2\,\text{SNRo}_{\text{rad}}$$

and

$$\lambda_{\text{AIS}} = 2N_{\text{AIS}}\,\text{SNR}_{\text{AIS}} = 2\,\text{SNRo}_{\text{AIS}}\,.$$

The different detectors are then comparable for a given target SNR expressing their performance in terms of P_d as a function of P_{fa} via the ROC curves.

2.7 Simulation results

To analyze the performance of the two detectors defined before, we consider a simulation scenario (in agreement with the assumptions in 2.4) with AIS and SAR signals corresponding to a single ship.

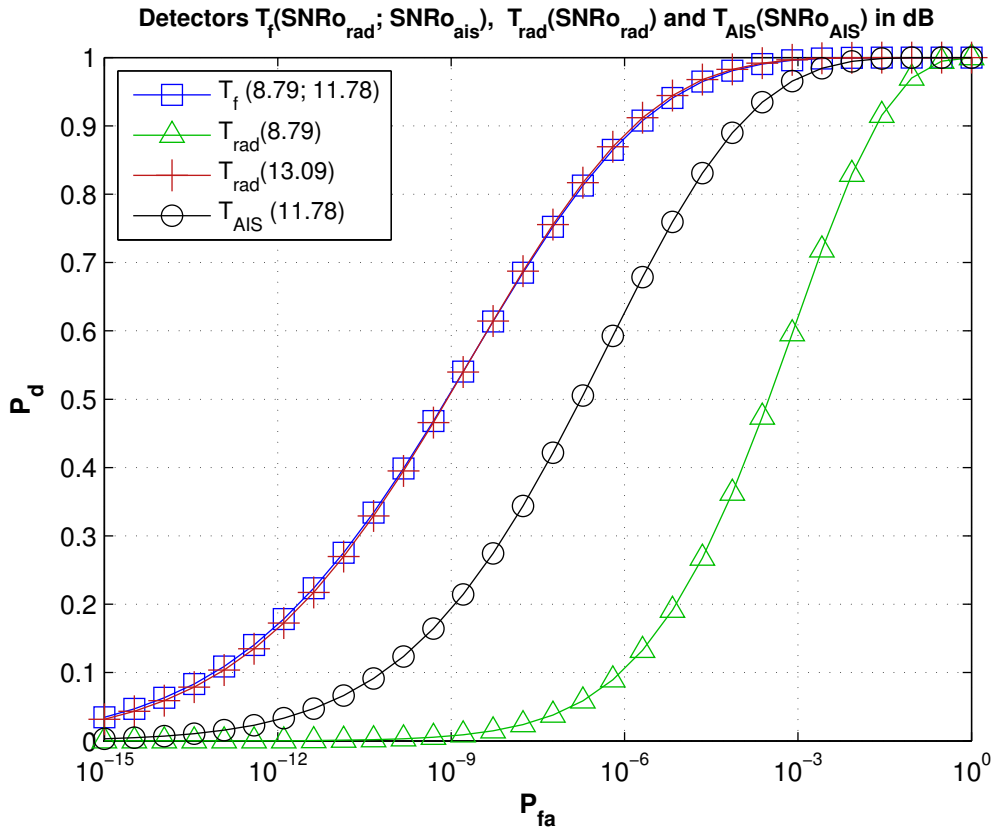

Figure 2.1: ROCs of $T_{\rm f}$, $T_{\rm AIS}$ and $T_{\rm rad}$ for a small ship ($\text{SNRo}_{\rm rad} = 8.79$ dB). The $T_{\rm rad}$ ROC for a bigger ship ($\text{SNRo}_{\rm rad} = 13.09$ dB) is also presented for comparison.

The SAR system is assumed to operate with 200 pulses of $2\mu s$ and 30MHz bandwidth, yielding a total of $N_{\rm rad} = 12000$ samples. For the AIS system, the known signaling bits and the predicted message bits lead to $N_{\rm AIS} = 95$. The ROCs are determined using equations (3.25) and (3.26).

The first set of experiments is presented in Fig. 2.1 for a small ship with a radar SNR of -33 dB (i.e., $\text{SNRo}_{\rm rad} = 8.79$ dB) and with an AIS SNR of -8 dB (i.e., $\text{SNRo}_{\rm AIS} = 11.78$ dB). Note that we used a logarithmic scale for the X axis and a linear scale for the Y axis. The gain obtained by using both AIS and radar data (blue line with squares) can be clearly observed when compared to the detector that uses radar measurements only $T_{\rm rad}$ (green line with triangles). For reference, a detector using AIS measurements only ($T_{\rm AIS}$) is presented (black line with circles) that is also outperformed

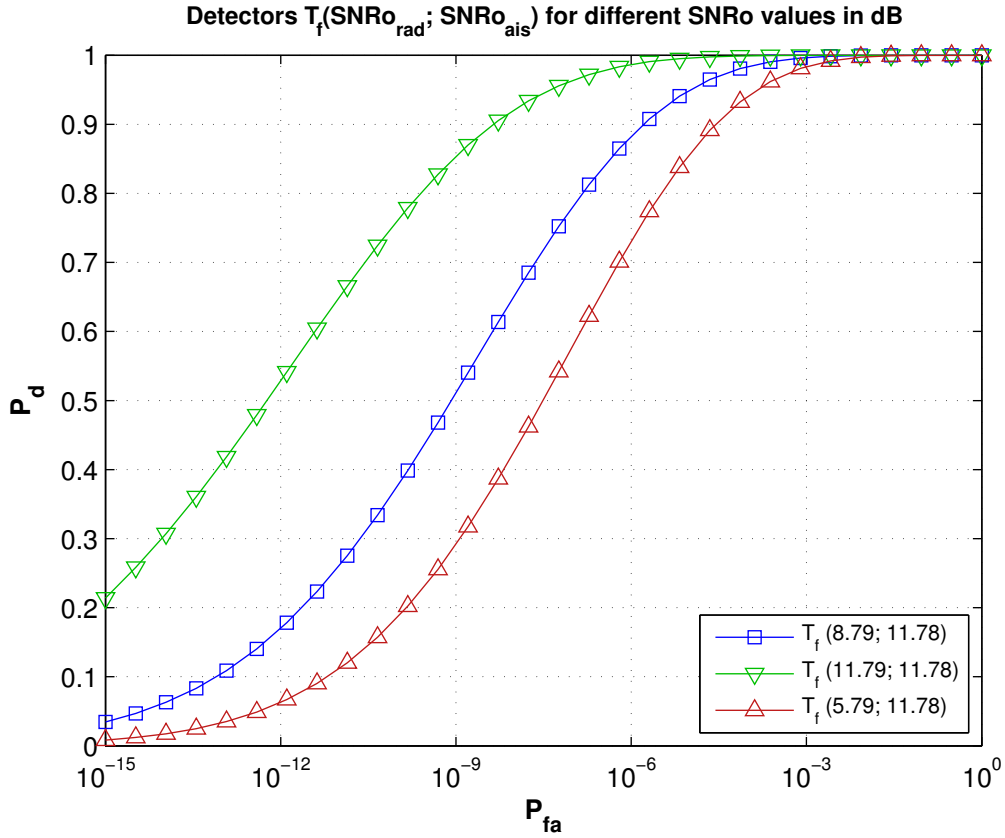

Figure 2.2: ROCs of T_{f} for different ship sizes, i.e., different radar SNRs ($\mathrm{SNRo}_{\mathrm{AIS}} = 11.78$ dB).

by the joint AIS/radar detector T_{f}. Note that for a detection probability $P_d = 0.9$ the probability of false alarm of T_{f} is close to $P_{fa} = 10^{-6}$, whereas for T_{rad}, we have P_{fa} close to 10^{-2}. In this example, the detector based on joint AIS/radar data provides a significative gain that allows us to detect targets 4.3 dB smaller while keeping the same performance in terms of P_d versus P_{fa} (blue line with squares and red line with crosses). Note that the performance of T_{f} is only compared to T_{rad} because the radar is more reliable than the AIS.

The second set of experiments compares ROCs associated with the joint AIS/radar detector for a fixed AIS SNR ($\mathrm{SNRo}_{\mathrm{AIS}} = 11.78$ dB) and different radar SNRs (i.e., different ship sizes). Fig. 2.2 shows that the detection performance is an increasing function of the radar SNR, as expected. This kind of comparison can be made for different SNRs, we may also consider a different number of

correlation bits for the AIS signal.

Simulation using synthetic AIS and radar data

It is natural to relate the performance ROC curves obtained from the theoretical distributions of the test statistics with ROC curves from synthetic data generated from the radar and AIS signal models. Detection performance may be evaluated using Monte Carlo trials in order to estimate the P_d versus P_{fa} using experimental ROC curves.

We consider the same hypotheses used for the theoretical models in the Section 2.4. We use synthetic data for both AIS and Radar with the GLRT detectors derived in Section 2.5. Likewise, we also simulate that the AIS and radar signals are originated from a fixed position $\boldsymbol{\theta}$ which we want to test.

Observing the figure 2.3 we evaluate the T_{f} model using synthetic data. One may see that the theoretical and synthetic curves are very close for different values of radar SNRo. Notice that the curves were plotted with lower SNR compared with figure 2.2. This was intentional as lower is the probability of false alarm samples are needed to trace the curves using synthetic data. Our conclusion is that the data samples reproduce the same detection probability as the theoretic curves, which validates our statistical model in a practical simulation using radar and AIS signal samples.

2.8 Conclusion

This chapter presented a ship detector combining AIS and radar data for maritime surveillance. This problem was formulated as a binary hypothesis test that was handled using the principle of the generalized likelihood ratio detector. We derived the distribution of the resulting test statistics under both hypotheses, allowing the receiver operational characteristics to be computed in closed form. A comparison between the ROCs associated with the joint AIS/radar detector, the AIS detector and the radar detector allowed the performance gain obtained when using both sensors to be appreciated. Both theoretical and empirical curves were obtained and compared, allowing to validate the statistical model used.

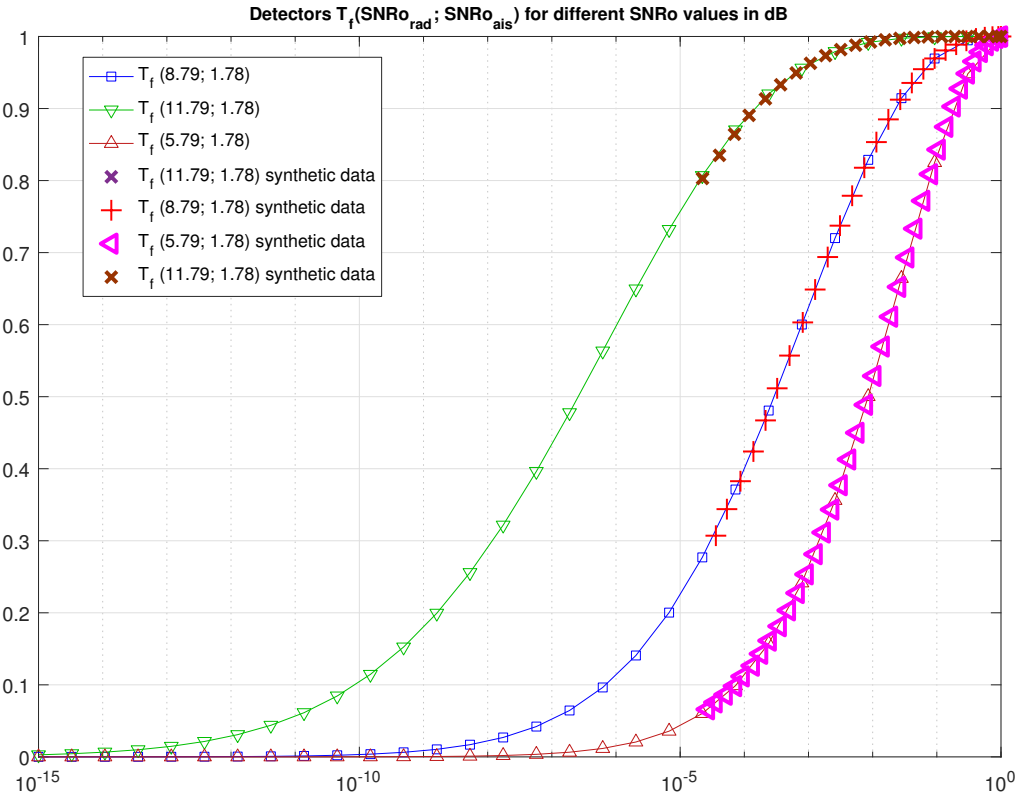

Figure 2.3: ROCs of T_{f} for different ship sizes, i.e., different radar SNRs ($\mathrm{SNRo}_{\mathrm{AIS}} = 1.78$ dB).

This study was based on some important simplifying assumptions that allowed the evaluation of the detection performance of a detector which uses both AIS and radar raw data. Despite the promising results, one has to deal with the computational complexity of the method which is complicated for real time implementation.

In the next chapters another development is devoted to the fusion of radar raw signal with AIS processed data (the ship positioning information decoded from the AIS signals), where we direct to a realizable sub optimal solution, exploring data in different manner with reduced computational complexity.

Chapter 3

Improve radar detection using AIS processed data

This chapter has been adapted from the conference paper [VVT+17].

3.1 Introduction (in French)

Dans le chapitre précédent, nous avons choisi d'exploiter les signaux AIS et Radar bruts, dans le but de les fusionner en conservant un maximum d'information. Nous avons ainsi formulé le problème de fusion des données en un problème de détection exploitant directement les signaux issus des deux types de capteurs. Bien que prometteuse, cette solution se heurte à un problème de charge calculatoire et des difficultés de mise en œuvre liées au nombre important de paramètres inconnus contenus dans le message AIS. En effet, celui-ci n'a pas été conçu pour un traitement par filtrage adapté mais pour

un décodage plus standard, basé sur la détection de ses séquences de synchronisation. D'autre part, il existe des bases de données accessibles gratuitement, diffusant, en temps réel, les positions des bateaux qui transmettent leur message AIS à la surface du globe. Le site marinetraffic.com est un exemple de ce type de bases de données résultant de mesures collaboratives à différents points du globe. Ces deux constatations nous poussent à étudier un nouveau schéma de fusion des données basé sur l'exploitation des signaux radar bruts assistée d'une base de donnée des positions de bateaux donnée a priori (méthode dénommée fusion de niveau 2 dans le chapitre 1).

Ce problème de fusion avec des données « mixtes » (brutes pour le radar et déjà traitées pour l'AIS) peut également être formulé de la façon suivante : est-il possible d'améliorer la détection radar connaissant une liste a priori de positions de bateau fournie par l'AIS ? Cette question peut-être décomposée en deux sous-questions que nous traiterons en deux étapes successives.

1. Est-ce que la liste des positions disponibles est valide ?
2. Existe-t-il d'autres bateaux dans la zone ?

A partir de ces questions on peut définir quatre hypothèses liées au problème de détection :

H_0 : il n'y a pas de bateau dans la case radar sous test (pas de position AIS correspondant cette case dans la liste, confirmé par le radar)

H_1 : il y a un bateau coopératif dans la case sous test (position de la liste AIS confirmée par le radar)

H_2 : il y a un bateau dans la case sous test sans signal AIS (le radar détecte un bateau ne correspondant à aucune position de la liste AIS). Ce cas regroupe les petits bateaux ne possédant pas d'AIS et les bateaux n'ayant pas transmis (volontairement ou non) leur position. Cette situation peut également correspondre au cas de bateaux qui biaisent volontairement leur position AIS (pêche illégale, piraterie) de manière à masquer leurs positions, sans éveiller de soupçons. Ce cas sera alors également détecté, dans la case correspondant à la position biaisée, par la dernière hypothèse de travail, H_3.

H_3 : il n'y a pas de bateau dans la case sous test mais on devrait en avoir un, au vu de la liste AIS (position AIS non confirmée par le radar).

Comme nous l'avons vu précédemment, les positions AIS sont mises à jour avec une répétition assez lente (pouvant aller jusqu'à 3 minutes) et de manière non synchronisée pour chaque bateau. Comme la vitesse, le cap et la datation des mesures des navires sont transmis par les messages AIS, il est cependant possible d'extrapoler les positions des bateaux de la liste pour les comparer aux données radar acquises à un instant différent. Deux hypothèses peuvent alors être envisagées

- La résolution du radar est suffisamment grande (bande basse) pour que l'on puisse considérer que l'on ne commet pas d'erreur quant à l'extrapolation des positions AIS sur les cases radar.
- La résolution du radar est fine (bande large) de manière à pouvoir intégrer une erreur de position éventuelle des positions AIS extrapolées sur les cases radar.

Focalisons-nous, dans un premier temps, sur le cas le plus simple où l'on considère que l'on ne commet pas d'erreur a priori sur les positions des bateaux à partir des mesures AIS. La première étape consiste à vérifier que la liste des positions AIS correspond bien à des positions renvoyant de l'énergie radar au sol. Pour cela, il suffit de tester les positions de la liste AIS $\boldsymbol{\theta}_{\text{AIS}} = \left[\boldsymbol{\theta}_{\text{AIS}_1}, \ldots, \boldsymbol{\theta}_{\text{AIS}_{N_{\text{AIS}}}}\right]^T$ une à une, en supposant que les autres positions de la liste sont valides (on suppose que seule une erreur est possible à chaque test). Le problème peut donc se formaliser par un test d'hypothèses binaires :

$$\text{pour chaque } \boldsymbol{\theta}_{\text{AIS}_i} \in \boldsymbol{\theta}_{\text{AIS}}$$

$$\begin{cases} \boldsymbol{y}_{\text{rad}} = \boldsymbol{A}_{\sim i}\boldsymbol{\alpha}_{\sim i} + \boldsymbol{n}_{\text{rad}} & \text{under } H_3 \\ \boldsymbol{y}_{\text{rad}} = \boldsymbol{A}_{\sim i}\boldsymbol{\alpha}_{\sim i} + \beta\boldsymbol{a}(\boldsymbol{\theta}_{\text{AIS}_i}) + \boldsymbol{n}_{\text{rad}} & \text{under } H_1 \end{cases}$$

où $\boldsymbol{A}_{\sim i} = \left[\boldsymbol{a}(\boldsymbol{\theta}_{\text{AIS}_1}), \ldots, \boldsymbol{a}(\boldsymbol{\theta}_{\text{AIS}_{i-1}}), \boldsymbol{a}(\boldsymbol{\theta}_{\text{AIS}_{i+1}}), \ldots, \boldsymbol{a}(\boldsymbol{\theta}_{\text{AIS}_{N_{\text{AIS}}}})\right]$ regroupe, en colonne les $(N_{\text{AIS}} - 1)$ signatures de la liste des positions AIS non testées à l'étape i et $\boldsymbol{\alpha}_{\sim i}$ les $(N_{\text{AIS}} - 1)$ amplitudes.

Après cette première étape de confirmation, on obtient une liste des bateaux confirmés $\boldsymbol{\theta}_{\mathrm{AIS}_{\mathrm{conf}}}$ (hypothèse H_1). Lors d'une deuxième étape, nous pouvons donc maintenant tester la présence de nouveaux bateaux en dehors de la liste des positions a priori. Ce problème peut être formulé de la manière suivante :

$$\text{pour chaque } \boldsymbol{\theta} \notin \boldsymbol{\theta}_{\mathrm{AIS}_{\mathrm{conf}}}$$

$$\begin{cases} \boldsymbol{y}_{\mathrm{rad}} = \boldsymbol{A}\boldsymbol{\alpha} + \boldsymbol{n}_{\mathrm{rad}}, & \text{sous } H_0 \\ \boldsymbol{y}_{\mathrm{rad}} = \boldsymbol{A}\boldsymbol{\alpha} + \beta\boldsymbol{a}(\boldsymbol{\theta}) + \boldsymbol{n}_{\mathrm{rad}}, & \text{sous } H_2 \end{cases}$$

où $\boldsymbol{A}$ regroupe, cette fois en colonne les $N_{\mathrm{AIS}_{\mathrm{conf}}}$ signatures radar correspondant aux positions des bateaux confirmés.

On voit que les modèles présentés lors des 2 étapes successives sont identiques. Nous allons donc nous focaliser sur la deuxième étape pour développer le test GLRT associé. Le même détecteur sera alors valide pour la première étape, en utilisant la matrice $\boldsymbol{A}_{\sim i}$ en lieu et place de la matrice $\boldsymbol{A}$ et en limitant la zone de recherche au positions $\boldsymbol{\theta}$ de la liste AIS.

En considérant les amplitudes des différents échos radar $\boldsymbol{\alpha}$ ainsi que la puissance du bruit σ^2_{rad} inconnues, on obtient l'expression suivante de la statistique du test GLRT

$$\frac{\|\acute{\boldsymbol{a}}^H \acute{\boldsymbol{y}}\|^2}{\|\acute{\boldsymbol{a}}\|^2 \|\acute{\boldsymbol{y}}\|^2} \underset{H_0}{\overset{H_1}{\gtrless}} \eta_{\mathrm{p}}$$

où $\acute{\boldsymbol{a}} = \boldsymbol{P}^{\perp}_{\boldsymbol{A}}\boldsymbol{a}(\boldsymbol{\theta})$ and $\acute{\boldsymbol{y}} = \boldsymbol{P}^{\perp}_{\boldsymbol{A}}\boldsymbol{y}_{\mathrm{rad}}$ sont les projections de la signature radar recherchée et du signal radar sur le sous-espace orthogonal aux signatures des bateaux déjà répertoriés.

De par l'inégalité de Cauchy-Schwarz, ce test peut être interprété comme une mesure du cosinus carré de l'angle entre les vecteurs $\acute{\boldsymbol{a}} = \boldsymbol{P}^{\perp}_{\boldsymbol{A}}\boldsymbol{a}$ et $\acute{\boldsymbol{y}} = \boldsymbol{P}^{\perp}_{\boldsymbol{A}}\boldsymbol{y}_{\mathrm{rad}}$ vecteurs auxquels on a supprimé préalablement les interférences liées aux cibles déjà connues par l'AIS. Il suffit alors de comparer ce test à un seuil pour décider entre les hypothèses H_0 et H_2. La valeur du seuil est fixée en fonction de la P_{fa} désirée. On peut également noter que ce test est à taux de fausse alarme constant (CFAR).

Ce processus de détection permet d'une part de fusionner de manière naturelle les informations AIS et radar, mais peut également améliorer la performance en détection du radar. Pour évaluer

ce gain éventuel en terme de détection, nous allons comparer notre détecteur au détecteur GLRT utilisant les données radar sans connaissance a priori de la liste AIS. Sous l'hypothèse d'une puissance de bruit inconnue, ce dernier est le détecteur appelé « CFAR matched detector » dont la statistique de test est

$$T_{\mathrm{c}} = \frac{\boldsymbol{y}_{\mathrm{rad}}^H \boldsymbol{P}_{\boldsymbol{a}} \boldsymbol{y}_{\mathrm{rad}}}{\boldsymbol{y}_{\mathrm{rad}}^H \boldsymbol{P}_{\boldsymbol{a}}^{\perp} \boldsymbol{y}_{\mathrm{rad}}}$$

L'analyse des lois des statistiques de ces deux tests permet de montrer qu'elles suivent des lois de Fisher centrées et décentrées, en fonction de l'hypothèse valide. Ces lois permettent de comparer, de manière théorique, leurs performances en terme de courbes ROC (P_d en fonction de P_{fa}). Les tracés de ces courbes théoriques permettent de montrer que les performances dépendent de la densité de bateaux connus à proximité de la case sous test. Plus la densité des bateaux connus de par la liste AIS est grande, plus la performance chute. Néanmoins, de par sa construction, le détecteur proposé, qui élimine les interférences des bateaux déjà connus est beaucoup moins sensible à cet effet et ses performances sont quasi constantes en fonction de la densité de bateaux. On observe le même phénomène en fonction de l'éloignement et de la taille des bateaux à proximité de la case sous test. Logiquement, plus le bateau répertorié est gros et proche de la case sous test, plus la détection d'un nouveau bateau sera délicate. Cet effet est néfaste mais grandement atténué par le nouveau détecteur.

Enfin, pour finir ce chapitre, nous nous sommes intéressé au cas où les positions de bateaux de la liste AIS peuvent contenir des erreurs, du fait de leur extrapolation à la date de prise de vue radar. Dans ce cas, on peut modifier le modèle d'observation en intégrant du bruit sur ces mesures de position, comme suit :

$$\begin{cases} \boldsymbol{y}_{\mathrm{rad}} = \boldsymbol{A}\left(\boldsymbol{\theta}_r\right)\boldsymbol{\alpha} + \beta \boldsymbol{a}\left(\boldsymbol{\theta}\right) + \boldsymbol{n}_{\mathrm{rad}} \\ \boldsymbol{\theta}_{\mathrm{a}} = \boldsymbol{\theta}_r + \boldsymbol{n}_{\mathrm{a}} \end{cases}$$

où $\boldsymbol{\theta}_r$ représente le vecteur des vraies positions captées par le radar et $\boldsymbol{\theta}_a$ les positions extrapolées sujettes à des erreurs modélisées de manière gaussiennes par $\boldsymbol{n}_a$.

On peut supposer que la puissance de ces erreurs de positionnement peut être estimée connaissant la précision des mesures AIS brutes (position, vitesse, datation) ainsi que la durée d'extrapolation. De même, on peut supposer que l'on a accès à des données radar secondaires pour déterminer la puissance du bruit des mesures radar. On peut alors calculer un nouveau détecteur intégrant ces erreurs de mesures AIS. Ce nouveau détecteur GLRT présente un terme correctif dont le poids dépend naturellement de la puissance (supposée connue) des erreurs sur les positions. Des simulations permettent de comparer le comportement de ce nouveau détecteur avec le détecteur ne prenant pas en compte d'erreurs de position.

3.2 Introduction

In the previous chapter we decided to explore the fusion of raw AIS and radar data in order to preserve the maximum of information. We formulated the problem of data fusion into a detection problem by exploring directly the raw data from both sensors. While promising, the proposed solution has high computational cost and is difficult to implement due to the number of unknown parameters in the AIS message. The AIS is a telecomunication signal and it was not conceived for matched filtering reception, but instead, to be decoded using a more simple scheme based on detecting the synchronization sequences and then using bit decoding with the possibility of error detection by using the CRC block to assure message integrity.

The data obtained from AIS decoded messages provides useful information about ships positioning. In a surveillance scenario, this may be used not only to inform about the cooperative ships but also to improve detection and classify ship detections. Also, AIS decoded information is available from other sources than from the direct acquisition. The website "www.marinetraffic.com" for example is one service that offers real time AIS processed data. For those reasons, we direct our research to a more feasible fusion scheme, where we consider exploring the radar raw data assisted by a secondary data source, providing a list of "know" ship positions (that may have errors and need to be validated) named "the fusion level two" in the list of data fusion methods presented in chapter one.

Moreover, there are many challenges that need to be dealt it. In the first chapter we cite some important surveillance scenarios like, e.g., navigating in crowded areas (the North sea, Mediterranean, the English channel, among others). The detection of ships that are close range or near the coastal area are more examples of scenarios that are specifically challenging to deal with. We will see that a conventional detector (that uses only raw radar data) may have a non uniform detection performance in those cases. We propose a different model for the ship detection problem and compare the performance between the conventional radar detector with a proposed detector in some surveillance specific scenarios.

In this chapter, we propose a detector that uses the vessel position provided by the AIS system to improve the radar detection performance. This time the processed AIS data is used as secondary information for the radar detector in order to improve the detection performance. The idea is also to use a detector that is able to separate target into four different surveillance hypotheses, namely to classify targets as a new detection, a non detection, a confirmation of a target or a false alarm. Besides the classification of targets, the proposed detector shall be used for detecting ships that are not in the AIS list (non cooperative ships), which we expect to observe a performance gain in ship detection by using AIS positioning with radar raw data.

First we introduce the signal models associated with the radar signals and with the AIS detection map. Section 3.4 introduces the problem and issues addressed in this work. Section 3.5 investigates the GLRT based on the proposed detection problem. Section 3.6 derives the probability distributions of the test statistics that are used to determine performance using ROC curves. Section 3.7 compares the detection performance obtained for both theoretical and simulated data in different scenarios. We clearly show the gain of using a detector combining AIS and SAR data when compared to the classical radar detector for scenarios characterized by different ship scenario configuration like different ship densities, sizes or the distance between ships. Afterwards, we present a model that considers the case that AIS positioning error is greater than the radar resolution. To finish, we draw our conclusions in Section 3.9.

3.3 Signal model

AIS processed data

AIS messages are transmitted every 2 to 10 seconds for moving ships and every 3 minutes for the anchored ones [ITU14]. The AIS information can be obtained in different ways: They may be acquired onboard a satellite embedding AIS receiver, or may be gathered from some AIS databse (an example of AIS database may be found in www.marinetraffic.com). Mainly due to the asynchronous nature of AIS, the list of positions provided by the AIS usually does not coincide with ship positions associated with radar snapshots. This leads to ship positioning errors that need to be considered accurately. A simple approach consists of propagating the AIS detection map by using information contained in AIS messages, such as, e.g., ship heading, speed, rate of turn indicator and message timestamps. Moreover, precision may be improved when multiple AIS messages from the same ship are available. In practice, the majority of ships travel on straight lines and a simple linear extrapolation may be sufficient to propagate the AIS positions. Propagation of the AIS positions up to the radar time measurement may be done by simple extrapolation of positions using target speed, heading and timestamp. Also, we consider here at first that the positioning interpolation errors are lower than the radar resolution so that their impact on detector performance can be neglected. The AIS positions list after being propagated to the current radar scene instant is represented by $\boldsymbol{\theta}_{\text{AIS}}$.

3.4 Problem statement

Referring to the radar model in Section 2.3.2, in this case we no more consider the raw AIS signals but the list of AIS positions $\boldsymbol{\theta}_{\text{AIS}}$. If we consider the coordinates, ship speeds and also the time of reception of the AIS message of each ship in the area of interest, we may propagate those positions to the instant of reception of the radar signal $\boldsymbol{\theta}_{\text{AIS}_{\text{prop}}}$. For simplicity, we will omit the suffix "prop" and by $\boldsymbol{\theta}_{\text{AIS}}$ we are referring uniquely to the already propagated list of AIS ship positions. The radar raw signal at the satellite receiver is

$$\boldsymbol{y}_{\text{rad}} = \boldsymbol{A}\left(\boldsymbol{\theta}_{\text{AIS}}\right)\boldsymbol{\alpha} + \beta\boldsymbol{a}\left(\boldsymbol{\theta}\right) + \boldsymbol{n}_{\text{rad}} \tag{3.1}$$

where $\boldsymbol{A}(\boldsymbol{\theta}_{\text{AIS}})$ is a $N_{\text{rad}} \times N_{\text{AIS}}$ matrix containing N_{AIS} radar signatures of the cooperative targets at the positions in vector $\boldsymbol{\theta}_{\text{AIS}}$, and $\boldsymbol{a}(\boldsymbol{\theta})$ is the radar signature at the test position $\boldsymbol{\theta} \notin \boldsymbol{\theta}_{\text{AISprop}}$ with unknown signal amplitude β, and vector $\boldsymbol{\alpha} = (\alpha_1, \ldots, \alpha_{N_{\text{AIS}}})^T$ is the unknown amplitudes of the radar signals corresponding to the cooperative ships in the AIS positions.

Here, we consider that the AIS ship detection list may be incomplete (or corrupted), where we have to discriminate among four hypotheses: Hypothesis H_0 corresponds to the absence of ship (confirmed by the radar and the AIS), hypothesis H_1 is associated with a radar echo from a ship whose position is known from the AIS list (a cooperative ship confirmed), whereas hypothesis H_2 represents a radar echo from an unknown ship (a non-cooperative ship detected with the radar) and lastly, hypothesis H_3 corresponds to the absence of radar echo at an AIS reported position (an AIS error, deliberate or not).

The hypothesis H_3 indicates a problem that is observable only when using both AIS and radar associated. In this case the AIS position does not match to a radar detection, indicating that the AIS information is either biased to a position farther than the radar resolution, or represents a false AIS data, situation that may be intentional or not. In some maritime surveillance scenarios like in illegal fishing, AIS data may be intentionally forged by fishing vessels in order to avoid authorities surveillance or concurrent fishers that searchs for good fishing zones. In hypothesis H_2 there are ship detection that does not transmit their AIS position but are confirmed by the radar, representing in surveillance scenarios situations like an illegal cargo operation, where ships intentionally turn of their AIS in order to proceed with the illegal activity, or some ships that does not have an AIS transmitter. The cases of hypotheses H_1 and H_2 are, respectively the confirmation of a ship and a non-detection of a position that is not in the AIS list.

We conduct a two-step procedure in order to decide between the different hypotheses:

1. Confirmation of the AIS ship positions

   In this step we exclusively test the AIS positions in order to confirm the presence (or the absence) of ships with the radar. We are interested in testing if each of AIS positions $\boldsymbol{\theta}_{\text{AIS}_i}$

corresponds to a radar detection. For this first stage, the model to consider is

$$\boldsymbol{y}_{\text{rad}} = \boldsymbol{A}_{\sim i}\left(\boldsymbol{\theta}_{\text{AIS}_{\sim i}}\right)\boldsymbol{\alpha}_{\sim i} + \alpha_i \boldsymbol{a}\left(\boldsymbol{\theta}_{\text{AIS}_i}\right) + \boldsymbol{n}_{\text{rad}} \tag{3.2}$$

where $i \in \{1, \ldots, N_{\text{AIS}}\}$ represents the index of a ship in the AIS positioning list $\boldsymbol{\theta}_{\text{AIS}} = \left(\boldsymbol{\theta}_{\text{AIS}_1}, \ldots, \boldsymbol{\theta}_{\text{AIS}_{N_{\text{AIS}}}}\right)$, being $\boldsymbol{\theta}_{\text{AIS}_i}$ the i-th AIS position to test while $\boldsymbol{\theta}_{\text{AIS}_{\sim i}}$ are the remaining ones. $\boldsymbol{A}_{\sim i}$ is a $N_{\text{rad}} \times (N_{\text{AIS}} - 1)$ matrix whose columns contain the radar signatures corresponding to the remaining $(N_{\text{AIS}} - 1)$ positions in the AIS list. α_i and $\boldsymbol{\alpha}_{\sim i}$ represent the complex amplitudes of the radar signals from the AIS list at, respectively, the i-th position and the remaining ones. The binary hypothesis test used to validate the AIS positions consists testing whether α_i is zero or not, distinguishing each ship in $\boldsymbol{\theta}_{\text{AIS}}$ between the two hypotheses H_1 (cooperative ship confirmed) and H_3 (AIS biased ship).

2. Detection of unknown ships

   After validating the AIS list $\boldsymbol{\theta}_{\text{AIS}_{\text{conf}}}$, the two hypotheses H_0 (no ship) and H_2 (ship detection without AIS) can be tested for all other positions $\boldsymbol{\theta}$ that do not belong to the AIS list, i.e., for $\boldsymbol{\theta} \notin \boldsymbol{\theta}_{\text{AIS}_{\text{conf}}}$

$$\boldsymbol{y}_{\text{rad}} = \boldsymbol{A}\left(\boldsymbol{\theta}_{\text{AIS}_{\text{conf}}}\right)\boldsymbol{\alpha}_{\text{conf}} + \beta \boldsymbol{a}\left(\boldsymbol{\theta}\right) + \boldsymbol{n}_{\text{rad}}. \tag{3.3}$$

3.5 Generalized Likelihood Ratio Test

We are interested in solving the following binary hypothesis test problem

$$H_0 : \beta = 0 \text{ (absence of ship)} \tag{3.4}$$

$$H_2 : \beta \neq 0 \text{ (presence of ship)} \tag{3.5}$$

considering the radar noise power σ^2_{rad} and the signal amplitudes $\boldsymbol{\alpha}$ and β as unknown. The GLRT compares the following quantity

$$\frac{p(\boldsymbol{y}_{\text{rad}}|\hat{\sigma}^2_1, \hat{\boldsymbol{\alpha}}_1, \hat{\beta}_1, \boldsymbol{\theta}_{\text{AIS}_{\text{conf}}}, \boldsymbol{\theta}, H_2)}{p(\boldsymbol{y}_{\text{rad}}|\hat{\sigma}^2_0, \hat{\boldsymbol{\alpha}}_0, \beta = 0, \boldsymbol{\theta}_{\text{AIS}_{\text{conf}}}, \boldsymbol{\theta}, H_0)} \tag{3.6}$$

to an appropriate threshold, where $\hat{\boldsymbol{\alpha}}_i$ and $\hat{\beta}_i$ are the maximum likelihood estimators (MLE) of the signal amplitudes under the hypothesis H_i, $p(\boldsymbol{y}_{\text{rad}}|\sigma_i^2, \boldsymbol{\alpha}_i, \beta_i, H_i)$ is the probability density function of the radar measurement vector $\boldsymbol{y}_{\text{rad}}$ at test position $\boldsymbol{\theta}$. The probability density function is show to be

$$p(\boldsymbol{y}_{\text{rad}}|\sigma_{\text{rad}}^2, \boldsymbol{\alpha}, \beta, \boldsymbol{\theta}_{\text{AIS}}, \boldsymbol{\theta}, H_i) = \left(\pi\sigma_{\text{rad}}^2\right)^{-N_{\text{rad}}} \exp\left\{-\frac{\|\boldsymbol{y}_{\text{rad}} - \boldsymbol{A}\boldsymbol{\alpha} - \beta\boldsymbol{a}\|^2}{\sigma_{\text{rad}}^2}\right\}, \tag{3.7}$$

where we write $\boldsymbol{a}$ and $\boldsymbol{A}$ instead of respectively $\boldsymbol{a}(\boldsymbol{\theta})$ and $\boldsymbol{A}(\boldsymbol{\theta}_{\text{AIS}})$ to shorten notation. It is straightforward to show that the unknown parameters σ_{rad}^2, $\boldsymbol{\alpha}$, β have their MLE estimates respectively given by

$$\begin{aligned}
\hat{\sigma}_{\text{rad}}^2 &= \|\boldsymbol{y}_{\text{rad}} - \boldsymbol{A}\boldsymbol{\alpha} - \beta\boldsymbol{a}\|^2 / N_{\text{rad}} \\
\hat{\boldsymbol{\alpha}} &= \boldsymbol{A}^+ \left(\boldsymbol{y}_{\text{rad}} - \beta\boldsymbol{a}\right) \\
\hat{\beta} &= \left(\boldsymbol{a}^H \boldsymbol{P}_{\boldsymbol{A}}^{\perp} \boldsymbol{a}\right)^{-1} \boldsymbol{a}^H \boldsymbol{P}_{\boldsymbol{A}}^{\perp} \boldsymbol{y}_{\text{rad}},
\end{aligned}$$

with $\boldsymbol{A}^+ = (\boldsymbol{A}^H\boldsymbol{A})^{-1}\boldsymbol{A}^H$ representing the pseudo-inverse of $\boldsymbol{A}(\boldsymbol{\theta}_{\text{AIS}_{\text{conf}}})$, $\boldsymbol{P}_{\boldsymbol{A}} = \boldsymbol{A}\boldsymbol{A}^+$ is the projection matrix onto the subspace containing all the ships belonging to the AIS list $\boldsymbol{\theta}_{\text{AIS}_{\text{conf}}}$, and $\boldsymbol{P}_{\boldsymbol{A}}^{\perp} = \boldsymbol{I} - \boldsymbol{P}_{\boldsymbol{A}}$ the orthogonal projection. Replacing the unknown parameters by their respective MLE, we obtain the following probability density functions for both hypotheses H_0 and H_2

$$\begin{aligned}
p(\boldsymbol{y}_{\text{rad}}|\hat{\sigma}_{\text{rad}}^2, \hat{\boldsymbol{\alpha}}, \beta = 0, \boldsymbol{\theta}_{\text{AIS}}, \boldsymbol{\theta}, H_0) &= \left(\frac{\pi e}{N_{\text{rad}}}\|\boldsymbol{y}_{\text{rad}} - \boldsymbol{A}\hat{\boldsymbol{\alpha}}\|^2\right)^{-N_{\text{rad}}} \\
p(\boldsymbol{y}_{\text{rad}}|\hat{\sigma}_{\text{rad}}^2, \hat{\boldsymbol{\alpha}}, \hat{\beta}, \boldsymbol{\theta}_{\text{AIS}}, \boldsymbol{\theta}, H_2) &= \left(\frac{\pi e}{N_{\text{rad}}}\|\boldsymbol{y}_{\text{rad}} - \boldsymbol{A}\hat{\boldsymbol{\alpha}} - \hat{\beta}\boldsymbol{a}\|^2\right)^{-N_{\text{rad}}}
\end{aligned}$$

where straightforward computations show that

$$l = \begin{cases} \left(\frac{\pi e}{N_{\text{rad}}}\right)^{-N_{\text{rad}}} \left(\boldsymbol{y}_{\text{rad}}^H \boldsymbol{P}_{\boldsymbol{A}}^{\perp} \boldsymbol{y}_{\text{rad}}\right)^{-N_{\text{rad}}} & \text{under } H_0 \\ \left(\frac{\pi e}{N_{\text{rad}}}\right)^{-N_{\text{rad}}} \left(\boldsymbol{y}_{\text{rad}}^H \boldsymbol{P}_{\boldsymbol{A}}^{\perp} \boldsymbol{y}_{\text{rad}} - \frac{\boldsymbol{y}_{\text{rad}}^H \boldsymbol{P}_{\boldsymbol{A}}^{\perp} \boldsymbol{a}\boldsymbol{a}^H \boldsymbol{y}_{\text{rad}}}{\boldsymbol{a}^H \boldsymbol{P}_{\boldsymbol{A}}^{\perp} \boldsymbol{a}}\right)^{-N_{\text{rad}}} & \text{under } H_2, \end{cases}$$

are the likelihoods functions with respect to each hypothesis. The GLRT in (3.6) may be written

$$\frac{p(\boldsymbol{y}_{\text{rad}}|\hat{\sigma}_1^2, \hat{\boldsymbol{\alpha}}_1, \hat{\beta}_1, \boldsymbol{\theta}_{\text{AIS}}, \boldsymbol{\theta}, H_2)}{p(\boldsymbol{y}_{\text{rad}}|\hat{\sigma}_0^2, \hat{\boldsymbol{\alpha}}_0, \beta = 0, \boldsymbol{\theta}_{\text{AIS}}, \boldsymbol{\theta}, H_0)} = \left[\frac{\boldsymbol{y}_{\text{rad}}^H \boldsymbol{P}_{\boldsymbol{A}}^{\perp} \boldsymbol{y}_{\text{rad}}}{\boldsymbol{y}_{\text{rad}}^H \boldsymbol{P}_{\boldsymbol{A}}^{\perp} \boldsymbol{y}_{\text{rad}} - \frac{\boldsymbol{y}_{\text{rad}}^H \boldsymbol{P}_{\boldsymbol{A}}^{\perp} \boldsymbol{a}\boldsymbol{a}^H \boldsymbol{P}_{\boldsymbol{A}}^{\perp} \boldsymbol{y}_{\text{rad}}}{\boldsymbol{a}^H \boldsymbol{P}_{\boldsymbol{A}}^{\perp} \boldsymbol{a}}}\right]^{N_{\text{rad}}}. \tag{3.8}$$

Taking the N_{rad}th-root and after some manipulations, we obtain the GLRT

$$T_{\text{p}} = \frac{\boldsymbol{y}_{\text{rad}}^H \boldsymbol{P}_{\boldsymbol{A}}^{\perp} \boldsymbol{a}\boldsymbol{a}^H \boldsymbol{P}_{\boldsymbol{A}}^{\perp} \boldsymbol{y}_{\text{rad}}}{\left(\boldsymbol{a}^H \boldsymbol{P}_{\boldsymbol{A}}^{\perp} \boldsymbol{a}\right)\left(\boldsymbol{y}_{\text{rad}}^H \boldsymbol{P}_{\boldsymbol{A}}^{\perp} \boldsymbol{y}_{\text{rad}}\right)} = \frac{\|\acute{\boldsymbol{a}}^H \acute{\boldsymbol{y}}\|^2}{\|\acute{\boldsymbol{a}}\|^2 \|\acute{\boldsymbol{y}}\|^2} \underset{H_0}{\overset{H_1}{\gtrless}} \eta_{\text{p}} \tag{3.9}$$

where $\acute{\boldsymbol{a}} = \boldsymbol{P}_{\boldsymbol{A}}^{\perp} \boldsymbol{a}(\boldsymbol{\theta})$ and $\acute{\boldsymbol{y}} = \boldsymbol{P}_{\boldsymbol{A}}^{\perp} \boldsymbol{y}_{\text{rad}}$ are respectively the signal and the measurement vectors projected onto the subspace orthogonal to the confirmed AIS positions, η_{p} is the detection threshold to be chosen with respect to the desired performance in terms of P_d and P_{fa}. The proposed detector T_{p} is a constant false-alarm rate (CFAR) that compare the square of the cosine of the angle between two vectors: the measurement vector $\boldsymbol{y}_{\text{rad}}$ and the radar signature vector $\boldsymbol{a}(\boldsymbol{\theta})$ after both being projected onto the space of the radar signatures orthogonal to the AIS position list $\boldsymbol{\theta}_{\text{AIS}_{\text{conf}}}$.

Alternatively, one may consider an equivalent GLRT statistic which is also invariant to the same group of transformations that makes T_{p} invariant [Sch91]. Noticing that $\frac{\acute{\boldsymbol{y}}^H \acute{\boldsymbol{a}} \acute{\boldsymbol{a}}^H \acute{\boldsymbol{y}}}{\acute{\boldsymbol{a}}^H \acute{\boldsymbol{a}}} = \acute{\boldsymbol{y}}^H \boldsymbol{P}_{\acute{\boldsymbol{a}}} \acute{\boldsymbol{y}}$ and $\acute{\boldsymbol{y}}^H \acute{\boldsymbol{y}} = \acute{\boldsymbol{y}}^H \boldsymbol{P}_{\acute{\boldsymbol{a}}} \acute{\boldsymbol{y}} + \acute{\boldsymbol{y}}^H \boldsymbol{P}_{\acute{\boldsymbol{a}}}^{\perp} \acute{\boldsymbol{y}}$, taking the N_{rad}th-root of (3.8) we obtain

$$T'_{\text{p}} = \frac{\acute{\boldsymbol{y}}^H \boldsymbol{P}_{\acute{\boldsymbol{a}}} \acute{\boldsymbol{y}}}{\acute{\boldsymbol{y}}^H \boldsymbol{P}_{\acute{\boldsymbol{a}}}^{\perp} \acute{\boldsymbol{y}}} \tag{3.10}$$

which is also a ratio of quadratic forms in projection matrices that measures the energy of $\boldsymbol{y}_{\text{rad}}$ that lies in the subspace defined by $\boldsymbol{P}_{\acute{\boldsymbol{a}}}$. Observe that $T_{\text{p}} = \frac{T'_{\text{p}}}{T'_{\text{p}}+1}$.

To evaluate the performance we compare the proposed detector T_p with the standard matched detector in the hypothesis of unknown noise power

$$T_{\text{c}} = \frac{\boldsymbol{y}_{\text{rad}}^H \boldsymbol{P}_{\boldsymbol{a}} \boldsymbol{y}_{\text{rad}}}{\boldsymbol{y}_{\text{rad}}^H \boldsymbol{P}_{\boldsymbol{a}}^{\perp} \boldsymbol{y}_{\text{rad}}} \underset{H_0}{\overset{H_1}{\gtrless}} \eta_{\text{c}} \tag{3.11}$$

is the CFAR matched subspace detector (available in [Sch91]) where $\boldsymbol{P}_{\boldsymbol{a}} = \boldsymbol{a}(\boldsymbol{\theta}) \left[\boldsymbol{a}(\boldsymbol{\theta})^H \boldsymbol{a}(\boldsymbol{\theta})\right]^{-1} \boldsymbol{a}(\boldsymbol{\theta})^H$ and $\boldsymbol{P}_{\boldsymbol{a}}^{\perp} = \boldsymbol{I} - \boldsymbol{P}_{\boldsymbol{a}}$ are both the projection matrices associated respectively with the radar signal subspace and its orthogonal.

3.6 Performance analysis

In the sequel, $F_{n,m}(\lambda)$ denotes a real noncentral Fisher distribution (F-distribution) with n, m degrees of freedom and noncentrality parameter λ. Moreover, we use the notation $W \sim \rho F_{n,m}(\lambda)$ for a

random variable W such that W/ρ has an F-distribution $F_{n,m}(\lambda)$. Of course, the noncentral $F_{n,m}(\lambda)$ distribution reduces to a central F-distribution with n, m degrees of freedom when $\lambda = 0$.

3.6.1 Distribution of the test statistic $T_{\mathbf{p}}$

As $\boldsymbol{n}_{\text{rad}}$ is supposed to be Gaussian, T_{p} is (up to a multiplicative constant) the ratio of a central under a noncentral chi-square distribution under hypotheses H_0 and H_2 which is known as a Fisher distribution [Sch91].

Degrees of freedom

We evaluate the numerator and denominator of T_{p} separately. Consider $\boldsymbol{Q}$ an orthogonal matrix such that $\boldsymbol{Q}^H \boldsymbol{P}_{\boldsymbol{A}} \boldsymbol{Q} = \boldsymbol{I}_k$ and $\boldsymbol{P}_{\boldsymbol{A}} = \boldsymbol{Q}\boldsymbol{I}_k\boldsymbol{Q}^H$, which $\boldsymbol{I}_k$ notation indicate that $\boldsymbol{I}$ is a $n \times n$ diagonal matrix with k ones and $n-k$ zeros so that $\text{rank}(\boldsymbol{I}_k) = k$. For the denominator we have

$$\begin{aligned} \boldsymbol{y}_{\text{rad}}^H \boldsymbol{P}_{\boldsymbol{A}}^{\perp} \boldsymbol{P}_{\acute{a}} \boldsymbol{P}_{\boldsymbol{A}}^{\perp} \boldsymbol{y}_{\text{rad}} &= \boldsymbol{y}_{\text{rad}}^H \boldsymbol{Q}\boldsymbol{I}_{n-k}\boldsymbol{Q}^H \boldsymbol{Q}\boldsymbol{I}_1\boldsymbol{Q}^H \boldsymbol{Q}\boldsymbol{I}_{n-k}\boldsymbol{Q}^H \boldsymbol{y}_{\text{rad}} \\ &= \boldsymbol{y}_{\text{rad}}^H \boldsymbol{Q}\boldsymbol{I}_{n-k}\boldsymbol{I}_1\boldsymbol{I}_{n-k}\boldsymbol{Q}^H \boldsymbol{y}_{\text{rad}}. \end{aligned} \tag{3.12}$$

This way, $\text{rank}(\boldsymbol{I}_{n-k}\boldsymbol{I}_1\boldsymbol{I}_{n-k}) = 1$.

Proof: As $\boldsymbol{a} \perp \boldsymbol{A}$, $< \boldsymbol{I}_1, \boldsymbol{I}_{n-k} >= \boldsymbol{I}_1$. Then $\text{rank}(\boldsymbol{I}_{n-k}\boldsymbol{I}_1\boldsymbol{I}_{n-k}) = \text{rank}(\boldsymbol{I}_1) = 1$.

Evaluating the numerator

$$\begin{aligned} \boldsymbol{y}_{\text{rad}}^H \boldsymbol{P}_{\boldsymbol{A}}^{\perp} \boldsymbol{P}_{\acute{a}}^{\perp} \boldsymbol{P}_{\boldsymbol{A}}^{\perp} \boldsymbol{y}_{\text{rad}} &= \boldsymbol{y}_{\text{rad}}^H \boldsymbol{Q}\boldsymbol{I}_{n-k}\boldsymbol{Q}^H \boldsymbol{Q}\boldsymbol{I}_{n-1}\boldsymbol{Q}^H \boldsymbol{Q}\boldsymbol{I}_{n-k}\boldsymbol{Q}^H \boldsymbol{y}_{\text{rad}} \\ &= \boldsymbol{y}_{\text{rad}}^H \boldsymbol{Q}\boldsymbol{I}_{n-k}\boldsymbol{I}_{n-1}\boldsymbol{I}_{n-k}\boldsymbol{Q}^H \boldsymbol{y}_{\text{rad}}, \end{aligned} \tag{3.13}$$

where $\text{rank}(\boldsymbol{I}_{n-k}\boldsymbol{I}_{n-1}\boldsymbol{I}_{n-k}) = n-k-1$.

Proof:

$$\begin{aligned} \text{rank}(\boldsymbol{a}) = 1,\ \boldsymbol{a} \subset < \boldsymbol{A}_{\perp} > \\ \text{rank}(\boldsymbol{a}_{\perp}) = n-1,\ \boldsymbol{a}_{\perp} \subset < \boldsymbol{A} \cup \boldsymbol{A}_{\perp} > \end{aligned} \tag{3.14}$$

As $\boldsymbol{a}_{\perp} \cap \boldsymbol{a} = \emptyset$ and $\boldsymbol{a} \perp \boldsymbol{A}$, then $< \boldsymbol{a}_{\perp} \cap \boldsymbol{A}_{\perp} >=< \boldsymbol{A}_{\perp} - \boldsymbol{a} >$. $\text{rank}(< \boldsymbol{A}_{\perp} - \boldsymbol{a} >) = n-k-1$. The (complex) number of degrees of freedom are $d_1 = 1$ and $d_2 = n-k-1$, where k is the dimension of $< \boldsymbol{A} >$ and n the complete complex vector space $\mathbb{C}^n$.

Probability distribution

The Fisher distribution is defined as: $X = \frac{u/d_1}{w/d_2}$ where u and w are χ^2 distributed with respectively d_1 and d_2 degrees of freedom and being u and w independent. To grant independence of the ratio between χ^2 distributions we use the alternative GLRT formulation T'_{p}

$$T'_{\mathrm{p}} = \frac{\boldsymbol{y'^H P_a(\theta) y'}}{\boldsymbol{y'^H P_a^{\perp}(\theta) y'}} = \frac{\sum_{i=1}^{d_1} \|u_i\|^2}{\sum_{j=1}^{d_2} \|w_j\|^2} \tag{3.15}$$

with $\boldsymbol{u} = \boldsymbol{P_a P_A^{\perp} Q}^H \boldsymbol{y}_{\mathrm{rad}}$ and $\boldsymbol{w} = \boldsymbol{P_a^{\perp} P_A^{\perp} Q}^H \boldsymbol{y}_{\mathrm{rad}}$ are mutually orthogonal transformations of the Gaussian random vector $\boldsymbol{y}_{\mathrm{rad}}$. We granted that the numerator of T'_{p} is orthogonal to the denominator so that

$$T'_{\mathrm{p}} = k \frac{\chi^2_{2d_1}}{\chi^2_{2d_2}} \sim F\left(2d_1, 2d_2, 2\lambda\right) \tag{3.16}$$

is a non-central Fisher distribution where $k = \left(\frac{\sigma^2 d_1}{\sigma^2 d_2}\right) = \frac{d_1}{d_2}$. Notice that the "times 2" in terms is due to the isomorphism between $\mathbb{C} \mapsto \mathbb{R}^2$ (see [DFKE95] for details). Thus, straightforward computations lead to

$$T'_{\mathrm{p}} \sim \begin{cases} \frac{1}{2} F_{2,2(n-k-1)}(0) & \text{under } H_0 \\ \frac{1}{2} F_{2,2(n-k-1)}(\lambda_{\mathrm{p}}) & \text{under } H_2 \end{cases} \tag{3.17}$$

where

$$\lambda_{\mathrm{p}} = 2\beta^2 \|\boldsymbol{P}_A^{\perp}(\boldsymbol{\theta}_{\mathrm{AIS}}) \boldsymbol{a}\left(\boldsymbol{\theta}\right)\|^2 / \sigma^2_{\mathrm{rad}} \tag{3.18}$$

is the noncentrality parameter of the distribution under hypothesis H_2, $n = N_{\mathrm{rad}}$ is the number of radar samples and $k = N_{\mathrm{AIS}}$ is the number of ships that are in the AIS detection list.

3.6.2 Distribution of the test statistic $T_{\mathbf{c}}$

The distribution of the radar as CFAR matched filter in (3.9) is classical (available in [Sch91])

$$T_{\mathrm{c}} \sim \begin{cases} \frac{1}{2} F_{2,2(n-1)}(0) & \text{under } H_0 \\ \frac{1}{2} F_{2,2(n-1)}(\lambda_{\mathrm{c}}) & \text{under } H_2 \end{cases} \tag{3.19}$$

where

$$\lambda_{\mathrm{c}} = 2\beta^2 \|\boldsymbol{a}\left(\boldsymbol{\theta}\right)\|^2 / \sigma^2_{\mathrm{rad}} \tag{3.20}$$

is the noncentrality parameter of the F-distribution under hypothesis H_2 and $n = N_{\text{rad}}$ is the number of radar samples.

3.6.3 Receiver Operating Characteristics

The probability distributions derived in the previous section can be used to determine the ROCs for both T_{c} and T_{p} detectors. The ROCs will be used to evaluate the potential performance gain due to the exploitation of AIS information. Denote

$$Q_F(y; n, m, \lambda) = \int_{\boldsymbol{y}}^{\infty} p_{F(n,m,\lambda)}(x)dx$$

as the complementary cumulative distribution function (CCDF) for the noncentral F-distribution, with n and m degrees of freedom, noncentrality parameter λ. Also define $Q_F^{-1}(p; n, m, \lambda)$ the CCDF inverse [VBR08]. The probability of detection (P_d) and the probability of false alarm (P_{fa}) of both (3.17) and (3.19) test statistics can be obtained as follows

Radar with AIS positions

$$P_{fa}(T_{\text{p}}) = Q_F(2\eta_{\text{p}}; 2, 2(n-k-1), 0) \tag{3.21}$$

$$P_d(T_{\text{p}}) = Q_F(2\eta_{\text{p}}; 2, 2(n-k-1), \lambda_{\text{p}}) \tag{3.22}$$

Radar only

$$P_{fa}(T_{\text{c}}) = Q_F(2\eta_{\text{c}}; 2(1), 2(n-1), 0) \tag{3.23}$$

$$P_d(T_{\text{c}}) = Q_F(2\eta_{\text{c}}; 2(1), 2(n-1), \lambda_{\text{c}}). \tag{3.24}$$

These results can be used to determine the theoretical ROCs of the detection problems, i.e.,

Radar with AIS positions

$$P_d(T_{\text{p}}) = Q_F(Q_F^{-1}(P_{fa}(T_{\text{p}}); 2, 2(n-k-1), 0); 2, 2(n-k-1), \lambda_{\text{p}}) \tag{3.25}$$

Radar only

$$P_d(T_c) = Q_F(Q_F^{-1}(P_{fa}(T_c); 2, 2(n-1), 0); 2, 2(n-1), \lambda_c) \tag{3.26}$$

Note that (3.25) and (3.26) indicate that the detection performance depends on the noncentrality parameters λ_p and λ_c, which are related to the signal-to-noise ratio after match filtering (SNRo). More precisely, for $\boldsymbol{\theta} \notin \boldsymbol{\theta}_{\text{AISprop}}$ and considering that the minimum distance between the test position $\boldsymbol{\theta}$ and the AIS positions $\boldsymbol{\theta}_{\text{AISprop}}$ is not lower than the radar resolution, we have SNRo $= \lambda_c \approx \lambda_p$ as $\|\boldsymbol{P}_A^{\perp}(\boldsymbol{\theta}_{\text{AIS}})\boldsymbol{a}(\boldsymbol{\theta})\| \approx \|\boldsymbol{a}(\boldsymbol{\theta})\|$.

3.7 Performance assessment

To evaluate the performance of both detectors T_p and T_c, we simulated a spatial SAR system operating with a $B = 15$ MHz bandwidth and transmitting $N = 81$ pulses of $W = 3.33\mu$s, leading to $BNW = 4050$ radar signal samples. Empirical ROCs were obtained using Monte Carlo trials for a fixed SNRo $= 10$ dB. We considered a scene defined as a 13×13 (for computational time reduction of the simulations) grid with a 10m resolution. The classical radar detector T_c and the proposed one T_p are compared for the detection of an unknown ship located in the center of the radar scene in the presence of cooperative ships. The two detectors are compared in two scenarios with different ship densities. Note that the cooperative ships were randomly positioned in the scene of interest. Simulated ROCs were obtained by using the results of 3.75×10^6 Monte Carlo trials corresponding to random configurations of ship positions and different noise realizations. The theoretical ROCs determined in (3.25) and (3.26) are also displayed for comparison. The ROCs of the different detectors considering the ship density are shown in Figure 3.1. Our conclusions about these results are summarized below

- Theoretical ROCs: The theoretical ROCs are represented in purple for the classical detector T_c and in black for the proposed detector T_p. These curves correspond to the optimal performance obtained at a given location of interest by using, respectively, radar data only and using radar data with the AIS position information. Note that the classical detector assumes the presence

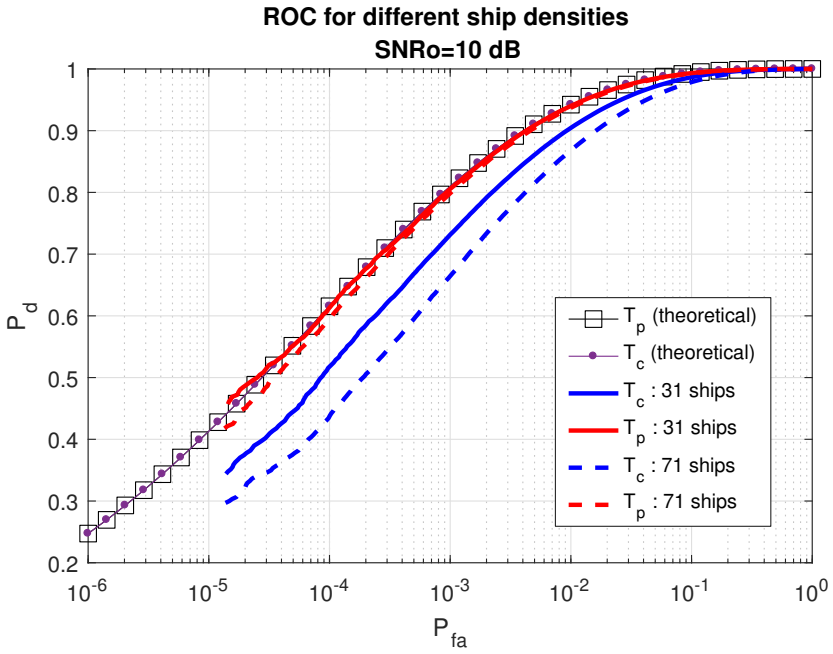

Figure 3.1: Theoretical and experimental detector performances using ROCs considering scenarios with different ship densities.

of a single ship in the scene of interest. As can be seen, the optimal performances obtained in this context for the two detectors are approximately the same.

- Empirical ROCs: The empirical ROCs are more realistic since the detection of ship at a given location will be affected by the presence of ships in the neighborhood. In order to illustrate this point, we have represented in Figure 3.1 the empirical ROCs computed by averaging the results of the different Monte Carlo runs (classical detector T_{c} in blue lines, proposed detector T_{p} in red lines, solid curves for 30 cooperative ships and dashed lines for a more dense scenario with 70 cooperative ships). First, we can observe that the detection performance decreases with the number of ships present in the scene. It can be explained by the fact that the probability of having interferences due to sidelobes of the processing scheme at a given location (affecting detection performance) is related to the number of ships present in its neighborhood. However, the performance degradation of the proposed detector T_{p} due to a higher density of ships in the

scene is much reduced when compared to the one obtained for the classical detector T_c. This is due to the fact that the proposed detector uses AIS data to remove the interferences from the known ships by projection the data in to the subspace orthogonal these known positions before to compute the matched filter. Another important remark is that the empirical ROCs associated with the proposed detector are closer to the optimal performance than the ones obtained for the detector T_c using radar data only.

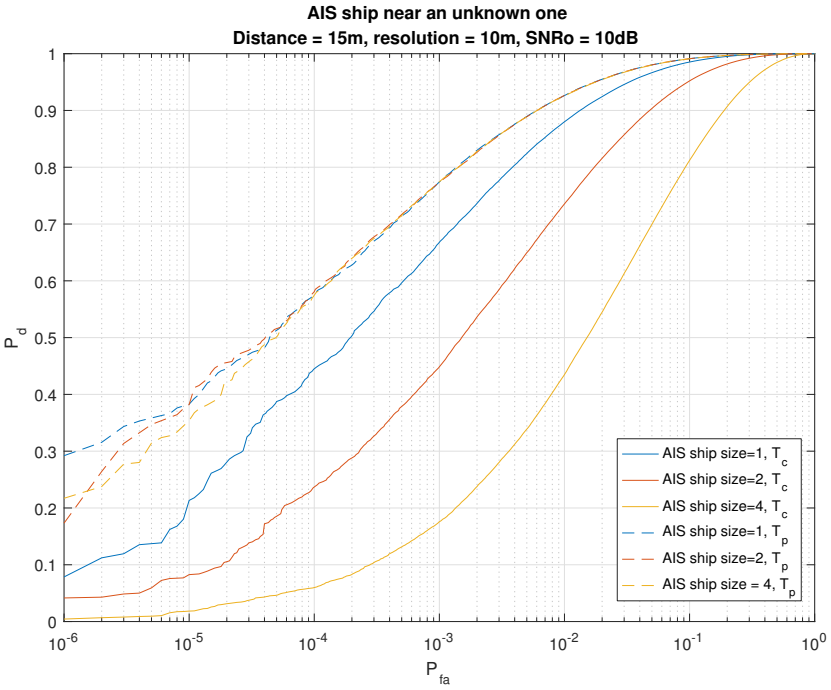

Figure 3.2: Experimental detector performance considering two ships: Different cooperative ship sizes. Distance = 15m, resolution = 10m.

We also propose to evaluate the detection performance of the ship detectors in a specific maritime scenario. Consider a cooperative ship which is at a close distance to an unknown ship. Ships are near but still separated by a distance bigger than the radar resolution. The detection performance of the conventional detector against the proposed one is evaluated using ROC simulations for different ship sizes and separation distances.

The ROCs of the different detectors considering a fixed distance of 15 meters is shown in Figure

3.2. The empirical ROCs are represented in two fashions: dashed lines for the proposed detector T_{p} and solid lines for the classical radar detector T_{c}. Colors discriminate three different sizes for the cooperative ship: blue indicates relative size equals to 1 (both have the same size), followed by red and yellow indicating respectively that the cooperative ship has twice and four times the size of the unknown ship to be detected. As can be seen, the performances obtained in this context for the two detectors are quite different. The classic detector performance in detecting the unknown ship is strongly affected by the other ship. As bigger is the cooperative ship size, more important is the impact in T_{c} detection performance. It may be observed that T_{p} is almost unchanged and preserves the performance close to its theoretical curve.

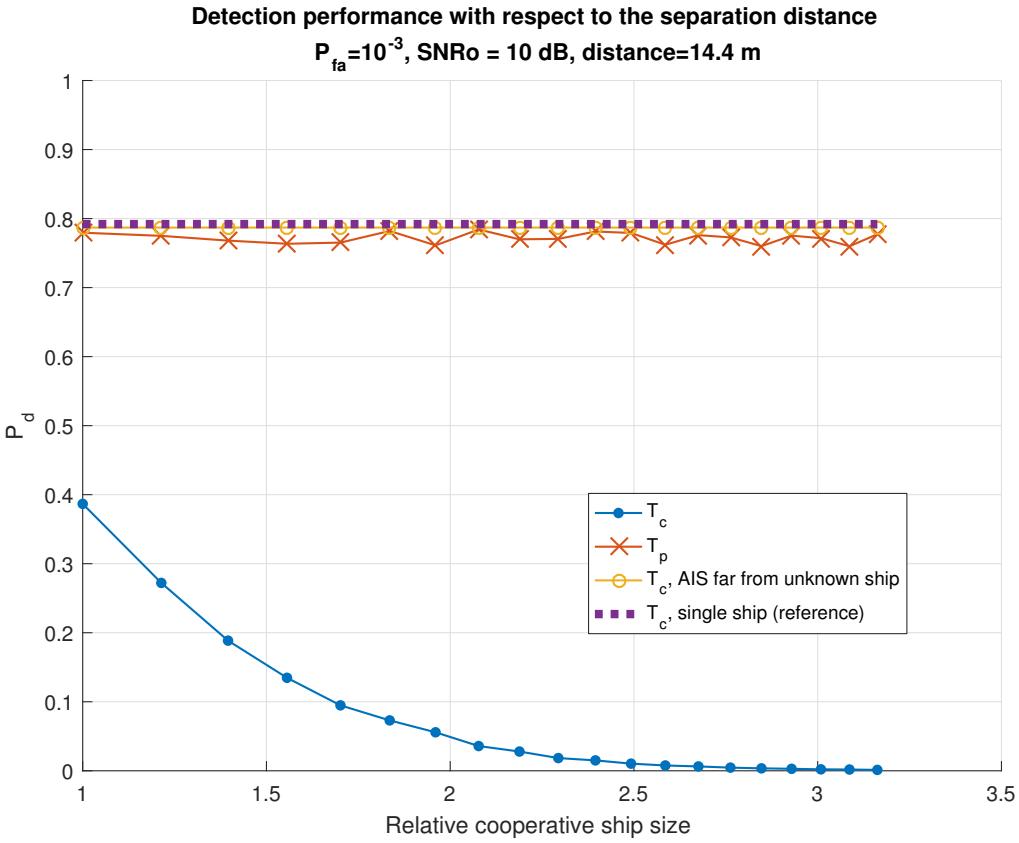

Figure 3.3: Experimental detector performance considering two ships: Different cooperative ship sizes. Distance = 14.4m, resolution = 10m.

Alternatively, those results may be observed in the Figure 3.3. Here we fixed the separation distance to a value that produces the most important impact in detection performance for the unknown ship (14.4 m separation in our test case). It may be observed that the classical radar detector looses performance as the size of the known ship increases (blue line with dots) while the proposed detector (red line with crosses) keeps the same performance of the classical detector in the single ship case (dotted violet line). The comparison with the classic detector in the case that both ships are far separated is show as reference (yellow line with circles).

In a second situation, consider now the fixed distance of 25 meters between the ships. It can be seen in the Figure 3.6 that the classic detector has better detection performance than the proposed one. The performance seems to increase when the size of the cooperative ship increases. Despite seeming beneficial at this situation this is actually a problem. The non uniform performance gain means that at certain situations the unknown ship may be or easily detected or not detected at all. The selection of a fixed detection threshold would not provide a constant false alarm rate in this kind of maritime scenario as desired.

Despite that we may still argue about the benefit may or may not surpass the loss in using the conventional detection in scenarios where one tries to detect unknown ships near known ones ships. To evaluate that we observe the Figure 3.7 that shows the impact in the detection performance with respect to the ship distance for a fixed value of P_{fa}.

First notice that we are interested in detecting ships that are farther than the radar resolution distance, so we consider only the positioning that are far than the radar resolution. In our simulations we considered a radar imaging with 10 m resolution. From the blue line representing the classical radar detector it can be seen that detection performance strongly depends on the distance between the ships. The proposed detector (here represented by the red line) has more stable performance almost identical to the theoretic curve (dotted line). For reference, when ships are far enough they approach the theoretical performance, which is close to the performance curve for the classic radar detector in a single ship case (when there is no interference from other ships). One may observe that both detectors have performance almost identical in the distances that represents the zeros of the radar lobes (multiples of the radar resolution distance) which indicates the source of the degradation

in T_c performance.

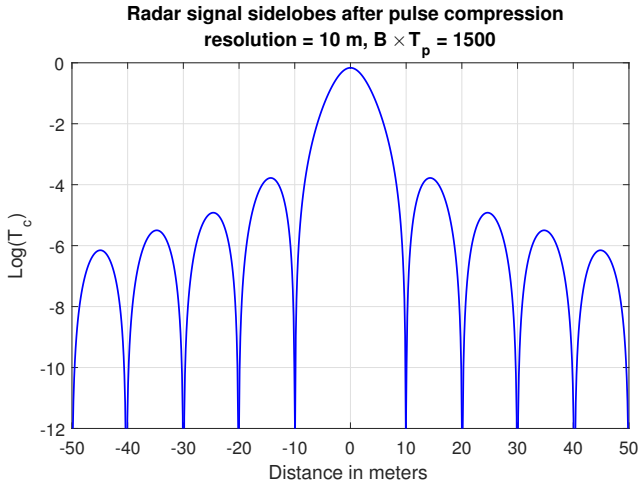

Figure 3.4: Representation of the radar signal lobes with respect to the distance between ships.

The radar resolution distance is defined by the widths in both range and cross-range axes of the main lobe of the radar signal pulse compressed (see Figures 3.4 and 3.5). After SAR processing, the radar return signal from a target at some coordinate pair $\boldsymbol{\theta}$ has most of its energy concentrated into the resolution cell respective to $\boldsymbol{\theta}$ coordinates. Though, a ratio of the radar energy spreads outside its resolution cell going into the side lobes. Because of that, radar scatters from other targets that are close but in different resolution cells may still suffer (and produce) constructive (or destructive) interference to neighbor resolution cells, impacting the performance. The proposed detector uses the projection of the known ships due to the AIS information to perform the "pre-whitening", meaning that the measurement vector has the interference (radar scatters from the ships that transmits their positions via AIS) removed before performing detection. This provides a detection map where noise is better estimated.

3.8 Case with important AIS errors

In this case we suppose that the AIS position list does not provide sufficient information about the target positioning. This may happens due to AIS positioning extrapolation errors or insufficient

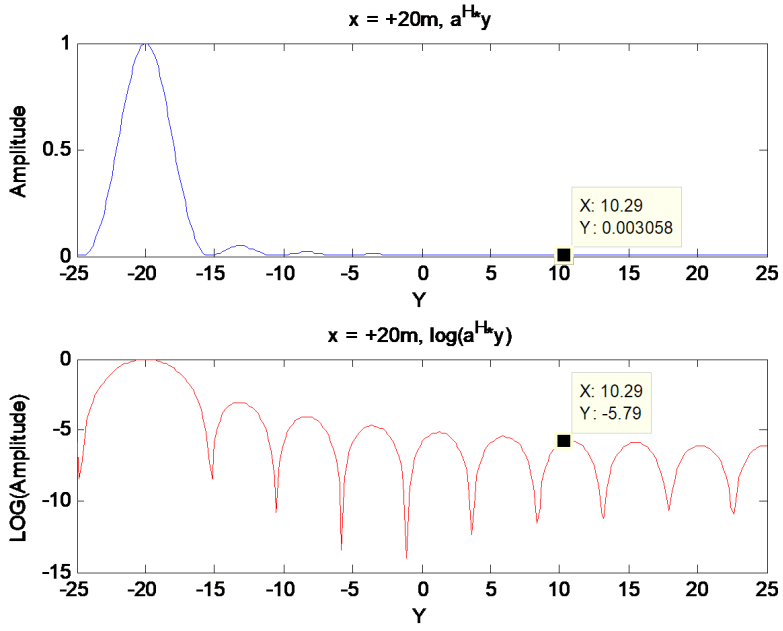

Figure 3.5: Representation of the radar signal lobes with respect to the distance between ships, compared to a radar detection cross section view.

precision of the GPS data, for example. One way to deal with the errors is to model the AIS positions as secondary data with noise modeled according to some probability distribution.

In this case, the signal model in (3.1) may be rewritten as

$$\begin{cases} \boldsymbol{y}_{\text{rad}} = \boldsymbol{A}\left(\boldsymbol{\theta}_r\right)\boldsymbol{\alpha} + \beta\boldsymbol{a}\left(\boldsymbol{\theta}\right) + \boldsymbol{n}_{\text{rad}} \\ \boldsymbol{\theta}_{\text{a}} = \boldsymbol{\theta}_r + \boldsymbol{n}_{\text{a}} \end{cases} \tag{3.27}$$

where $\boldsymbol{\theta}_{\text{a}}$ is the AIS positioning list, $\boldsymbol{\theta}_r$ is the vector containing the correct positions of the AIS ships at the radar measurement time, and $\boldsymbol{n}_{\text{AIS}}$ is the positioning error, here modeled as a Gaussian distribution with variance σ_{a}^2.

Once again, one must decide between both hypotheses H_2 and H_0 considering the existence (or not) of a radar signal in the test position $\boldsymbol{\theta}$. This can be translated into the GLRT by deciding if β

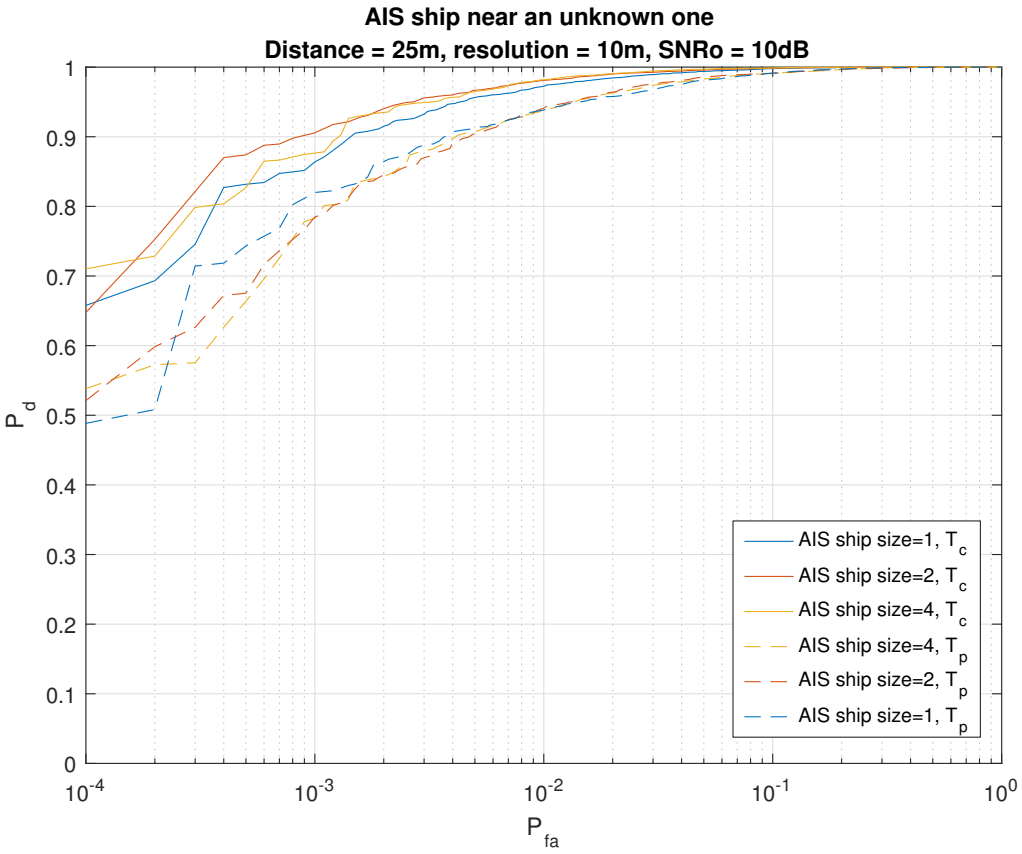

Figure 3.6: Experimental detector performance considering two ships: Different cooperative ship sizes. **Distance = 25m**, resolution = 10m.

is different from zero or not:

$$H_0 : \beta = 0 \text{ (absence of ship)} \tag{3.28}$$

$$H_2 : \beta \neq 0 \text{ (presence of ship).} \tag{3.29}$$

There are different possible cases considering the knowledge about the signal noise power and the noise power of the positioning measurement $\boldsymbol{\theta}_a$. The variance of the positioning error may be estimated using historical data from past AIS acquisitions. A formalization of the error model may be done considering the acquisition time, ship speed, signal propagation delay in order to produce a model about the position uncertainty of the AIS ships. Conversely, for the radar noise we may again

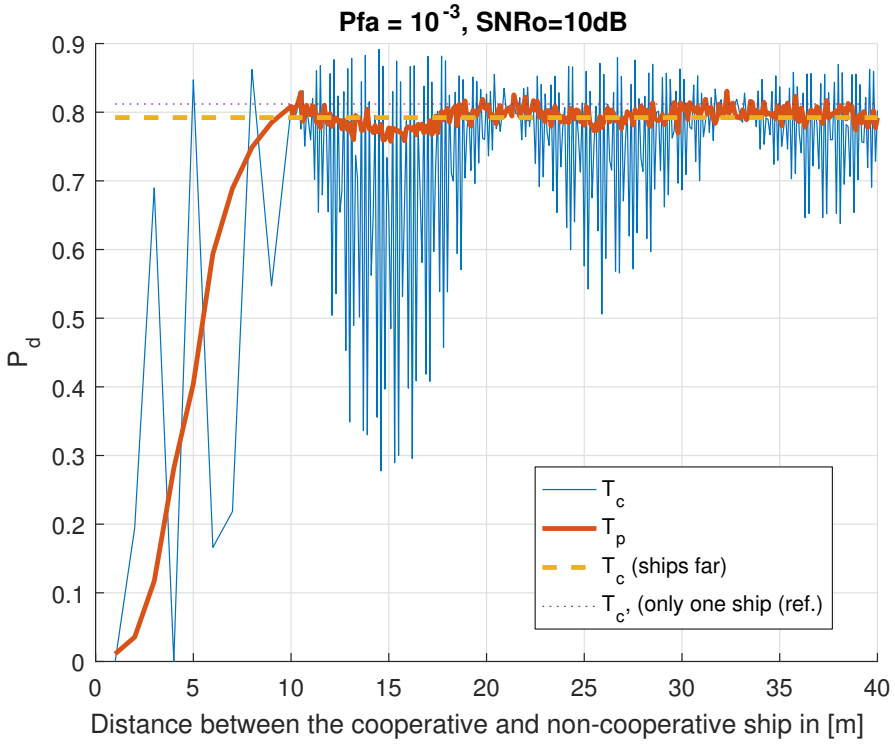

Figure 3.7: Experimental detector performance considering two ships: Comparison of P_d against the distance between the cooperative and an unknown ship. Resolution = 10m.

consider that both cases have known noise power. Alternatively, one could use secondary data to estimate the value of σ^2_{rad}, or again, consider that the noise power is unknown and must be estimated from the signal model.

Considering the case that σ_r^2 and σ_a^2 are known variances we have the following probability density functions

$$\begin{cases} p(\boldsymbol{y}_{\text{rad}}|\sigma_r^2, \boldsymbol{\alpha}, \beta, \boldsymbol{\theta}_r, \boldsymbol{\theta}) = (\pi\sigma_r^2)^{-N_{\text{rad}}} \exp\left\{-\frac{\|\boldsymbol{y}_{\text{rad}} - \boldsymbol{A}(\boldsymbol{\theta}_r)\boldsymbol{\alpha} - \beta\boldsymbol{a}(\boldsymbol{\theta})\|^2}{\sigma_r^2}\right\} \\ p(\boldsymbol{\theta}_{\text{a}}|\sigma_a^2, \boldsymbol{\theta}_r) = (2\pi\sigma_{\text{a}}^2)^{-N_{\text{AIS}}/2} \exp\left\{-\frac{\|\boldsymbol{\theta}_a - \boldsymbol{\theta}_r\|^2}{2\sigma_a^2}\right\}. \end{cases} \tag{3.30}$$

Being the additive noises $\boldsymbol{n}_r$ and $\boldsymbol{n}_a$ independent random variables, the joint probability density

function is given by the product

$$\begin{aligned} p(\boldsymbol{y}_{\text{rad}};\boldsymbol{\theta}_{\text{a}}|\sigma_r^2,\sigma_a^2,\boldsymbol{\alpha},\beta,\boldsymbol{\theta}_r,\boldsymbol{\theta}) &= p(\boldsymbol{y}_{\text{rad}}|\sigma_r^2,\boldsymbol{\alpha},\beta,\boldsymbol{\theta}_r,\boldsymbol{\theta}) \times p(\boldsymbol{\theta}_{\text{a}}|\sigma_a^2,\boldsymbol{\theta}_r) \\ &= k\exp\left\{-\frac{\|\boldsymbol{y}_{\text{rad}}-\boldsymbol{A}(\boldsymbol{\theta}_r)\boldsymbol{\alpha}-\beta\boldsymbol{a}(\boldsymbol{\theta})\|^2}{\sigma_r^2}-\frac{\|\boldsymbol{\theta}_a-\boldsymbol{\theta}_r\|^2}{2\sigma_a^2}\right\}. \end{aligned} \tag{3.31}$$

where $k=\left(\pi\sigma_r^2\right)^{-N_{\text{rad}}}\left(2\pi\sigma_a^2\right)^{-N_{\text{AIS}}/2}$ is a constant. Considering both hypotheses H_2 and H_0 one may replace the unknown variables by their MLE considering each hypothesis as

$$p(\boldsymbol{y}_{\text{rad}}|\sigma_r^2,\sigma_a^2,\widehat{\boldsymbol{\alpha}}_i,\beta_i,\widehat{\boldsymbol{\theta}_{ri}},\boldsymbol{\theta},H_i)=k\exp\left\{-\frac{\|\boldsymbol{w}_i\|^2}{\sigma_r^2}-\frac{\|\boldsymbol{\theta}_a-\boldsymbol{\theta}_r\|^2}{2\sigma_a^2}\right\}, \tag{3.32}$$

where $\boldsymbol{w}_i=\|\boldsymbol{y}_{\text{rad}}-\boldsymbol{A}(\widehat{\boldsymbol{\theta}_{r1}})\widehat{\boldsymbol{\alpha}}_1-\hat{\beta}\boldsymbol{a}\|^2$ for $i=2$ and $\boldsymbol{w}_i=\|\boldsymbol{y}_{\text{rad}}-\boldsymbol{A}(\widehat{\boldsymbol{\theta}_{r0}})\widehat{\boldsymbol{\alpha}}_0\|^2$ for $i=0$, and $i\in\{0,2\}$ represents the index of the corresponding hypothesis H_0 or H_2. The GLRT is

$$T=\frac{p(\boldsymbol{y}_{\text{rad}};\boldsymbol{\theta}_{\text{a}}|\sigma_r^2,\sigma_a^2,\hat{\boldsymbol{\alpha}}_1,\hat{\beta}_1,\boldsymbol{\theta}_r,\boldsymbol{\theta},H_2)}{p(\boldsymbol{y}_{\text{rad}};\boldsymbol{\theta}_a|\sigma_r^2,\sigma_a^2,\hat{\boldsymbol{\alpha}}_0,\beta=0,\boldsymbol{\theta}_r,\boldsymbol{\theta},H_0)}. \tag{3.33}$$

Taking the logarithm we obtain the following formulation for the detector

$$T'=\frac{\|\boldsymbol{y}_{\text{rad}}-\boldsymbol{A}(\widehat{\boldsymbol{\theta}_{r0}})\widehat{\boldsymbol{\alpha}}_0\|^2-\|\boldsymbol{y}_{\text{rad}}-\boldsymbol{A}(\widehat{\boldsymbol{\theta}_{r1}})\widehat{\boldsymbol{\alpha}}_1-\hat{\beta}\boldsymbol{a}(\boldsymbol{\theta})\|^2}{\sigma_r^2}+\frac{\|\boldsymbol{\theta}_a-\widehat{\boldsymbol{\theta}_{r0}}\|^2-\|\boldsymbol{\theta}_a-\widehat{\boldsymbol{\theta}_{r1}}\|^2}{2\sigma_a^2}. \tag{3.34}$$

Considering the hypothesis H_0, it is clear that the MLE of the unknown variables $\boldsymbol{\alpha_0}$ and $\boldsymbol{\theta}_{r0}$ are

$$\begin{cases} \widehat{\boldsymbol{\alpha}}_0=(\boldsymbol{A}^H\boldsymbol{A})^{-1}\boldsymbol{A}^H\boldsymbol{y}_{\text{rad}}=\boldsymbol{A}^+(\widehat{\boldsymbol{\theta}_{r0}})\boldsymbol{y}_{\text{rad}} \\ \widehat{\boldsymbol{\theta}_{r0}}=\arg\min\limits_{\boldsymbol{\theta}_{r0}}\left(\frac{\boldsymbol{y}_{\text{rad}}^H\boldsymbol{P_A}^{\perp}(\boldsymbol{\theta}_{r0})\boldsymbol{y}_{\text{rad}}}{\sigma_r^2}+\frac{\|\boldsymbol{\theta}_a-\boldsymbol{\theta}_{r0}\|^2}{2\sigma_a^2}\right) \end{cases} \tag{3.35}$$

where $\boldsymbol{A}^+$ denotes the pseudo-inverse of the matrix $\boldsymbol{A}$. The AIS position list $\boldsymbol{\theta}_r$ has errors and need to be estimated. For hypothesis H_2

$$\begin{cases} \widehat{\boldsymbol{\alpha}}_1=(\boldsymbol{A}^H\boldsymbol{A})^{-1}\boldsymbol{A}^H\boldsymbol{y}_{\text{rad}}=\boldsymbol{A}^+(\widehat{\boldsymbol{\theta}_{r0}})\left(\boldsymbol{y}_{\text{rad}}-\beta\boldsymbol{a}(\boldsymbol{\theta})\right) \\ \hat{\beta}=\acute{\boldsymbol{a}}^H\left(\acute{\boldsymbol{a}}^H\acute{\boldsymbol{a}}\right)^{-1}\acute{\boldsymbol{y}} \\ \widehat{\boldsymbol{\theta}_{r1}}=\arg\min\limits_{\boldsymbol{\theta}_{r1}}\left(\frac{\boldsymbol{y}_{\text{rad}}^H\boldsymbol{P_A}^{\perp}(\boldsymbol{\theta}_{r1})\boldsymbol{y}_{\text{rad}}}{\sigma_r^2}-\frac{1}{\sigma_r^2}\frac{\boldsymbol{y}_{\text{rad}}^H\boldsymbol{P_A}^{\perp}(\boldsymbol{\theta}_{r1})\boldsymbol{a}\boldsymbol{a}^H\boldsymbol{P_A}^{\perp}(\boldsymbol{\theta}_{r1})\boldsymbol{y}_{\text{rad}}}{\boldsymbol{a}^H\boldsymbol{P_A}^{\perp}(\boldsymbol{\theta}_{r1})\boldsymbol{a}}+\frac{\|\boldsymbol{\theta}_a-\boldsymbol{\theta}_{r1}\|^2}{2\sigma_a^2}\right) \end{cases} \tag{3.36}$$

where $\acute{\boldsymbol{a}}=\boldsymbol{P_A}^{\perp}\boldsymbol{a}$ and $\acute{\boldsymbol{y}}=\boldsymbol{P_A}^{\perp}\boldsymbol{y}_{\text{rad}}$ and the orthogonal projector $\boldsymbol{P_A}^{\perp}$ defined for $\boldsymbol{A}(\boldsymbol{\theta}_{r1})$.

The detector is then

$$T' = \frac{\boldsymbol{y}_{\text{rad}}^H \boldsymbol{P_A}^{\perp}(\widehat{\boldsymbol{\theta}_{r0}})\boldsymbol{y}_{\text{rad}}}{\sigma_r^2} - \frac{1}{\sigma_r^2}\frac{\boldsymbol{y}_{\text{rad}}^H \boldsymbol{P_A}^{\perp}(\widehat{\boldsymbol{\theta}_{r1}})\boldsymbol{a}\boldsymbol{a}^H \boldsymbol{P_A}^{\perp}(\widehat{\boldsymbol{\theta}_{r1}})\boldsymbol{y}_{\text{rad}}}{\boldsymbol{a}^H \boldsymbol{P_A}^{\perp}(\widehat{\boldsymbol{\theta}_{r1}})\boldsymbol{a}} + \frac{\|\boldsymbol{\theta}_a - \widehat{\boldsymbol{\theta}_{r0}}\|^2 - \|\boldsymbol{\theta}_a - \widehat{\boldsymbol{\theta}_{r1}}\|^2}{2\sigma_a^2}. \tag{3.37}$$

3.8.1 Simulations

Here we demonstrate with simulated data the detector when there are important errors bigger than the radar resolution. In this case, the detector must determine the position $\boldsymbol{\theta}_r$ that minimizes the cost function related to choosing a position $\boldsymbol{\theta}_r$ that is different from $\boldsymbol{\theta}_a$ measured (which means acquired by the AIS). We simulated a scenario which two ships are close but still separated by a distance bigger than the radar resolution. One of the ships is cooperative and the other is present for reference. The radar target positions are (+3,0) meters and (+2,+2) meters from the target area center.

It can be seem that in 3.8 that the detector that admits small errors in the AIS positions could not remove the radar detection of the known ship at (2,2) as the positioning error is greater than the radar resolution. The detector identifies a detection at the correct ship position but as the position is not considered in the AIS list the detector identifies the coordinates as a unknown ship. With the detector that models AIS errors greater than the radar resolution we searched for the best $\boldsymbol{\theta}_r$ that minimizes the cost functions. As the estimated value for theta identified that (2,2) best matches the real AIS position, the detector now considers the target at (2,2) as the real AIS position and removes the signature by projecting the measurements to the orthogonal of $\boldsymbol{A}$.

The detection map presented at Figure 3.9 shows that the target that before was present at the coordinates (2,2) is now removed and only the unknown ship at (3,0) is presented as a new detection.

3.9 Conclusions

Here we addressed the problem of detecting a ship at a given location in the presence of cooperative ships potentially present in its neighborhood. We demonstrated the interest of using the knowledge of cooperative ship positions with raw radar data. Considering that the list of ships detected by

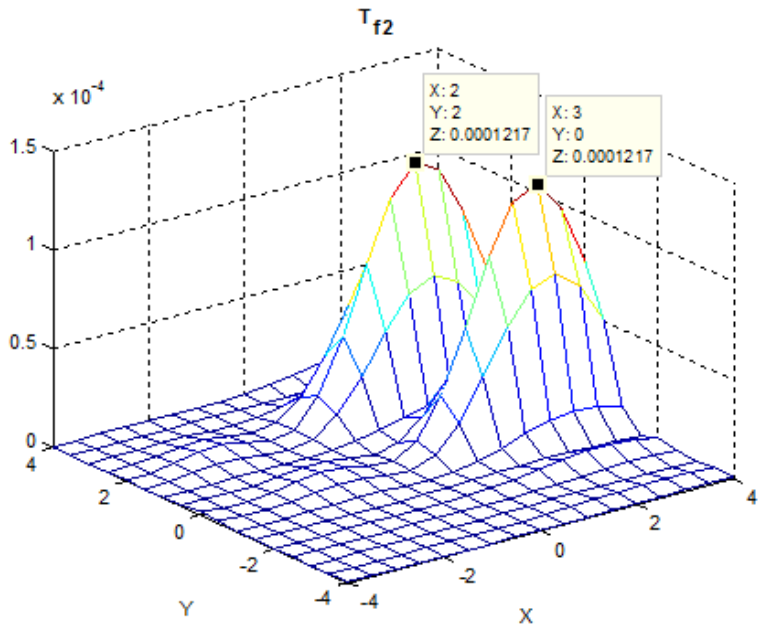

Figure 3.8: Detector considering positioning errors **smaller** than the radar resolution. The AIS position is the pair of coordinates (0,0) (azimuth;range), while the real AIS is at (2,2). The reference is an unknown ship at (3,0). SNRo=11 dB, $\sigma_a^2 = 2.82$, radar targets at (+3,0) and (+2,+2), resolution is (2m;5m) meters.

the AIS can be incomplete or corrupted, we proposed a two-step procedure: 1) validation of AIS detections, and 2) detection of unknown ships. The results obtained in this study showed that the classical detector performance decreases when the number of ships in the scene increases. However, the proposed detector using the AIS data is much less affected by the number of cooperative ships present in the scene. The advantage of the proposed method is that it provides improved radar detection in dense environments. Also, it produces a detection map that considers both radar and AIS sources to discriminate between the four hypotheses. One possible application of this detector is ship detection in high density scenes considering that most ships cooperatively transmits their positions using the AIS. Other uses may consider the elimination of known returns that are not exclusively ship (for example the coastal area). We evaluated the impact of other ships in specific scenario considering two ships that are close distance and provide an explanation to the effect of the

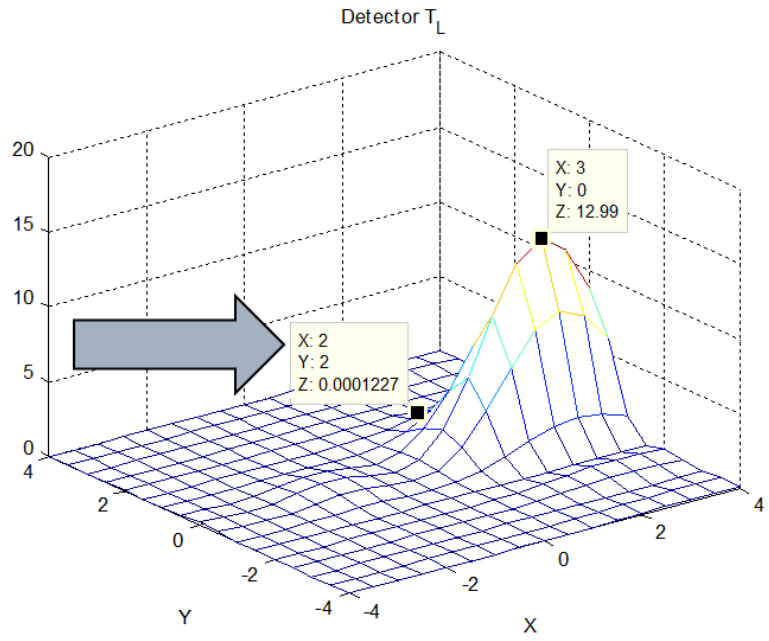

Figure 3.9: Detector considering positioning errors **bigger** than the radar resolution. The AIS position is the pair of coordinates (0,0) (azimuth;range), while the real AIS is at (2,2). The reference is an unknown ship at (3,0). SNRo=11 dB, $\sigma_a^2 = 2.82$, radar targets at (+3,0) and (+2,+2), resolution is (2m;5m).

interference in the detection performance from when more than one ship is present. Building new detectors mitigating the impact of positioning errors in the AIS is also an interesting problem that would deserve to be investigated and will be presented in the next Section.

In the next chapter we will present the simulations of the radar and AIS signals and applications of the detectors presented so far. We also present the detection maps produced with the detectors considering some scenarios that are pertinent to maritime surveillance (high density scenario and detection of ships that are close distance, for example). With the simulations we are going to discuss the challenges considering the detection methods presented so far.

Chapter 4

Fusion of AIS and radar data for specific surveillance applications

4.1 Introduction

Here we describe the simulation method used for generating the raw sensor signals and by specifying the key parameters used in these simulations. Also, we propose some maritime surveillance problems to be addressed using the detection methods discussed so far. Our objective is to show the radar signal simulation and that the fusion of data from dissimilar sensors can be applied to specific maritime surveillance applications.

This chapter is organized as follows. In the first section we introduce the simulation method that we have been used for AIS and radar data and the simulation parameters. We then introduce some test scenarios where we explore three surveillance examples. In these examples, ship targets

are presented in different scenarios. The radar signal simulator will produce the radar signals that will be used by the detectors to produce a detection map of the scenarios presented in this chapter. The simulation results are analyzed carefully and some conclusions are finally provided.

4.2 Radar signal simulator

In the first chapter, we presented a mathematical model for raw radar signals obtained from targets positioned at Earth's surface (specifically the seas) being illuminated by a radar embedded satellite. Consider that the imaging of a maritime scene with ships is done by a signal simulator based on the same model. Consider also the radar operating as focused SAR in "stripmap" mode, positioned broadside in a side-looking configuration, that is, the radar beam is normal to the flight direction continuously observing a swath parallel to the satellite flight path on Earth's surface (see the SAR geometry in Figure 1.11).

With those considerations, we proceed detailing the steps to simulate the surveillance scenarios. We use the raw radar signals produced by our radar signal simulator, and the signals will be processed by the ship detectors to produce a detection map. The block diagram in Figure 4.1 indicates how the radar raw signal simulator is used to reproduce a radar signal $\boldsymbol{a}(\boldsymbol{\theta})$ and a radar measurement $\boldsymbol{y}_{\text{rad}}$.

With the radar signal simulator, a radar signal $\boldsymbol{a}(\boldsymbol{\theta})$ is modeled considering a target at some position $\boldsymbol{\theta}$ for a specific configuration of the radar (given by the set of SAR parameters). The radar measurement $\boldsymbol{y}_{\text{rad}}$ contains the radar raw signals from the targets in the radar view, added with noise $\boldsymbol{n}_{\text{rad}}$. The columns of matrix $\boldsymbol{A}(\boldsymbol{\theta}_{\text{all}})$ are composed of the radar signals $\boldsymbol{a}(\boldsymbol{\theta}_i)$ from the illuminated ships in the area of interest ($\boldsymbol{\theta}_i \in \boldsymbol{\theta}_{\text{all}}$, the position list containing all radar illuminated ships), and $\boldsymbol{\alpha}$ is the vector containing the amplitude of each signal in $\boldsymbol{A}(\boldsymbol{\theta}_{\text{all}})$. Finally, the noise $\boldsymbol{n}_{\text{rad}}$ is modeled as in (2.4).

The Figure 4.1, we illustrate the process of building a detection map using the classical radar detector and the synthetic signals from our simulator. This detector uses as input the signal modeled $\boldsymbol{a}(\boldsymbol{\theta})$ and the measurement vector $\boldsymbol{y}_{\text{rad}}$. The detector output is compared to a threshold to produce a binary output indicating if a ship is detected (or not) at the position under test $\boldsymbol{\theta}$. We produce

the detection map by repeating this process for the test positions covering the area of interest.

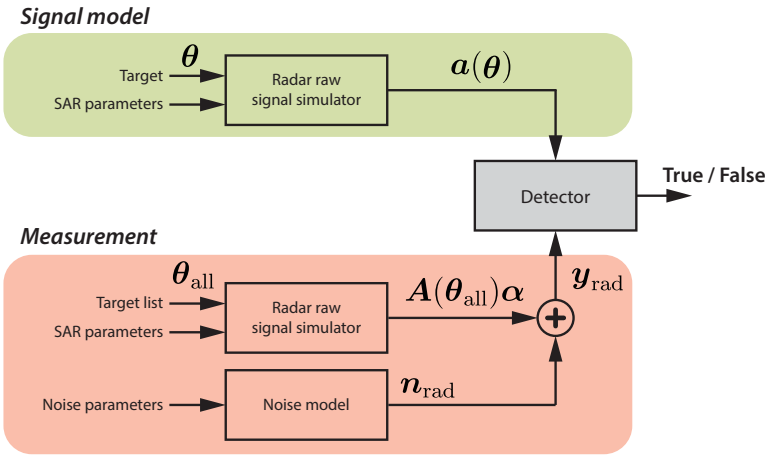

Figure 4.1: The block diagram for detecting targets using the classical radar detector.

4.2.1 Simulator parameters

The simulator have parameters for both the target and radar sensor. Target parameters include the positioning information $\boldsymbol{\theta} = (x, y)^T$ in the form of a pair of coordinates and the reference amplitude α for each respective return signal. Radar parameters consist in information about the radar and the scene geometry (see Figure 1.11), e.g., the antenna dimensions, radar speed and direction, altitude, incidence angle, among others. The SAR signal process parameters are defined according to a desired performance, e.g., the carrier frequency, radar signal bandwidth, PRF, radar resolution, coverage, wave penetration, the SNR, signal processing gain, among others.

The choice of simulation parameters has compromises in many aspects. For example, the choice of radar carrier frequency influence other factors like the resolution, power, coherence requirements, propagation factors (related to radar penetration like weather), stealth or low probability of intercept in military application [CGM95]. Here we simply consider the radar operating in the X-band and resolution in tens of meters.

The satellite velocity in the simulator is derived considering orbit information using the *vis-viva-equations* [See03], where speed at any point of the orbit is given by $v = \sqrt{GM(\frac{2}{r} - \frac{1}{a_s})}$, which a_s is the length of the semi-major axis of the satellite orbit, r is the distance between orbiting bodies, namely the satellite and Earth's gravity center, and GM the standard gravitational parameter, which for the Earth is $GM = 3.98600 \times 10^{14} m^3/s^2$.

Some simulation parameters used in the simulations are presented on the parameter Tables 4.1 and 4.2.

Table 4.1: SAR simulation input parameters

Parameter	**Value**	**Description**
h	500 km	Altitude
f_c	9.5 GHz	Carrier frequency
L_a	20 m	Azimuth antenna length
δx	10 m	Azimuth resolution
γ	25°	Antenna look angle
B_0T	50	Time-bandwidth product
f_s	$1.2B_0$ Hz	Sampling rate
PRF	$1.2B_D$ Hz	Pulse repetition frequency

Table 4.2: SAR simulation calculated parameters

Parameter	**Value**	**Description**
V_{st}	7612.6 m/s	Platform speed
L	$\lambda R_c/L_a$ m	Synthetic aperture length
B_D	$V_{st}/\delta x$ Hz	Minimum PRF (azimuth unambiguous)
PRF_{max}	$c/(2\Delta R)$ Hz	Maximum PRF

Notes: c denotes the speed of light and λ the radar wavelength.

4.2.2 The radar detection map using the signal simulator

Consider the example scenario in Figure 4.2. The radar signal returns are modeled considering the acquisition of a serie of pulses gathered in timed intervals restrained to a certain observation window (the area of interest). The measurement $\boldsymbol{y}_{\text{rad}}$ contains all samples obtained from the illuminated targets in the area. Yet, the antenna aperture limits the practical amount of samples that SAR integration process is effective in the azimuth direction x, that is, which may be integrated by the detector when testing a single position $\boldsymbol{\theta}$. In range, it is the pulse duration and the vertical aperture of the antenna that limits the number of samples in the range direction. This way, the antenna aperture sizes, the pulse duration T, the PRF f_p and the sampling rate f_s are the parameters that define the quantity of effective signal samples in the SAR processing. This limitation in the number of processed samples can be observed using an example of the raw radar signal with our simulator.

In Figure 4.3a we observe the return signal from a single target at coordinates (0,0) meters. As it may be seen, the signal returns are spread in the range direction and azimuth where the signal is clearly limited to an area of near 60 samples in range by 90 samples in azimuth.

due to the pulse width T and the antenna real aperture size in azimuth.

The Figures 4.3a and 4.3b show the raw radar signals for targets located at different coordinates (for reference plots indicate the real part of complex signals). In Figure 4.3a is presented the raw radar signal for a target at (0,0) meters. We consider the coordinates with respect to the radar scene illustrated in 4.2. The Figure 4.3b is the measurement of a scene with two targets: one at (0,0) meters and other at (200,200) meters. Observe that the raw signals does overlap when targets are separated by less than the size of the antenna aperture in azimuth direction, or by less than $cT/2$ meters in the range direction. Targets that are closer than this distance overlaps causing some interference. It is the SAR processing that will resolve overlapping targets from the measurement signal $\boldsymbol{y}_{\text{rad}}$. In Figure 4.4 we observe the chirp from the radar raw signal. The fast time samples in the range direction and the slow time samples in the azimuth direction. The fast time signal obtained by sampling the chirp echo, while chirp waveform observed in the slow time samples is result from the inter-pulse phase rotation of the coherent signal (caused by the target distance variation between each radar pulse).

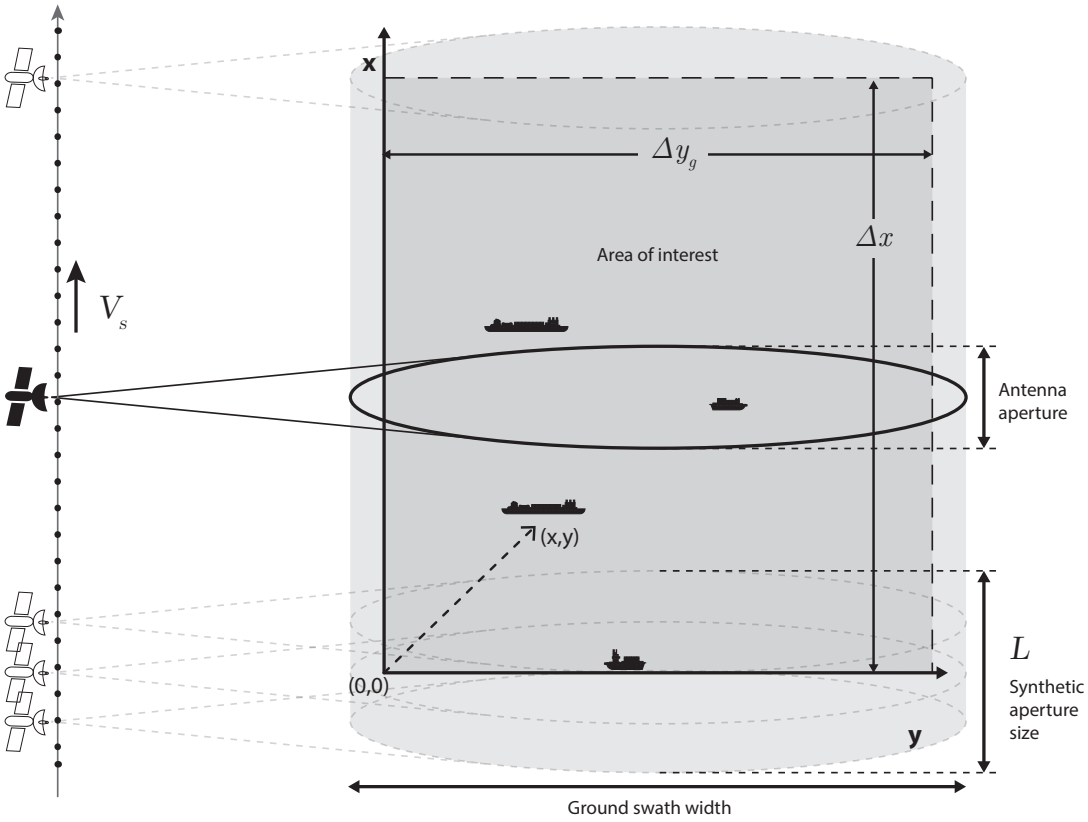

Figure 4.2: Geometry of a radar stripmap scene.

4.2.3 Simulation considerations

The radar signals are represented as bi-dimensional maps representing range versus Doppler coordinates. The relative displacement of the radar with respect to a target enables the cross range position discrimination. However, there is an extra Doppler with non-stationary targets that must be compensated in order to correctly position target objects. One can estimate the correct ship position for each ship in a scene or compensate using external information. For the sake of simplicity, we consider that the targets are stationary during the radar imaging.

About the radar signal power, we consider that the received radar signal attenuation due to propagation is uniform in the swath. The antenna aperture is considered ideal, meaning that target amplitude has unitary gain inside the antenna aperture while those outside are not considered.

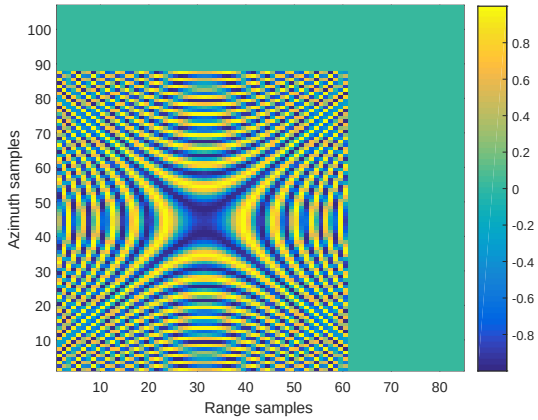

(a) Radar raw signal from a single target at (0,0) m.

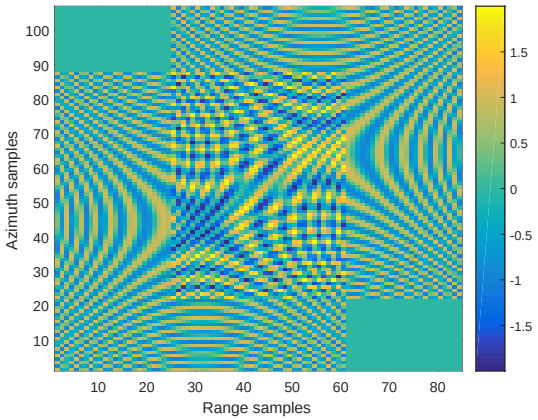

(b) Radar raw signal for two targets: One at (0,0) meters and the other at (200,200) meters.

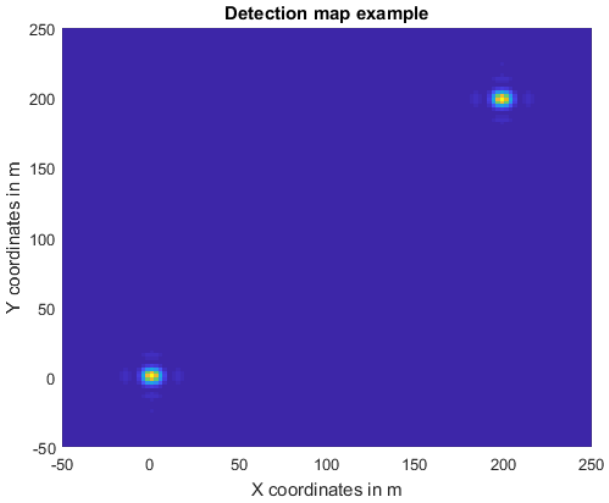

(c) Radar detection map example for the scene containing two targets before applying a detection threshold.

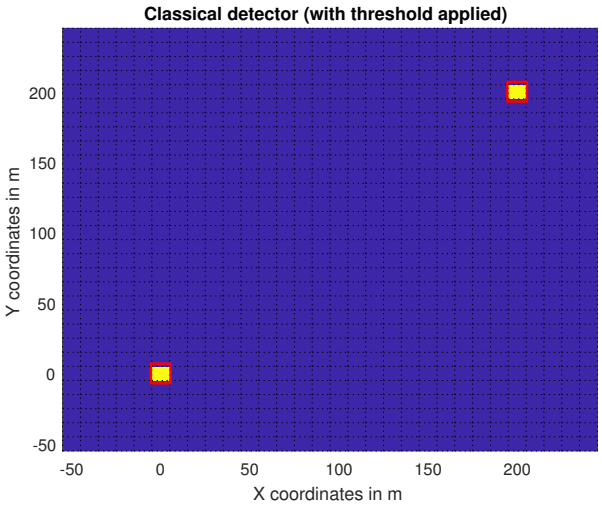

(d) Detection map after applying a detection threshold.

Figure 4.3: Example of radar raw signals that are generated by the signal simulator and their detection maps.

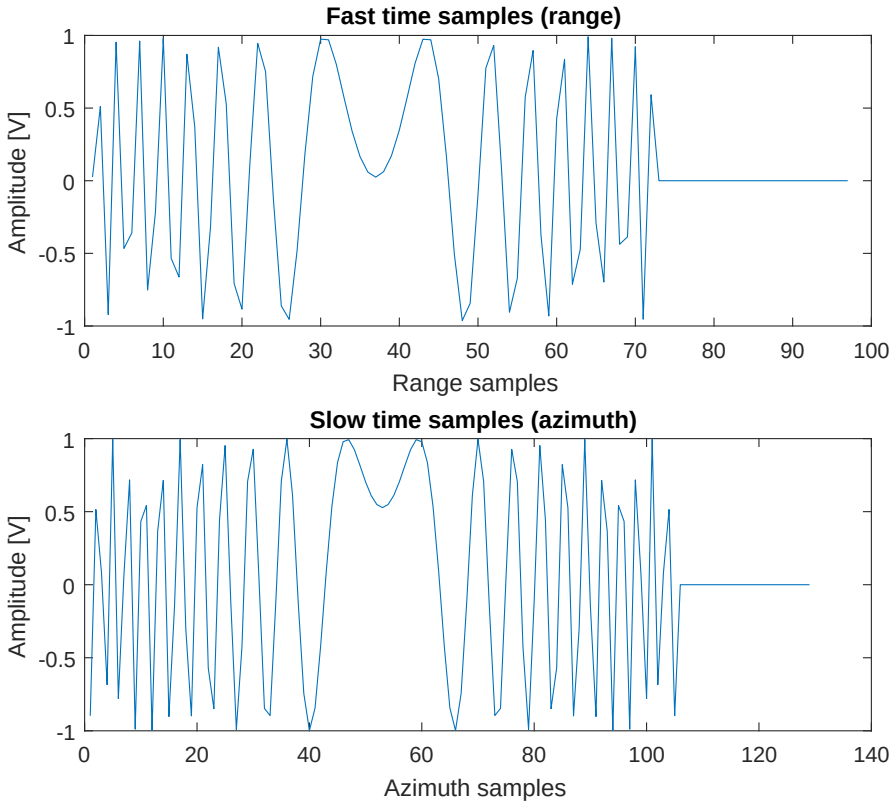

Figure 4.4: Example of radar signal observed in both fast time and slow time samples (respectively range and azimuth direction).

4.3 Surveillance test scenarios

In broad sense, a surveillance system needs to deal with the different events that are particularly interesting with respect to maritime safety and security. So far we presented ways to improve detection by integrating AIS and radar sensor data. In order to observe how using ship detection and classification may improve maritime surveillance we reproduce some typical scenarios. Specifically, we present a piracy activity, an uncontrolled sea cargo transshipment and also an example of high ship traffic scene based on a real situation. We begin introducing each surveillance scenario and exploring the scenes with our simulations.

4.4 Piracy: the ship hijacking case

Here we represent a classical piracy example of a ship hijacking case. In this scenario, criminals boarding a pirate ship moves from the coastal region approaching a commercial maritime route with the objective to hijack a possible victim, in our case a cargo ship. This is illustrated in the figure 4.5. The case is represented in a sequence of four events shown in the figure. The colored arrows represent the displacement of ships from the color of the arrow. The identification markers (crosses, plus signs, circles) represent a snapshot of the ship positions at some time instant, the parenthesis indicate the start and the end time in hours of each vessels in the chain of events in the ship hijacking case.

The first event occurs in figure 4.5a, where one pirate ship represented by the green circles sets course from the coast at the coordinates (0, 42) kilometers to the direction of a maritime route (green arrow), when 5.1 hours later a cargo ship appears, here represented by the blue “x”.

The second event is illustrated in figure 4.5b, the pirate ship (pirate 1) continues to approach the cargo ship, stopping at hour 8.4 and releasing a smaller vessel (pirate 2) represented by the orange crosses.

The third event is illustrated in figure 4.5c. The pirate 1 here stands still for near half an hour while the pirate 2 goes fast to the cargo ship to seize the victim. The figure 4.5d shows the last event when both cargo and the pirate 2 moves in the direction of the main ship (pirate 1), and all

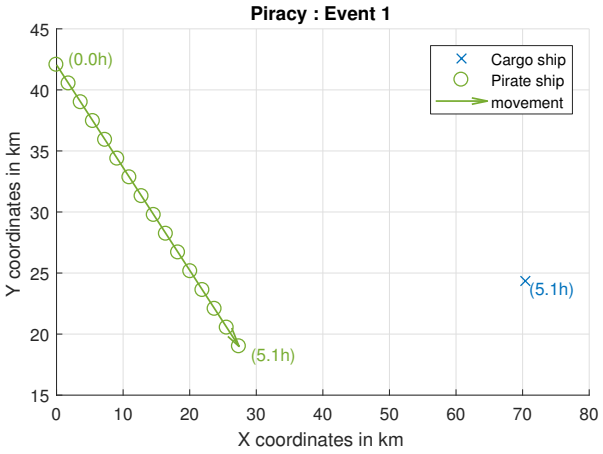

(a) A pirate ship approaches the cargo route looking for a victim.

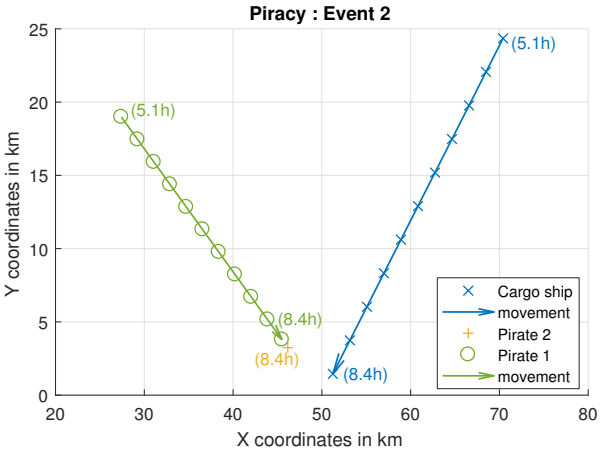

(b) The pirate ship approaches the cargo vessel and releases a second smaller pirate ship.

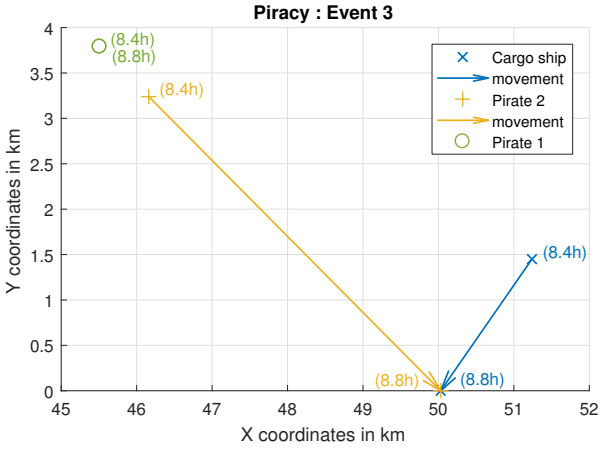

(c) The second pirate ship seizes the cargo vessel and hijacks the control of the ship in near half an hour.

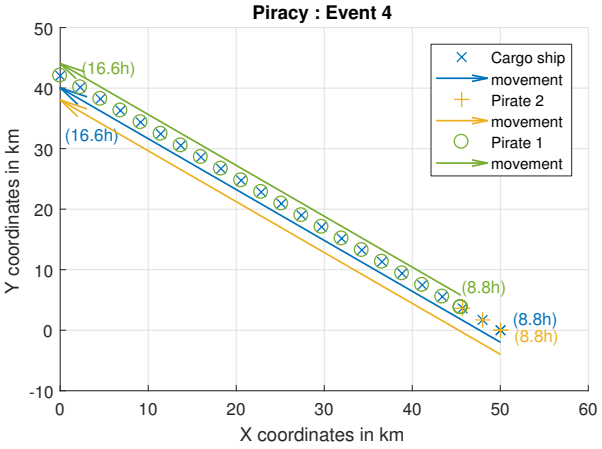

(d) Pirates travel back to the coast while controlling the cargo ship. The hijack is complete.

Figure 4.5: Piracy in a ship hijacking case divided in four chronological events.

three ships then travel back to the coast to the original position where the pirates came from. The hijacking now is complete with the total scenario, taking nearly 17 hours.

4.4.1 Piracy scenario simulation

In order to reproduce the surveillance situation we process snapshots of the scene as it would be seen by a satellite embedding a radar that passes over the scene. For sake of simplicity, we consider only imaging snapshots of some events that are more relevant to perform detection.

In the Figure 4.6 we observe the radar map of the scene at the instant of the third event, when both pirate vessels are on the scene and the smaller ship set course to seize the cargo vessel. To be more realistic, we assume the following sizes for the vessels: The cargo ship has 150 meters length and beam (ship width over the water) of 25 meters, the first pirate ship is 30x10 meters and the second pirate boat is about 10x10 meters wide. A intensity map of this scene is observable in the figure 4.7. This map has no measurement noise for illustration purposes. Data is displayed in a mesh plot where the peaks represent raw output of the classical detector before applying a detection threshold. The detectors are used to test a grid at the surveillance scene and the result for each position corresponds to a point in the grid. The radar parameters used in the simulations are indicated in the Table 4.3 and 4.4.

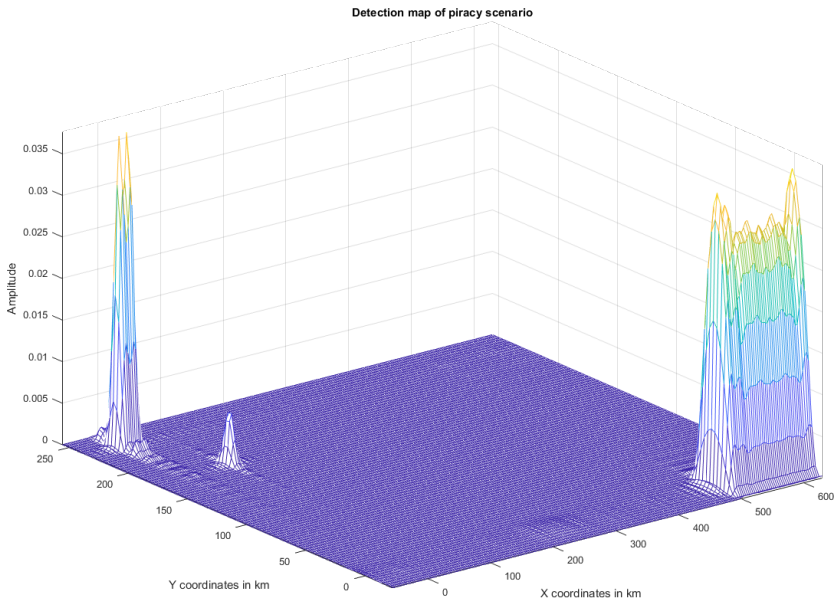

Figure 4.6: Radar map of the piracy scene : The pirate 1 at the upper left corner, pirate 2 is the small peak near the pirate 1, and the cargo ship at the lower right corner.

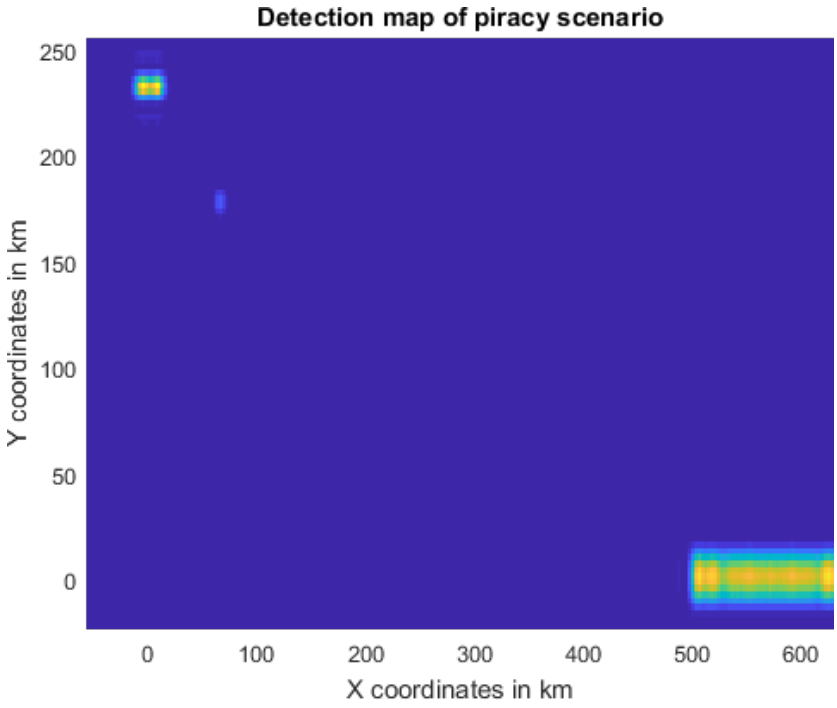

Figure 4.7: Piracy in a ship hijacking case. Using the classic detector. Scene of a pirate ship (upper left corner) releasing a second pirate ship at coordinates (80,180) km, heading for the cargo vessel (lower right corner).

Table 4.3: SAR input parameters for simulation

Parameter	**Value**	**Description**
h	500 km	Altitude
f_c	9.5 GHz	Carrier frequency
δx	10 m	Azimuth resolution
δx	10 m	Range resolution
γ	25°	Antenna look angle
B_0T	50	Time-bandwidth product
Δx	15 km	Range length of target area
Δy	200 m	Azimuth length of target area
f_s	$1.2B_0$ Hz	Sampling rate
PRF	4× PRFmin	4x the minimum unambiguous PRF (PRFmin=$1.2B_D$ Hz)

Table 4.4: SAR calculated parameters for simulation

Parameter	**Value**	**Description**
V_{st}	7612.6 m/s	Platform speed
B_D	$V_{st}/\delta x$ Hz	Minimum PRF (azimuth unambiguous)
ΔR	$cT + 200\sqrt{2}$ m	Range swath length
PRF_{max}	$c/(2\Delta R)$ Hz	Maximum PRF

Now we observe the scene using the classical radar detector in a noisy environment. In the Figure 4.8 we observe that in the classical detector map of the scene both pirate ships very close, being almost inseparable.

Next, we reproduce the same scenario but instead of using the classical radar detector we use the proposed one that explores the AIS information. Obviously both pirates are uncooperative and they are not to be found in the AIS list. However, consider that the snapshot was taken before the pirates take control of the cargo vessel, meaning that the cargo AIS was active and the ship position was available at the instant of the radar snapshot. Consider also at this example that the output radar SNR (SNR after signal processing) is 14 dB.

While in the classical detector case the cargo and the pirate ship are too close to be distinguished, it may be observed in the Figure 4.9 that the proposed detector maps the scene without showing the cooperative cargo vessel, and we may cleary isolate and detect the peak corresponding to the small pirate ship near the cargo position. For detecting, we applied a detection threshold over the intensity maps. The Figures 4.10b and 4.10a represents the intensity maps (before applying a detection threshold) of respectively the classical detector and the proposed one, and the Figures 4.11b and 4.11a represents respectively both detectors after a threshold is applied.

The detection maps shows more clearly the difference between the detectors. For the given threshold we may not be able to correctly differentiate the small pirate ship from the big cargo in the conventional detector while it is clearly visible in the Figure 4.11a when the proposed detector is used.

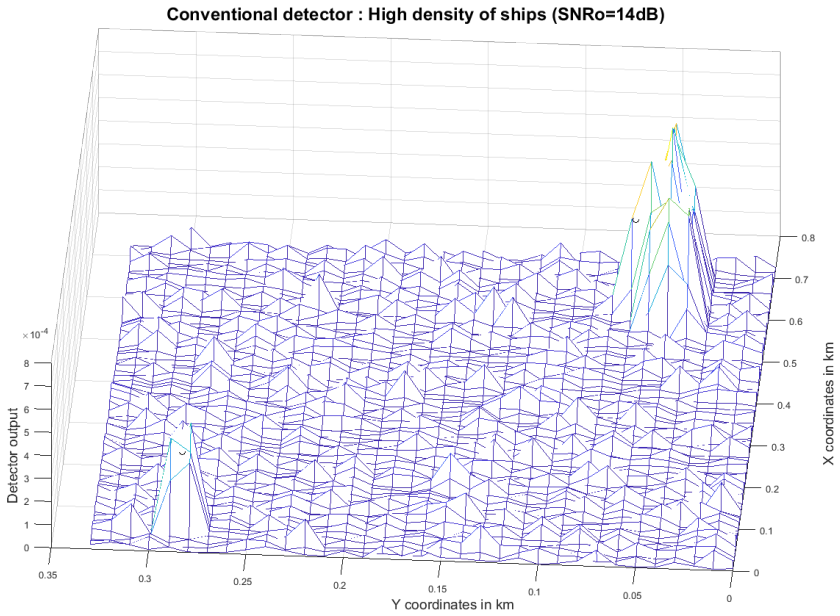

Figure 4.8: The classical detector map of the ship hijacking case. SNRout = 14dB.

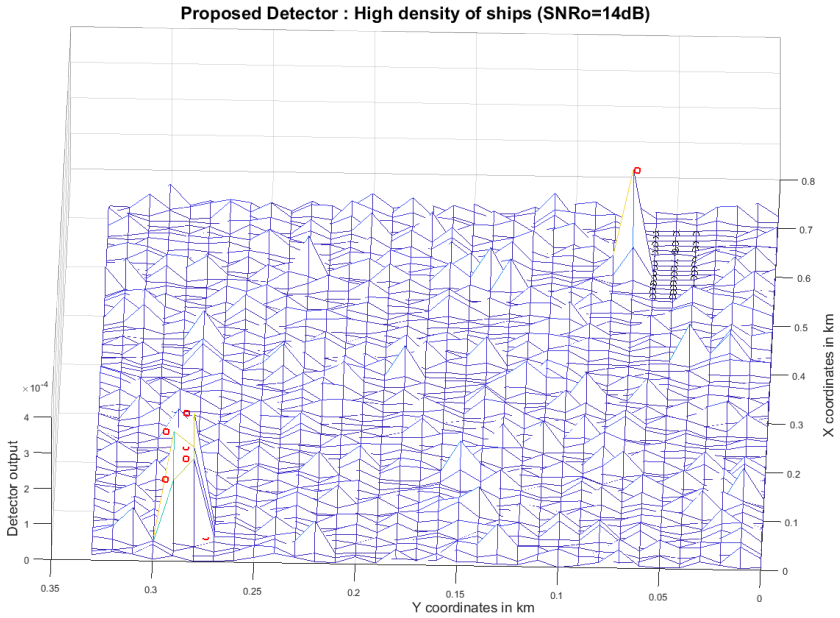

Figure 4.9: The proposed detector map of the ship hijacking case. SNRout = 14dB.

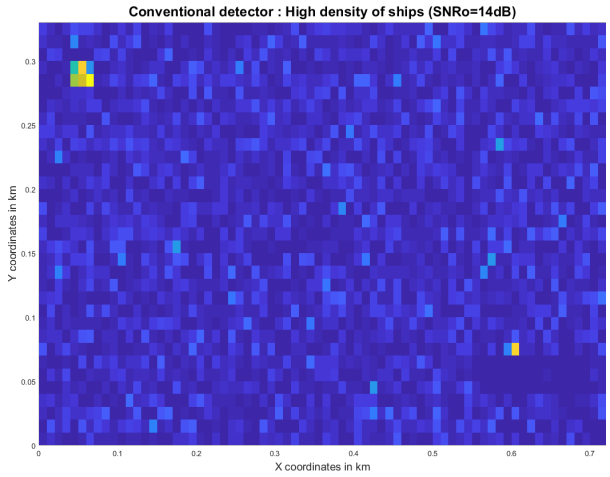

(a) The proposed detector map of the ship hijacking case. SNRout = 14dB.

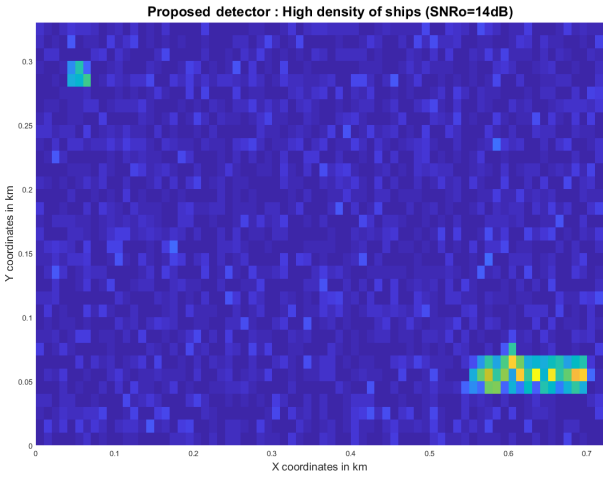

(b) The classic detector map of the ship hijacking case. SNRout = 14dB.

Figure 4.10: The classic and proposed detector map of the ship hijacking case, before applying a detection threshold.

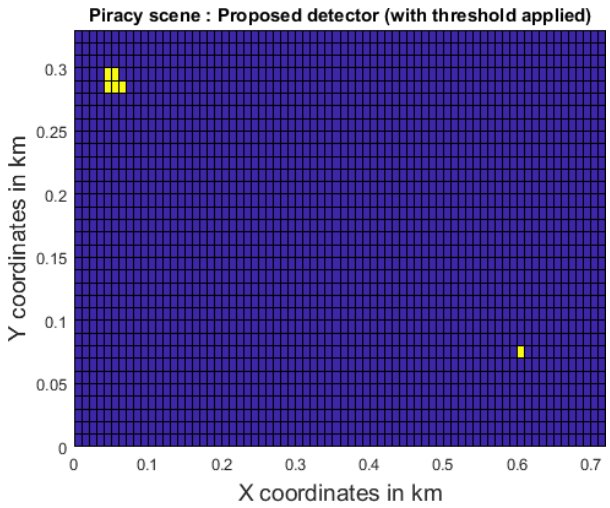

(a) The proposed detector map of the ship hijacking case. SNRout = 14dB.

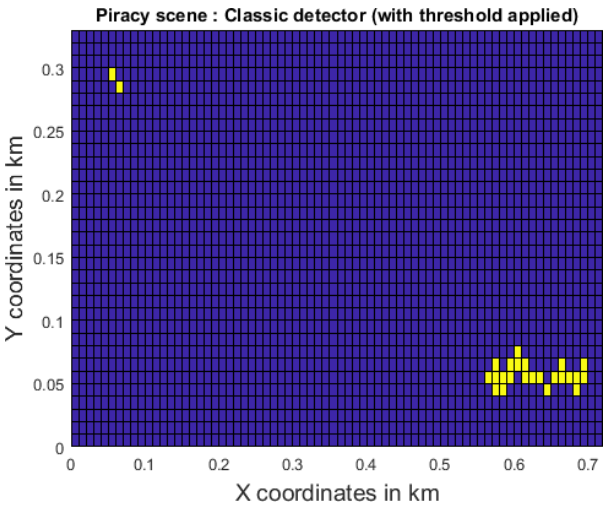

(b) The classic detector map of the ship hijacking case. SNRout = 14dB.

Figure 4.11: The classic and proposed detector map of the ship hijacking case after applying a detection threshold.

4.5 Cargo transshipment case

In this case we have a transshipment scenario involving three ships, where one ship transfers a part of its cargo to another ship by an intermediary vessel in order to illegally export goods without being noticed. Here the first ship is referred to as the export cargo (the ship that is going to provide the cargo), the second ship is the import cargo (the vessel that is interested in getting the cargo) and the third ship is an intermediary vessel, here a fishing "Trawler" that is going to transfer the cargo from the export ship to the import ship. Note that all ships are merchant and transmit their positions cooperatively using the AIS. However, they stop cooperating when engaged likely to perform illicit activities in order to avoid being detected by the policy authorities. In this context, all three ships stop transmitting their positions AIS at some point during the transshipment operation. This scenario is illustrated in the figure 4.12 where the export ship is located left and the other two ships are in the right of the figure. The red zone is the area that there are no AIS information.

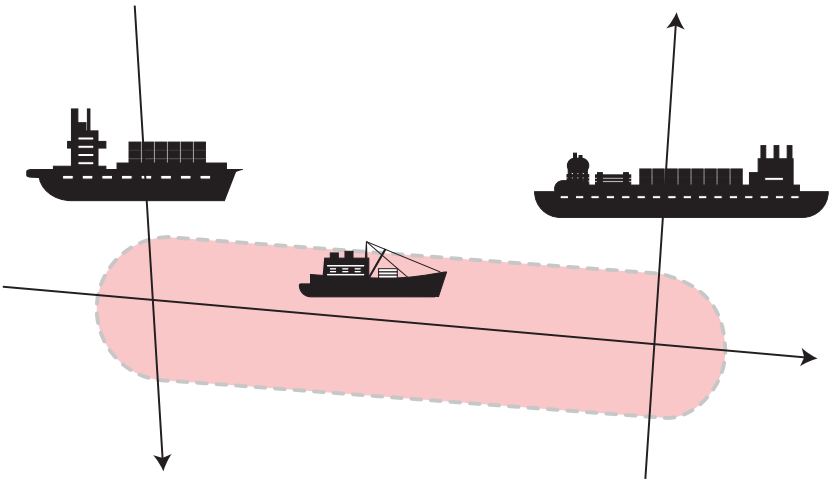

Figure 4.12: Illustration of a sea transshipment between two cargos using a third "Trawler" ship as intermediary. Red area indicates the zone where AIS is turned off.

4.5.1 Transshipment scenario simulation

Similar to the piracy case, the transshipment case is processed in a series of snapshots as it would be seen by a radar observing the scene. In this case we observe mainly the classification of targets considering both radar and AIS sources.

Consider that the transshipment operation may be gathered using 12 snapshots, and during the operations the ships turn off the AIS transmitter in order to avoid being noticed by policy authorities. In Figure 4.13 we observe the dynamic scenario with black circles indicating the real position of cooperative ships and red squares for the non-cooperative vessels. The number indicate the snapshot order from 1 to 12, the letters are the ship ID obtained from the AIS message. Here for simplicity we call the export cargo "A", "B" for the Trawler and "C" the import cargo ship. We also consider targets as punctual.

Next, we proceed by detecting using the radar classical detector and also with the proposed detector using the AIS positioning list. We consider in the simulation the SNR output of 20 dB and radar resolution of 50 m for both range and azimuth directions. The parameters of the simulation are presented in Table 4.5 and Table 4.6.

Table 4.5: SAR simulation input parameters

Parameter	**Value**	**Description**
h	500 km	Altitude
f_c	9.5 GHz	Carrier frequency
L_a	50 m	Range resolution
δx	50 m	Azimuth resolution
γ	25°	Antenna look angle
B_0T	50	Time-bandwidth product
f_s	$1.2B_0$ Hz	Sampling rate
PRF	$4 \times B_D$ Hz	Pulse repetition frequency
SNR_{out}	20 dB	Output signal-to-noise ratio

In a first step, the known positions are validated using the detector to confirm the AIS list. After

Table 4.6: SAR simulation calculated parameters

Parameter	**Value**	**Description**
V_{st}	7612.6 m/s	Platform speed
L	$\lambda R_c/L_a$ m	Synthetic aperture length
PRF_{min}	$V_{st}/\delta x$ Hz	Minimum PRF (azimuth unambiguous)

confirming the AIS positions we proceed to detect new unknown ships using the proposed detector and compare with the classical detector. In Figure 4.14 and Figure 4.15 we present the superposition of the snapshots taken from the sequence of events in the transshipment operation. The detection maps are presented after applying a detection threshold. The red squares indicate the unknown ship positions and black circles are the position of cooperative ships. The classical detector images all ships in the scene while the proposed detector only shows the new detections.

Apart from the detection gain using the proposed detector the other scenarios, here we focus in observing how the proposed detector may improve surveillance in target classification. In the scenario we infer about a suspicious activity only when comparing AIS information with a radar detection map. However, the proposed detector already fuses the AIS information with the radar data and presents directly the map with only new detections that occurred during the time window when an illegal cargo transshipment was occurring. This allows to easier evaluate the scenario and may serve as input for an improved surveillance system to identify suspicious activities.

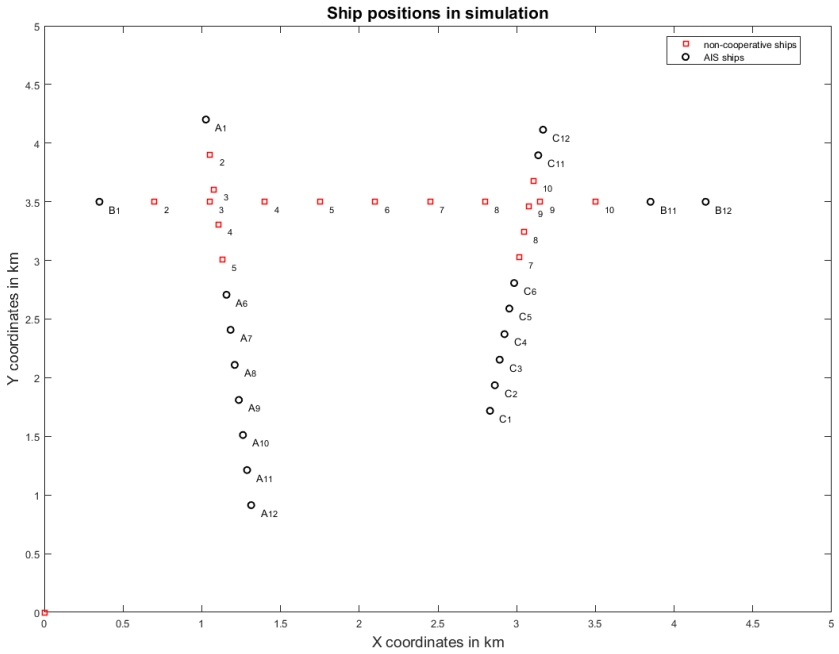

Figure 4.13: Transshipment scene : Reference map of the ships to be detected.

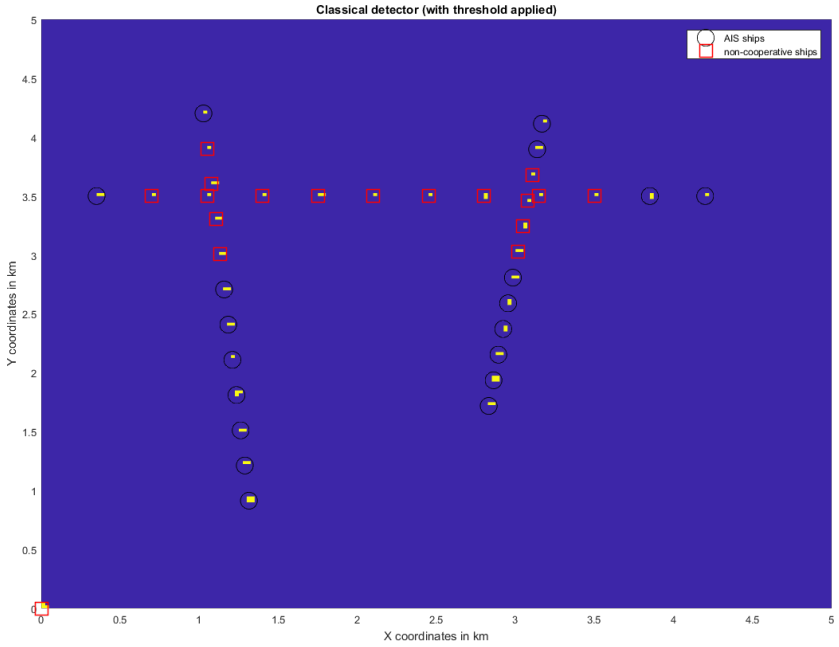

Figure 4.14: Classical detector : Detection map after applying a detection threshold.

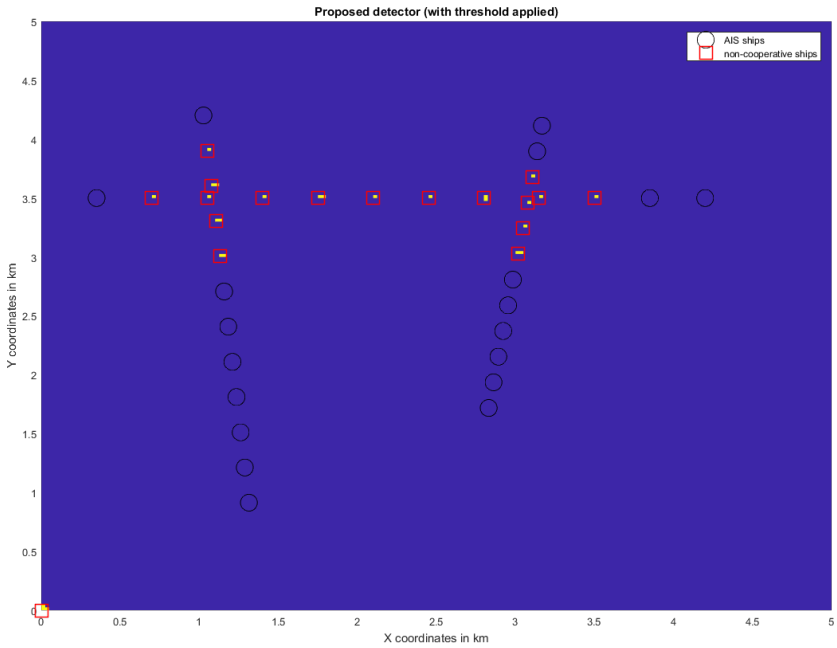

Figure 4.15: Proposed detector : Detection map after applying a detection threshold.

4.6 Scenario with important ship traffic

Here we explore the problem of detecting vessels in a dense ship density scenario. For reference, in Figure 4.16 we observe the extent of ship traffic in crowded areas like the Mediterranean, the English channel and coastal regions. The routes with dense ship traffic are indicates in the color map. Consider an example of crowded region near a port. A representation of this example scenario is illustrated in Figure 4.17.

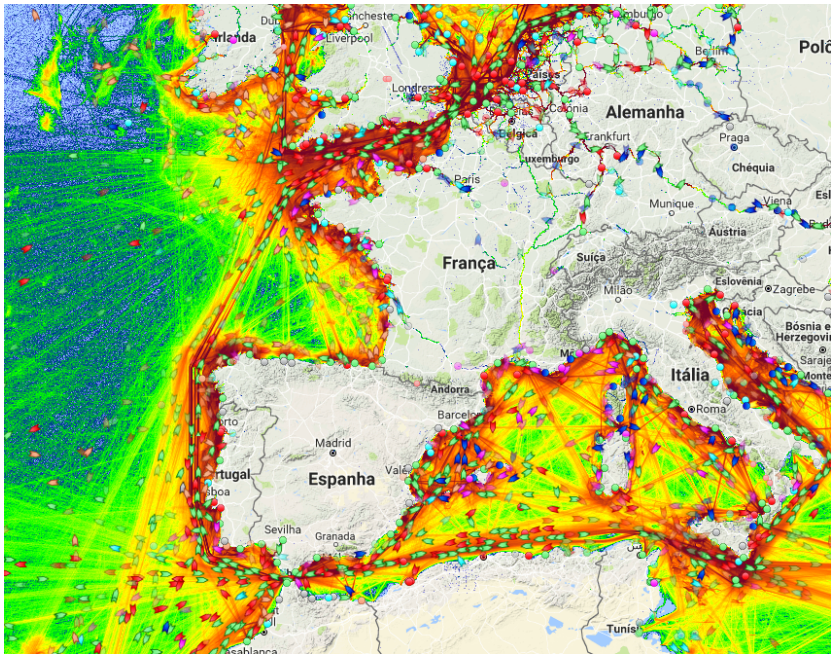

Figure 4.16: Representation of sea traffic obtained with the AIS data from www.marinetraffic.com.

4.6.1 Ship traffic scenario simulation

In this scenario we simulated a region using the classical detector to produce a radar detection map. For simplicity, we consider that all ships have the same size, and with the radar resolution, they appear as punctal targets in the radar map. For this, we modified the radar parameters in order to consider targets with radar resolution of 70×70 meters. For the simulations we consider the radar parameters indicated in the Tables 4.7 and 4.8.

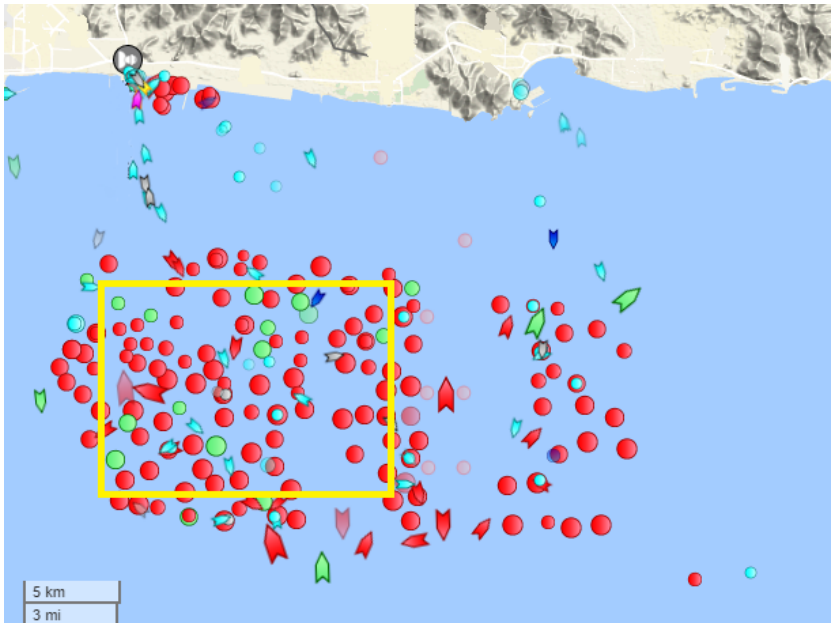

Figure 4.17: Snapshot of ship traffic from AIS data in a crowded region near a port.

Table 4.7: SAR simulation input parameters

Parameter	**Value**	**Description**
h	500 km	Altitude
f_c	9.5 GHz	Carrier frequency
L_a	20 m	Azimuth antenna length
δx	10 m	Azimuth resolution
γ	25°	Antenna look angle
B_0T	50	Time-bandwidth product
f_s	$1.2B_0$ Hz	Sampling rate
PRF	$4 \times B_D$ Hz	Pulse repetition frequency
SNR_{out}	12 dB	Output signal-to-noise ratio

For the simulation we assume a density of 200 ships including five that are not represented in the AIS list for some reason (AIS error, wrong data or because it is intentionally not cooperative). In Figure 4.18 we display the simulation scene. The black circles indicate the AIS ships while the red

Table 4.8: SAR simulation calculated parameters

Parameter	Value	Description
V_{st}	7612.6 m/s	Platform speed
L	$\lambda R_c/L_a$ m	Synthetic aperture length
PRF_{min}	$V_{st}/\delta x$ Hz	Minimum PRF (azimuth unambiguous)

squares display the ships that are not cooperative.

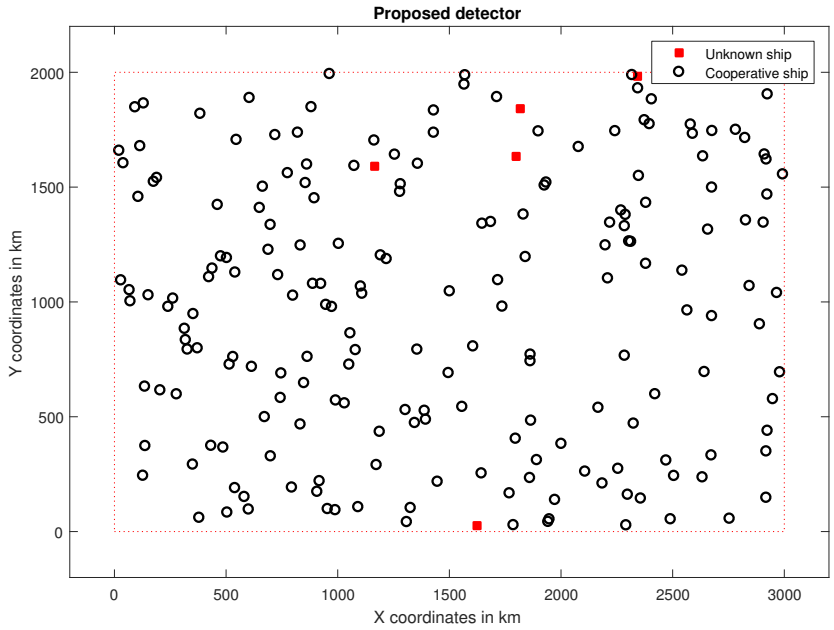

Figure 4.18: The reference map of the ships to be detected. In black circles the cooperative AIS ships and in red the unknown ones to be detected.

First, we reproduce the dense scenario using the classical radar detector. The detector images the entire scene with both cooperative and non-cooperative ships. The radar map is presented in the Figure 4.19. The peaks correspond to the more likely candidates for ships to be detected when using a given threshold to be chosen. In Figure 4.20 we observe the classical detector after applying a detection threshold. This produces a detection map of the scene with the bright spots indicating the possible positions that were classified as detections.

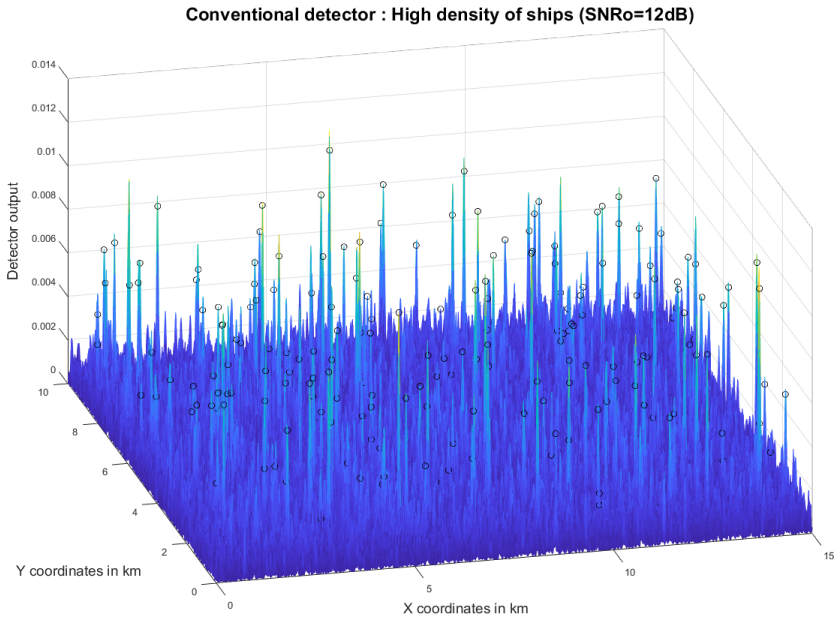

Figure 4.19: Radar map of a crowded region using the classical detector. The peaks in the map are probable target candidates. The circles indicate the real ship position, here indicated for referencing.

For comparison, we proceed by using the AIS data and the radar raw signal to process the simulation scenario. We begin by the two-step procedure discussed in 3.4, that is:

1. AIS validation

   We validate the AIS detections using the detector at the known positions in the AIS list.

2. Detection of unknown ships

   After validating the AIS, we proceed with the detection of new ships at the unknown positions using the proposed detector in order to identify non-cooperative ships in the scene.

In the Figure 4.21 we observe the raw output the proposed detector before applying a detection threshold. We denote in the figure using red squares the true positions of the non-cooperative ships in the scene. As it may be observed results show that the detection map of the proposed detector clearly indicates fewer peaks compared to the classical detector.

To show the detector in operation we also apply a detection threshold to the detection map. In the Figure 4.22 we have the positions that are classified as ships by the proposed detector.

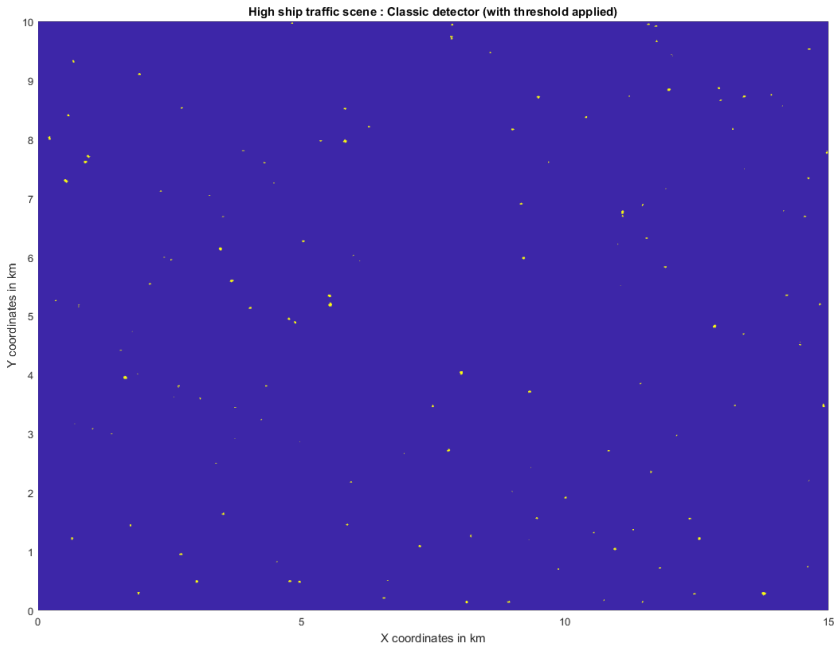

Figure 4.20: Classical detector : Detection map after applying a detection threshold.

The detection map have less interference (fewer ships) and noise from known ships when compared to the detection map of the classical radar detector.

From equation (3.9) we observe that the proposed detector explores $\acute{\boldsymbol{y}} = \boldsymbol{P}_{\boldsymbol{A}}^{\perp}\boldsymbol{y}_{\text{rad}}$, which is the orthogonal projection of the radar signatures to the orthogonal of the space containing the known AIS positions, while the classical radar detector explores the measurements $\boldsymbol{y}_{\text{rad}}$. The main difference is that the proposed detector contains fewer radar signatures, as the "whitened" measurement vector $\acute{\boldsymbol{y}}$ has only the signatures from the unknown ships, meaning less interference to the detector correlator. This gives better estimation of the radar noise power ($\boldsymbol{y}_{\text{rad}}^{H}\boldsymbol{P}_{\boldsymbol{A}}^{\perp}\boldsymbol{y}_{\text{rad}}$) when compared with the classical radar detector ($\boldsymbol{y}_{\text{rad}}^{H}\boldsymbol{y}_{\text{rad}}$) as there are fewer interference to perturb the detector noise estimation. In practice, the proposed detector identify the new detections (unknown ships) among a scene containing cooperative AIS ships. In the dense scenario despite targets being close it is not clearly observable that detecting the ships with the proposed detector improves detection. It is necessary to perform many realizations of the scene to observe the gain in probability of detection. Detection performance with proposed detector is improved when compared to the classical detector because the cooperative ships

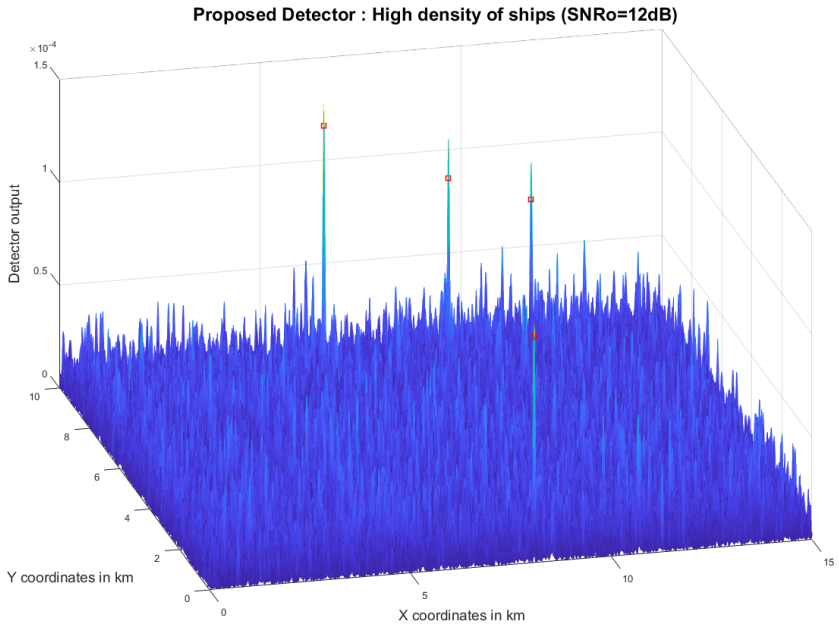

Figure 4.21: The reference map of the ships to be detected. In black circles the cooperative AIS ships and in red the unknown ones to be detected.

signatures are removed before detecting and there are less interference to perturb the detecting of new ships. This result was demonstrated in the third chapter using theoretical ROC curves and using Monte Carlo trials to obtain empirical ROC curves. Here we propose to observe a single detection map snapshot in a specific situation that the classical detection is perturbed by a ship. In the Figure 4.23 there is a small scenario showing three ships including one cooperative. The ship at coordinates (0,0) m is used for calibration of the noise level for choosing the detection threshold. Again, we plot both detector maps and apply a threshold to isolate detections in Figure 4.24. Needless to say that the AIS ship is not visible in the proposed detector map (Figure 4.24d) because it is testing only for the unknown positions. We observe that due to the interference of a nearby cooperative ship in the scene a ship detection is missing in the classical detection map. However, the proposed detector is able to detect the non-cooperative ship correctly using an equivalent threshold for the same noise realization and given an equivalent detection threshold.

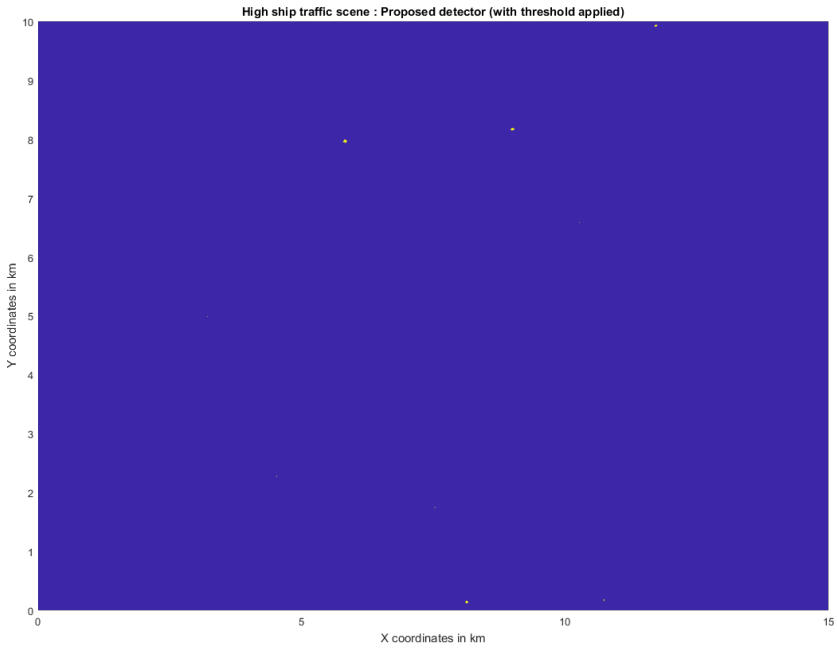

Figure 4.22: Proposed detector : Detection map after applying a detection threshold.

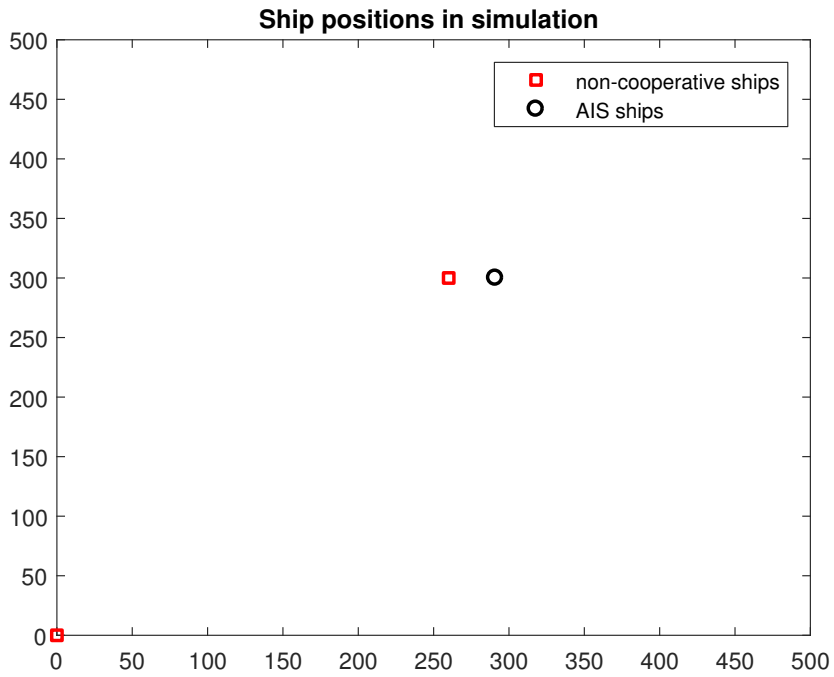

Figure 4.23: Small scene : Reference map of the ships to be detected. In black circles the cooperative AIS ships and in red squares the unknown ones to be detected.

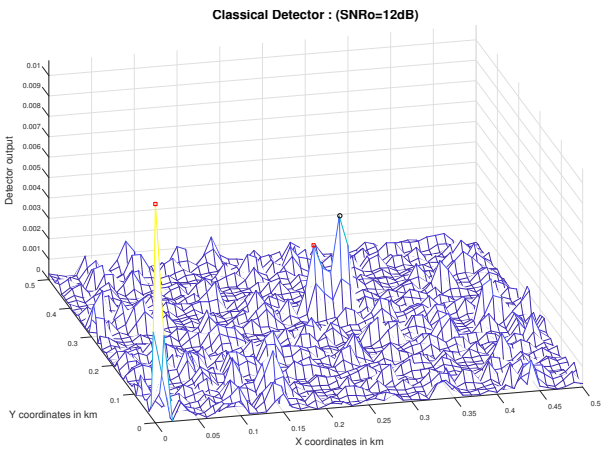

(a) Classical detector : Detection map.

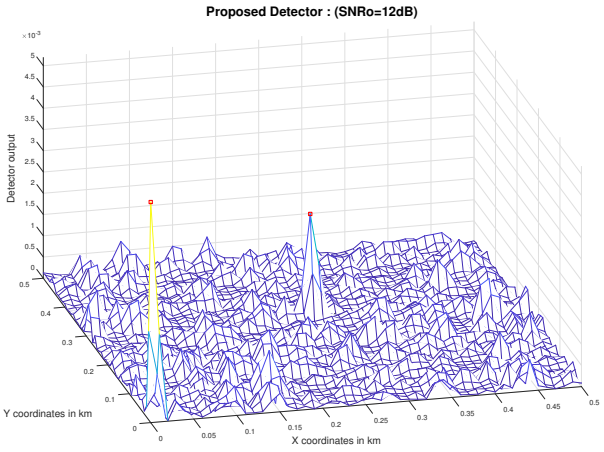

(b) Proposed detector : Detection map.

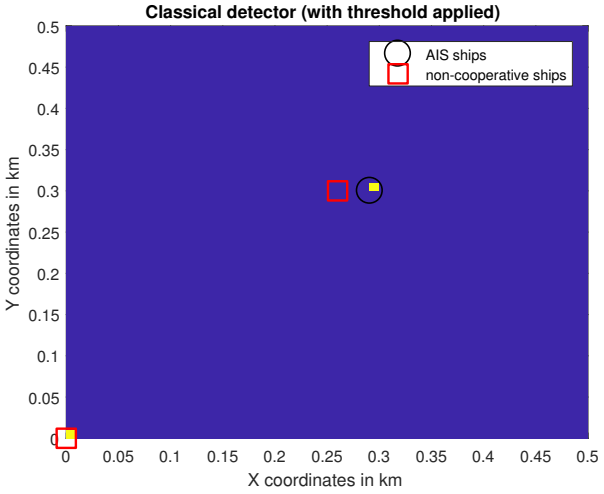

(c) Classical detector : Detection map after applying a detection threshold.

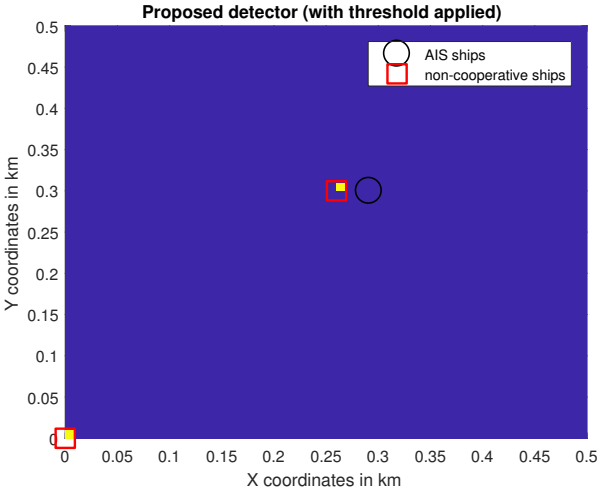

(d) Proposed detector : Detection map after applying a detection threshold.

Figure 4.24: Detection map of a small scenario containing two ships including one cooperative. For reference, the red square indicates the unknown ship positions and the black circles the position of the cooperative ship. The detection at coordinates (0,0) m is for calibration purposes.

Conclusions and perspectives

The objective of this thesis was to propose solutions in order to improve maritime surveillance using both AIS and SAR systems. In this context, the first chapter presented some possible ways of fusing AIS and radar data. From the identified methods related to data fusion, the first level of fusion seems to be promising. The joint use of raw data from both sensors, that is, data obtained just before applying any sensor's detection threshold, allows more information to be used in a ship detection process. The chapter also presented some bases about the AIS and radar systems, including details about the mathematical models used for both AIS and radar raw signals, considering them as from ships being observed from a satellite in orbit. These models were used to generate synthetic AIS and radar signals in order to evaluate and test the detection algorithms investigated in the following chapters.

The second chapter proposed a ship detection algorithm that combines the raw signals from both AIS and radar sensors for improving ship detection. It was demonstrated that fusing AIS and radar raw data allows cooperative AIS ships to be detected with a performance gain when compared to a classical radar detector, that is, a ship detector that considers only the radar data. However, the proposed detector model needed to consider important constrains due to the computational complexity resulting from the use of AIS raw data. For example, the acquisition time of the AIS signal depends on the ship dynamic conditions, whereas the radar signal corresponds to the ship position at the instant it was illuminated by the radar. Other difficulties arose from the AIS signal model, which depends on parameters different from the position, for example, related to the bit stuffing operation, the time delay, the modulation index, among others, limiting the practical use of the proposed detector in a real time application.

The third chapter studied a different approach for detecting ships using AIS and radar data in order to relax some constraints limiting the first fusion method. We proposed to use a detection list containing the positions of the AIS ships instead of the raw AIS signals. The positioning information was obtained from the AIS decoded messages after being propagated to the instant of the radar scene. The chapter also proposed a detection model that considers both the list of AIS ship positions and the radar raw signals for two different situations regarding the AIS positioning errors: First, the model assumed small positioning errors which may be neglected. Afterwards, the case of important positioning errors was considered, with positioning errors modeled using a Gaussian distribution. With respect to the AIS and radar detection errors, four hypotheses were considered. The problem can be solved using two consecutive binary hypothesis tests: In a first step, the AIS list of ship positions is validated, classifying the detections between a confirmed target (corresponding to hypothesis H_1) or a false AIS position (hypothesis H_3), that is, respectively between a ship position validated by both radar and AIS detections, or a ship position in the AIS list that does not correspond to a radar detection (due to an error in AIS data or possibly an illegal activity). In a second step, the validated AIS detections are considered in a detection model to perform another binary test for detecting new ships (hypothesis H_2), that is, confirming the presence of a ship with the radar at a position that is not in the AIS list (it might be the case for non cooperative ships). The positions that are not in the AIS list and that are not detected by the radar are associated with the last hypothesis (hypothesis H_0).

When considering the detection of new ships, the detector proposed in the third chapter outperformed the classical radar detector in the cases including cooperative ships with an important ship density or when ships are close. This improved performance is due to the interferences between the different radar signals, which affect the detection performance of the classical radar detector, while the radar signatures from cooperative ships (those belonging to the AIS positioning list) are removed by the proposed detector before detecting new ships.

The fourth chapter presented the radar signal simulator and examples of maritime surveillance scenarios being explored by the ship detectors. Some typical surveillance scenarios were chosen to illustrate how the detector proposed in the third chapter can be used to improve maritime surveillance

compared to the classical radar detector. Our results showed that the proposed detector can be used to identify specific maritime surveillance situations. For example, in cases where ships are voluntary hidden (a case of piracy) or when cooperative ships suddenly turn off their AIS transmitters (a case of illegal sea transshipment). The simulations clearly showed that ship detection can be improved with a detector that considers AIS positioning information.

This thesis showed that the combination of AIS and Radar data can improve maritime surveillance using satellites. In this context, there are different perspectives that may be considered for future work. In the second chapter regarding the detector that uses raw data from both AIS and radar, one may consider other message bits than only ship coordinates (Latitude and Longitude) in order to improve the detection performance gain. Indeed, one may consider more information bits based on previous knowledge of local ship traffic, for example, for estimating user ID, or the ship heading, or maybe other parameters from the AIS message specification.

In the third chapter, the proposed detector considered the cases of small and important positioning errors. In the case of important errors, the detector model explores the positioning errors in the AIS list and considers them as secondary data. A possible alternative would be to formalize the detection errors using a Bayesian approach, for example, by associating some prior probability for AIS detection errors (case of a false AIS) and assuming that the AIS ship coordinates are close to the expected ship position, with a positioning error described by a probability distribution (Gaussian for example). In the case of small positioning errors, a Bayesian approach could assume a probability value for the AIS detection errors, while positioning errors are negligible when smaller than the radar resolution.

Another perspective would be to explore some particularities of the maritime surveillance scenario. The maritime scene is usually very sparse, that is, the majority of tested positions do not contain a ship. It should be possible to explore this specificity of the maritime scene and try to detect ships using a sparse estimation approach. For example, considering a grid of ship coordinates, one could try to estimate the ship amplitudes assuming that, from all the possible positions in the grid, only few of them contain a ship. This approach leads to the estimation of radar signal amplitudes assuming that most of them are equal to zero (no ship), which can be formulated as a sparse estimation problem.

Another possibility to improve maritime surveillance would be to explore the information obtained

when the satellite revisits a scene. The long term ship tracking would allow more information to be available for detecting ships. Also, the tracking information would be very valuable to better estimate the occurrence of surveillance scenarios that concerns maritime surveillance applications, for example, with cases of illegal fishing, piracy, cargo transshipment, among others.

An improvement could be done in chapter 4 by dealing with extended targets. In the presented scenario containing extended targets we assumed that target form is known beforehand and the positioning information is already translated to all resolution cells relative to the ship in the detection scene, which usually is not the case. One may process the AIS heading information and the ship identification in order to obtain those information and to correctly remove the raw radar signature of the ship scatters from the scene.

Considering the radar ambiguity problem, a perspective would be to evaluate the use of the AIS information and the proposed detector to detect new targets masked by radar ambiguities from known ships with AIS.

List of publications

Conference papers

1. F. Vieira, F. Vincent, J.-Y. Tourneret, D. Bonacci, M. Spigai, M. Ansart and J. Richard "Ship detection using SAR and AIS raw data for maritime surveillance", *Proc. of 23th Conf. on Sig. Proc. (EUSIPCO'16)*, Budapest, Hungary, Aug. 29-Sep. 2, 2016.

2. F. M. Vieira, F. Vincent, J.-Y. Tourneret, D. Bonacci, M. Spigai, M. Ansart and J. Richard, "Improving synthetic aperture radar detection using the automatic identification system," *Proc. of Int. Radar Symp. (IRS'2017)*, Prague, Czech Republic, June 20-30, 2017.

Bibliography

[All15] Allianz, "Safety and shipping Review 2015", Allianz Global Corporate & Specialty, Tech. Rep., 2015.

[APP+09] D. J. Agnew, J. Pearce, G. Pramod, T. Peatman, R. Watson, J. R. Beddington, and T. J. Pitcher, "Estimating the Worldwide Extent of Illegal Fishing", *PLOS ONE*, vol. 4, no. 2, e4570, Feb. 2009.

[BLF+11] S. Brusch, S. Lehner, T. Fritz, M. Soccorsi, A. Soloviev, and B. v. Schie, "Ship Surveillance with TerraSAR-X", *2011 IEEE Trans. Geosci. Remote Sens. (IGARSS'2011)*, vol. 49, no. 3, pp. 1092–1103, Mar. 2011.

[Bur03] J. S. Burnett, *Dangerous Waters: Modern Piracy and Terror on the High Seas*, English, Reprint edition. New York, N.Y: Plume, Sep. 2003.

[CGE11] M. A. Cervera, A. Ginesi, and K. Eckstein, "Satellite-based vessel Automatic Identification System: A feasibility and performance analysis", *International Journal of Satellite Communications and Networking*, vol. 29, no. 2, pp. 117–142, Mar. 2011.

[CGM95] W. G. Carrara, R. S. Goodman, and R. M. Majewski, *Spotlight synthetic aperture radar: signal processing algorithms*, ser. The Artech House remote sensing library. Boston: Artech House, 1995.

[CM91] J. C. Curlander and R. N. McDonough, *Synthetic Aperture Radar: Systems and Signal Processing*, ser. Wiley series in remote sensing. New York: Wiley, 1991.

[CYS+11] S. K. Chaturvedi, C. S. Yang, P. Shanmuagm, J. H. Song, and K. Ouchi, "Preliminary technique to integrate SAR and AIS for ship detection and identification", in *Proc. 3rd Int. Asia-Pacific Conf. on Synthetic Aperture Radar (APSAR'2011)*, Sep. 2011, pp. 1–4.

[Det13] I. Detter, *The Law of War*, 3rd ed. Farnham Surrey, England ; Burlington, VT: Routledge, 2013.

[DFKE95] P. Diggle, S. Fienberg, K. Krickeberg, and P. S. Eriksen, *Linear and Graphical Models: for the Multivariate Complex Normal Distribution.* English. New York: Springer New York, 1995.

[EHNM06] T. Eriksen, G. Høye, B. Narheim, and B. J. Meland, "Maritime traffic monitoring using a space-based AIS receiver", en, *Acta Astronautica*, vol. 58, no. 10, pp. 537–549, May 2006.

[ESN+10] T. Eriksen, A. N. Skauen, B. Narheim, O. Helleren, O. Olsen, and R. B. Olsen, "Tracking ship traffic with Space-Based AIS: Experience gained in first months of operations", in *2010 Int. WaterSide Security Conf. (WSS'2010)*, IEEE, Nov. 2010, pp. 1–8.

[Fou12] M. Fournier, "L'apport de l'imagerie satellitale à la surveillance maritime. Contribution géographique et géopolitique", French, PhD thesis, Université de Montpellier 3, Dec. 2012.

[GAS+17] H. Greidanus, M. Alvarez, C. Santamaria, F.-X. Thoorens, N. Kourti, and P. Argentieri, "The SUMO Ship Detector Algorithm for Satellite Radar Images", *Remote Sensing*, vol. 9, no. 3, p. 246, Mar. 2017.

[GMB+09] R. Grasso, S. Mirra, A. Baldacci, J. Horstmann, M. Coffin, and M. Jarvis, "Performance Assessment of a Mathematical Morphology Ship Detection Algorithm for SAR Images through Comparison with AIS Data", in *Proc. 9th Int. Conf. Intell. Syst. Design and Applicat. (ISDA'2009)*, Nov. 2009, pp. 602–607.

[Gov11] K. Govern, "National Solutions To An International Scourge: Prosecuting Piracy Domestically As A Viable Alternative To International Tribunals", *University of Miami International and Comparative Law Review*, vol. 19, no. 1, p. 1, Oct. 2011.

[HLP15] A. Hassanin, F. Lázaro, and S. Plass, "An advanced AIS receiver using a priori information", in *IEEE Proc. OCEANS 2015 - Genova*, May 2015, pp. 1–7.

[IMO04] IMO, *The International Convention of the Safety of Life at Sea, SOLAS - Consolidated Edition.* 2004.

[IMO98] ——, *Recommendation on performance standards for an universal shipborne Automatic Identification System (AIS)*, Dec. 1998.

[ITU09] ITU-R, *M.2169 : Improved satellite detection of AIS*, Dec. 2009.

[ITU14] ——, *M.1371 : Technical characteristics for an automatic identification system using time-division multiple access in the VHF maritime mobile band*, Feb. 2014.

[LM13] J. A. Larsen and H. P. Mortensen, "In orbit validation of the AAUSAT3 SDR based AIS receiver", in *2013 6th Int. Conf. Recent Advances in Space Technologies (RAST'2013)*, IEEE, Jun. 2013, pp. 487–491.

[MA14] A. K. Maini and V. Agrawal, *Satellite technology: principles and applications*, Third edition. Chichester, West Sussex: Wiley, 2014.

[Mar11] D. Marley, *Modern piracy: a reference handbook*, ser. Contemporary world issues. Santa Barbara, USA: ABC-CLIO, 2011.

[MKS16] R. G. V. Meyer, W. Kleynhans, and C. P. Schwegmann, "Small ships don't shine: Classification of ocean vessels from low resolution, large swath area SAR acquisitions", in *IEEE Proc. Int. Geosci. and Remote Sens. Symp. (IGARSS'2016)*, Jul. 2016, pp. 975–978.

[MT11] G. Margarit and A. Tabasco, "Ship Classification in Single-Pol SAR Images Based on Fuzzy Logic", *IEEE Trans. Geosci. Remote Sens.*, vol. 49, no. 8, pp. 3129–3138, Aug. 2011.

[MVS15] F. Mazzarella, M. Vespe, and C. Santamaria, "SAR Ship Detection and Self-Reporting Data Fusion Based on Traffic Knowledge", *IEEE Geosci. Remote Sens. Lett.*, vol. 12, no. 8, pp. 1685–1689, Aug. 2015.

[Oce17] Oceans Beyond Piracy, "State Of Maritime Piracy 2016", One Earth Future Foundation, Denver, USA, Tech. Rep., 2017.

[Ong06] G. G. Ong-Web, Ed., *Piracy, maritime terrorism, and securing the Malacca Straits*, ser. IIAS/ISEAS series on maritime issues and piracy in Asia. Institute of Southeast Asian Studies, 2006.

[PCB+13] R. Prévost, M. Coulon, D. Bonacci, J. LeMaitre, J.-P. Millerioux, and J.-Y. Tourneret, "Cyclic redundancy check-based detection algorithms for automatic identification system signals received by satellite", *2013 Int. Journal of Satellite Communications and Networking*, vol. 31, no. 4, pp. 157–176, Jul. 2013.

[PPHD15] S. Plass, R. Poehlmann, R. Hermenier, and A. Dammann, "Global Maritime Surveillance by Airliner-Based AIS Detection: Preliminary Analysis", *Journal of Navigation*, vol. 68, no. 06, pp. 1195–1209, Nov. 2015.

[Pré12] R. Prévost, "Décodage et Localisation par Satellite", French, PhD thesis, INP Toulouse, Toulouse, France, Oct. 2012.

[PS08] J. G. Proakis and M. Salehi, *Digital communications*, 5th edition. Boston: McGraw-Hill, 2008.

[Rao02] C. R. Rao, *Linear Statistical Inference and its Applications*, eng, 2nd, ser. Wiley series in probability and statistics. New York: Wiley, 2002.

[RTC+10] S. Ramongassie, N. Taveneau, T. Calmettes, J. Richard, R. Challamel, O. Autran, V. Foix, and P. Durand, "RADAR and AIS sensors constellation for global maritime surveillance", in *Proc. 2010 IEEE Trans. Geosci. Remote Sens. (IGARSS'2010)*, IEEE, Jul. 2010, pp. 3793–3796.

[Sch91] L. L. Scharf, *Statistical Signal Processing*, Anglais, 1st ed. Reading, Mass: Prentice Hall, 1991.

[See03] G. Seeber, *Satellite Geodesy*, eng, 2nd edition. Berlin ; New York: Walter de Gruyter, 2003.

[Sko02] M. Skolnik, *Introduction to Radar Systems*, English, 3rd edition. Boston: McGraw-Hill, Dec. 2002.

[Sko08] ——, *Radar handbook*, 3rd edition. New York: McGraw-Hill, 2008.

[Stü00] G. L. Stüber, *Principles of Mobile Communication*, English, 2nd edition. Boston: Springer, Dec. 2000.

[UMF86] F. T. Ulaby, R. K. Moore, and A. K. Fung, *Microwave Remote Sensing: Active and Passive, Volume II: Radar Remote Sensing and Surface Scattering and Emission Theory*, English. Norwood, MA: Artech House Publishers, Mar. 1986.

[UNC08] UNCTAD, "Transport Newsletter No 38, (4th quarter 2007/ 1st quarter 2008)", UNCTAD, Newsletter 38, 2008, p. 28.

[Uni17] United Nations, *UNCTADstat database*, unctadstat.unctad.org, 2017.

[VBR08] F. Vincent, O. Besson, and C. Richard, "Matched Subspace Detection With Hypothesis Dependent Noise Power", *IEEE Trans. Signal Process.*, vol. 56, no. 11, pp. 5713–5718, Nov. 2008.

[VVT+16] F. M. Vieira, F. Vincent, J.-Y. Tourneret, D. Bonacci, M. Spigai, M. Ansart, and J. Richard, "Ship detection using SAR and AIS raw data for maritime surveillance", in *Proc. 24th European Signal Process. Conf. (EUSIPCO'2016)*, IEEE, Aug. 2016, pp. 2081–2085.

[VVT+17] ——, "Improving synthetic aperture radar detection using the automatic identification system", in *2017 18th Int. Radar Symp. (IRS'2017)*, IEEE, Jun. 2017, pp. 1–9.

[WHLN05] T. Wahl, G. K. Høye, A. Lyngvi, and B. T. Narheim, "New possible roles of small satellites in maritime surveillance", en, *Acta Astronautica*, vol. 56, no. 1-2, pp. 273–277, Jan. 2005.

[ZJX+14] Z. Zhao, K. Ji, X. Xing, H. Zou, and S. Zhou, "Ship Surveillance by Integration of Space-borne SAR and AIS – Review of Current Research", en, *Journal of Navigation*, vol. 67, no. 01, pp. 177–189, Jan. 2014.